RESONANT ULTRASONIC BONE PENETRATING NEEDLES

Rebecca Shirley Cleary

A thesis for the degree of Doctor of Philosophy (PhD)

Submitted to the College of Science and Engineering,
University of Glasgow

February 2020

Abstract

Bone biopsy is an invasive clinical procedure where a bone sample is recovered for analysis during the diagnosis of a medical condition. The procedure is performed while the patient is under either local or general anaesthesia as the patient can experience significant discomfort and possibly large haematoma due to the large axial and rotational forces applied through the needle to penetrate bone. It is well documented that power ultrasonic surgical devices offer advantages of low cutting force, high accuracy and preservation of soft tissues.

This thesis details a study of the design, analysis and evaluation of a class of novel power ultrasonic needles for bone penetration, particularly biopsy. Micrometric vibrations generated at the distal tip of a full-wavelength resonant ultrasonic device are used to penetrate the bone. Both ultrasonic longitudinal (L) and longitudinal-torsional (L-T) coupled vibration have proven successful in several applications including ultrasonic surgical devices.

Interest in ultrasonic bone cutting has grown since it was first introduced commercially as Piezosurgery® in the 1990s. More recent studies have focused on precision cutting of bone, reducing the risk of damage to surrounding delicate tissues in comparison with manual and other powered instruments.

Finite element analysis (FEA) is used to design full wavelength ultrasonic needle devices, where the geometry of the device is systematically modified to deter modal coupling by monitoring the frequency spacing between the longitudinal mode of interest and the neighbouring parasitic modes. FEA is further exploited to predict the achievable torsional displacement in a composite mode device tuned to vibrate in a longitudinal-torsional motion through degeneration of the longitudinal motion. While the L-mode device requires the operator to apply a slow backward and forward rotation and a small forward force, to maintain a forward motion and avoid imprinting, a L-T motion at the tip device could avoid this, simplifying the procedure, increasing precision and resulting in a cylindrical, less damaged

hole surface.

The dynamic behaviours predicted by FEA are validated through experimental modal analysis (EMA) demonstrating the effectiveness of FEA for the design of these devices. EMA is performed by exciting the ultrasonic needle device with a low power random excitation over a predetermined frequency range and measuring the vibration response using a 3D laser Doppler vibrometer (LDV) across a grid of points on the surface of the device.

Harmonic analysis was used to investigate the behaviour of the devices at high excitation levels to capture the inherent nonlinearity of the tuned device. The response is captured using bi-directional frequency sweeps across the tuned mode of interest at increasing excitation levels. Ultrasonic surgical instruments typically require to be driven at high excitation levels to generate sufficient vibration amplitude to cut or aspirate tissue or seal vessels. The nonlinearities of the instrument and load presented by the target tissue result in resonance frequency shift, variation in the electric impedance and instability in the vibrational response which can negatively affect the efficacy of the instrument. A resonance tracking system was developed to monitor the voltage and current and adjust the frequency in real time to compensate for the frequency shift. Additional functionality was incorporated to allow modifications to the excitation signal shape and to enable power modulation techniques to be tested in a study of their effects on the rate of progression of the device in its target tissue.

Prototype ultrasonic needle devices were evaluated in penetration tests conducted in bone mimic materials and animal bones. The devices recovered trabecular bone from the metaphysis of an ovine femur, and the biopsy samples were architecturally comparable to samples extracted using a trephine biopsy needle. The resonant needle device extracted a cortical bone sample from the central diaphysis, which is the strongest part of the bone, and the biopsy was of superior quality to the sample recovered by a trephine bone biopsy needle. The biopsy sample extracted by the resonant needle was architecturally uniform and cylindrical with an absence of chipping on the surface, suggesting that the biopsy was extracted with precision and control. To penetrate with the L mode device, the operator had to apply a slow backward and forward rotation and the small forward force, to maintain a forward motion. The rotation had to avoid imprinting of the needle tip in the bone, which otherwise resulted in the device stalling. However the L-T mode device, realised by incorporating helical cuts along the axial length, could penetrate the same animal bone sample

only requiring the small forward force, hence simplifying the procedure for the operator. The L-T device also provided increased precision, resulting in a cylindrical, less damaged hole surface.

Finally, a case study related to skull-based surgery is presented. The petrous apex is a pyramidal shaped structure at the anterior superior portion of the temporal bone and can be the location of tumours, cysts and lesions requiring diagnostic investigation. The petrous apex is challenging to access due to its medial location in the skull base and closeness to important neurovascular structures. An extended surgical approach removes the subject but is associated with morbidity and hence a minimally invasive procedure to access this site to retrieve a biopsy provides a valuable test case for the ultrasonic needle. Guided by the expertise and experience of an ear, nose and throat surgeon, the ultrasonic needle devices were modified and demonstrated in lab-based studies as a new technology for this bone penetration procedure.

Acknowledgments

First and foremost, I would like to thank my supervisor Professor Margaret Lucas. Without your help, support and patience I would not have completed this thesis. After each meeting I would have a renewed passion and motivation for the project, even during the most trying times. Throughout my extended time as a PhD student, you enabled me to attend numerous conferences across multiple continents, presenting my research and gaining an invaluable network within the world of ultrasonics. Furthermore, I would like to thank each member of the newly accredited Centre of Medical and Industrial Ultrasonics, especially Dr Andrew Mathieson whose support and insight provided during the initial years of my PhD were invaluable. I would also like to thank Professor Anthony Gachagan for introducing me to academia and ultrasonics, without the opportunities you provided I would not have pursued a PhD.

A special thanks also goes to Professor Hamish Simpson and Dr Robert Wallace from the Department of Orthopaedics and Trauma of the University of Edinburgh, and Dr Andrew Reid from the Centre of Ultrasonic Engineering of the University of Strathclyde, for their help in evaluating the ultrasonic bone biopsy needles. I would also like to thank Dr Alexander Gray and the other members of staff of the post-mortem department for their help with my many requests. Another special acknowledgement goes to the technical staff, especially Wilson MacDougall and Bernard Hoey, of the mechanical and electrical workshops for their assistance in the design and machining of the components and circuitry.

I would like to thank the British Research Council (the Engineering and Physical Sciences Research Council, grant number EP/K020013/1) for funding this research.

Finally, I would like to thank my family and friends who have shown love, support and understanding throughout this process. My parents Jim, Shirley and their partners, my in-laws Linda and Robert and my younger siblings Kimberley, Christopher and Abby, who

would all give up their time to watch our little monster while I wrote. Each of you provided encouragement whilst expecting nothing in return. Chris and Jess, through many hours of writing during evenings and weekends, you have shown me patience and devotion while providing me with a copious amount of coffee. We took on this challenge as a family and I look forward to what we do next. You are all part of this thesis and I simply would not have achieved this without you.

List of Symbols

α_R	Rayleigh mass proportional damping
β_R	Rayleigh stiffness proportional damping
Δi	Current error
Δcon	Joining plane of the conical-cylindrical section
$\Delta\theta$	Phase error
e_o	Absolute dielectric constant
λ	Wavelength
μ_{rp}	Relative permeability of core
ω_R	Natural resonant frequency of a system
ρ	Density
θ	Twist angle
B	Bending mode
Bo	Bolt mode
C	Capacitor
c	Damping
C_1	Capacitor, mechanical loss
C_{ij}^E	Elastic modulus at constant electric field
c_L	Wave velocity of longitudinal vibration

C_o	Capacitance of the clamped transducer
d	Strain
D_{cut}	Cut depth
D_{ijkl}	Elastic properties of piezoceramic
d_{ij}	Piezoelectric charge constant, relating the strain to the applied electrical field
E	Young's modulus
e	Stress
e_{ij}	Piezoelectric charge constant, relating the stress to the applied electrical field
e_{ij}^S	Permittivity of piezoceramic material at constant strain
e_{ij}^T	Permittivity of piezoceramic material at constant stress
f	Frequency
f_B	Frequency of bending modes
f_L	Frequency of longitudinal modes
F_{pl}	Preload force
f_p	Parallel resonance frequency
f_r	Anti-resonant frequency
f_r	Resonant frequency
f_s	Series resonance frequency
f_T	Frequency of torsional modes
FEA	Finite element analysis
FFT	Fast Fourier transform

FRF	Frequency response function
g_{ij}	Piezoelectric charge constant, relating the electrical field to the applied stress
ID	Inner diameter
K	Radius of gyration
k	Spring
k_{eff}	Effective electromechanical coupling coefficient
L	Longitudinal
L-T	Longitudinal-torsional
L_1	Inductor, mass component
L_{cut}	Cut length
L_{cyl}	Length of the cylinder section
L_{need}	Needle length
L_r	Rod length
LDV	Laser Doppler vibrometer
m	Mass
N	Number of turns
n	Mode number
n_i	Position of the i^{th} nodal plane
N_o	Number of piezoceramic rings
N_P	Number turns on primary winding
N_S	Number turns on secondary winding
OD	Outer diameter

p	Pitch
PCF	Pound per cubic foot
PZT	Lead zirconate titanate
Q_M	Mechanical quality factor
r	Radius of the toroid
R_1	Resistance, mechanical compliance
R_o	Resistance, dielectric loss
$step$	Location of the step
T	Torsional
$USN1$	Ultrasonic needle 1
$USN2$	Ultrasonic needle 2
$USN3$	Ultrasonic needle 3
$USNLT$	Ultrasonic needle longitudinal torsional
V	Voltage
v	Poisson's ratio
V_P	Primary winding voltage
V_S	Secondary winding voltage
Z_b	Acoustic impedances of the back mass
Z_e	Electrical impedance
Z_f	Acoustic impedances of the front mass
Z_L	Internal impedance of load
Z_o	Characteristic acoustic impedance
Z_p	Acoustic impedances of the piezoceramic
Z_S	Internal impedance of source

Contents

List of Tables

List of Figures

Chapter 1

Introduction

Ultrasonic bone cutting instruments are established for enhanced precision, safety and efficacy in several surgical applications. The devices are powered by piezoelectric transducers vibrating at ultrasonic frequencies between 20 and 60 kHz. They are most commonly used in oral and maxillofacial surgery where the advantages include selective cutting and precision. Periodontal and endodontic surgery particularly benefit from the precision of these devices due to the delicate bone structures involved, while invasive bone surgeries such as maxillectomy and mandibulectomy profit from the preservation of surrounding neurovascular structures. The potential of novel bone penetrating needles is significant, permitting direct surgical intervention, including biopsies, at targets within or obscured by bone. The progression towards minimal access surgery and the search for improved treatments for medical conditions is considerable. The importance of this research is significant; the potential outcomes could be transformative in the field of ultrasonic surgical devices.

This research was part of an EPSRC funded project; "Ultrasonic needles based on Mn-doped ternary piezocrystals". This project was led by the University of Glasgow, driven by the possibility of improving how bone biopsies are conducted while also investigating other applications which would benefit from a bone penetrating needle. Partners at the University of Dundee focussed on developing characterisation techniques capable of obtaining the property matrix of the piezocrystals over a range of nominal temperatures and pressures, while the University of Edinburgh collaborators assessed the effectiveness of the devices in soft-embalmed and fresh-frozen human cadavers and through animal studies.

The body of work described in this document focuses on the device design, characterisation

and testing. The research is centred around modelling and developing innovative features and ultrasonic excitation approaches that meet the challenges of penetrating bone with an ultrasonic needle.

1.1 Bone biopsy

A bone biopsy is an invasive diagnostic procedure where a small tissue sample is extracted from within the human body. The sample is examined through microscopy to diagnose a bone disorder or investigate an abnormality such as a bone tumour. There are traditionally two types of bone biopsy, open or closed. To perform an open biopsy the clinician will make a cut in the skin on top of the bone and remove a sample. For a closed or needle biopsy the clinician makes a small incision in the skin then uses a needle to take out the sample.

The needle further categorises bone biopsies as either a fine needle aspiration (FNA) or core biopsy. FNA involves collecting a sample from a cyst or solid mass using a fine needle and syringe. However only a small sample of cells or tissue can be obtained. A core needle biopsy is more invasive using a hollow needle to retrieve tissue rather than cells. While FNA rarely requires anaesthetic, a core biopsy generally involves either local or general anaesthetic to numb the area. However, collecting tissue samples delivers more information about the tumour or lesion, increasing the chances of establishing a final diagnosis.

When investigating a metabolic disease, a biopsy sample is commonly collected from the iliac crest of the pelvis as shown in Figure 1.1. The iliac crest possesses a thin outer wall and minimal surrounding soft tissue which eases the clinical process and reduces patient discomfort. This is adequate when investigating a pathology which affects the whole body, such as leukaemia or osteoporosis. However, it is not uncommon to perform a biopsy of other areas of the body, typically at the location where a tumour or lesion exists.

1.1.1 Bone anatomy

To understand the process of retrieving a bone biopsy it is important to recognise the complexity of bone tissue. The shape of bone is generalised into four distinct types: long, short, flat and irregular. Each shape comprises of different compositions of two distinct bone tissue types; cortical and trabecular. The distribution and concentration of each type varies based on the bone's function within the body.

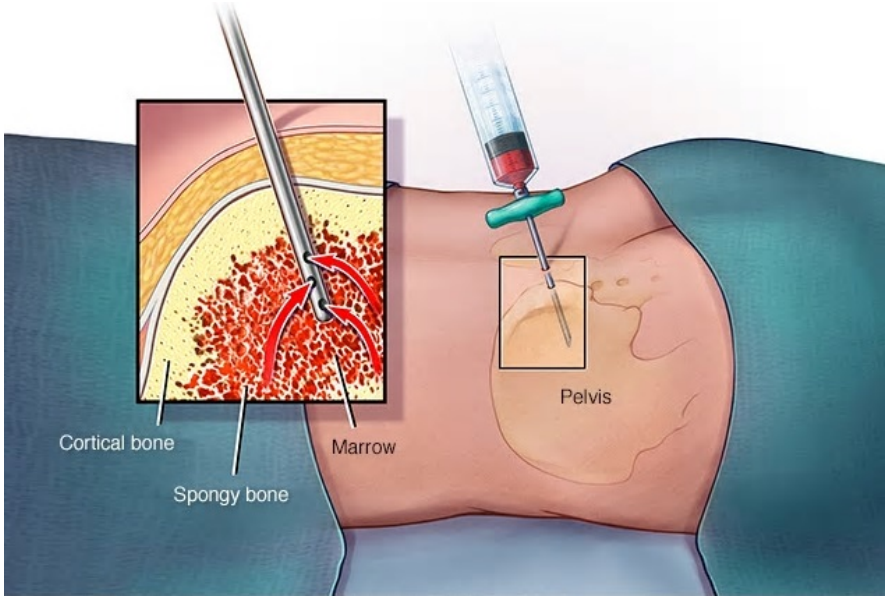

Figure 1.1: Bone Marrow Biopsy [1]

Cortical or compact bone is the thin outer layer which provides strength. It is dense as to withstand compressive forces while also providing support and protection. The spongy, cancellous trabecular bone is lightweight, structurally resembling honeycomb. The spaces within the network provides flexibility and supports shifts in the weight distribution. Trabecular bone is commonly found providing support at the ends of weight-bearing bone.

Bone marrow a soft, gelatinous tissue lies within the hollow interior of larger bone as shown in Figure 1.1. Bone marrow is where circulating blood cells are produced hence retrieving a sample can aid the diagnosis of anaemia, bone marrow diseases, blood cell conditions and cancers of the bone marrow or blood. The design of the ultrasonic needle is defined by the requirements of obtaining a bone marrow sample. The device must be capable of penetrating cortical and trabecular bone tissue, allowing access to the bone marrow within.

1.1.2 The current state of core bone biopsies

Bone marrow biopsy as a diagnostic technique was first introduced in the beginning of the nineteenth century. Over the years the procedure has evolved into a simple, repeatable process standardised in the 1970s [2]. The most common needle is a trephine bone marrow biopsy system.

A trephine bone biopsy system such as the one in Figure 1.2, consists of the stylet, probe and needle. The needle with the stylet in place is used when advancing through the soft tissue

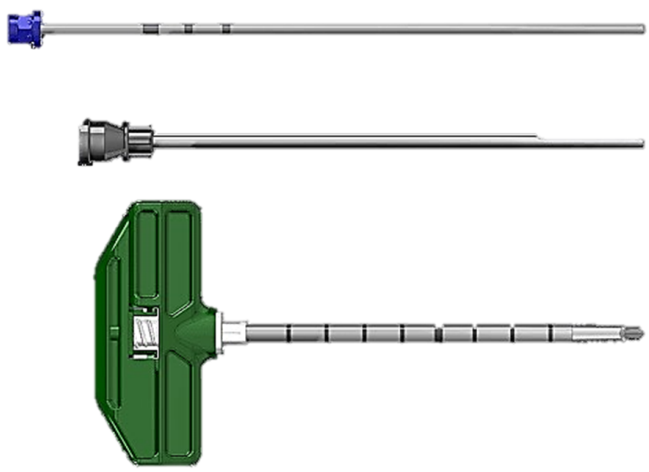

Figure 1.2: Trephine bone biopsy system [3]

using firm pressure. At the cortex or cortical bone, the needle is placed at a 90° angle while applying downward pressure and a twisting motion. Decreased resistance felt by the clinician is used to identify that the marrow cavity has been reached, the stylet is then removed. Two techniques are commonly used to obtain a sample depending on whether you wish to aspirate or obtain a core. By slowly advancing the needle further into the subject with a twisting action, a core can be obtained. To aspirate a sample, a syringe is connected to the cannula and quickly withdrawn, applying a negative pressure to obtain a sample.

Limited research has been undertaken to control the pain felt by the patient caused by the procedure [4]. The intensity and duration of pain has been addressed in a few clinical studies [5], [6]. Most patients report moderate to severe pain which can last for three to four days after the procedure is performed. Both studies conclude a strong correlation between the expertise of the clinician and the pain experienced by the patient.

Although rare, haematomas caused by bone marrow aspiration and trephine biopsies have been reported [7], [8]. A haematoma is blood pooling beneath the surface, outside the blood vessels caused by either trauma or disease. A retroperitoneal haemorrhage is the most commonly reported type associated with bone marrow trephine biopsies. Cases have been reported for patients across a range of sexes and ages [7], [9]. This complication results from the large forces required to penetrate the cortical bone. There is a clear opportunity to improve the efficacy and safety of bone biopsies. This work will focus on applying the advantages offered by high power ultrasonics.

1.2 Ultrasonic surgical devices

Sound waves above the audible range of human hearing are described as ultrasonic. Ultrasound has a wide range of applications which can be divided according to frequency and power level. Low power applications are defined by the ultrasound not permanently altering the target. These are typically measurement based and include medical imaging and non-destructive testing. Low power is paired with a high frequency, typically over 1 MHz, as the shorter wavelength offers a higher image resolution. High power ultrasound has a permanent or lasting effect on the target. Commonly called power ultrasonics, the frequencies tend to be low, between 20 kHz and 100 kHz. Power ultrasonics are used for a wide and diverse range of industrial and medical applications including surgery.

Power ultrasonic systems consist of a generator, supplying the electrical signal, a transducer converting the electrical excitation signal to mechanical vibration and an end-effector or tool. The most common electromechanical transducer is piezoelectric. Polarised molecules within the materials periodically align with the oscillating electrical field, this molecular realignment causing a change in material dimensions. Piezoelectric are the most common transducer as piezoceramic is available in many shapes, sizes and crystal orientations. This versatility allows piezoelectric transducers to be adapted to suit the need of many applications. Most power ultrasonic transducers are configured as a Langevin, or sandwich transducer, where the piezoelectric ceramics are held between two metal end masses. Since being introduced, this configuration has been adapted to a wide range of surgical and clinical applications described in the sections to follow.

1.2.1 High intensity focused ultrasound

High intensity focused ultrasound (HIFU) is a non-invasive surgical technique which utilises a focused ultrasound beam to destroy tissue via a process called coagulative necrosis. The ultrasound beam passes harmlessly through intervening tissues towards the target, however at the focal point the energy levels cause immediate cell death. A common feature of HIFU transducers is an axisymmetric bowl aperture which spherically focuses the ultrasound energy as in Figure 1.3. The intensity of the focused ultrasound can reach between 100 -10,000 W/cm^2 at the target area.

There are two main processes in HIFU, thermal heating and acoustic cavitation.

The focused ultrasound induces vibration in the tissue which causes frictional heat and subsequently when the temperature reaches higher than 56°C for over two seconds cell death occurs. Acoustical cavitation occurs when the tissue is subject to cyclic pressure. Hollow cavities, when subjected to alternating high and low levels of pressure, implode generating an intense shock wave. In tissue this disrupts the cell membrane and destroys surrounding tissue structure. Cavitation damage is more difficult to control and predict than thermally induced cell death.

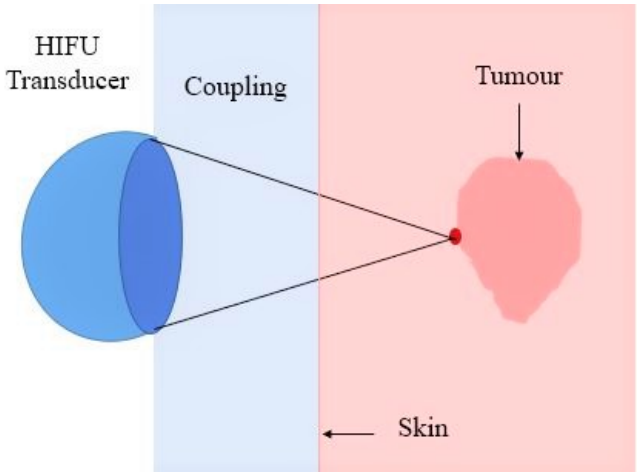

Figure 1.3: High intensity focused ultrasound

HIFU treatment is generally guided by diagnostic ultrasound or MRI imaging. The technique has gained validation as a minimally invasive treatment of a range of cancers including that of the liver, prostate, bladder and breast [10]. Perhaps the most prevalent clinical treatment is a trans-rectal device to treat prostate cancer [11], [12].

1.2.2 Phacoemulsification

Phacoemulsification (phaco) is a type of cataract surgery which uses an ultrasonic handpiece to fragment the cloudy cataract lens into tiny pieces simultaneously suctioned out. The lens is then replaced with an intraocular lens implant(IOL) as shown in Figure 1.4. Three components constitute a phaco system; irrigation, aspiration and ultrasonics. Irrigation maintains the intraocular pressure and provides a fluid flow to aid the removal of the particles from the eye, while also cooling the handpiece. Aspiration provides the outward flow of the particles through a controlled suction.

The phaco handpiece vibrates ultrasonically inducing a longitudinal or composite

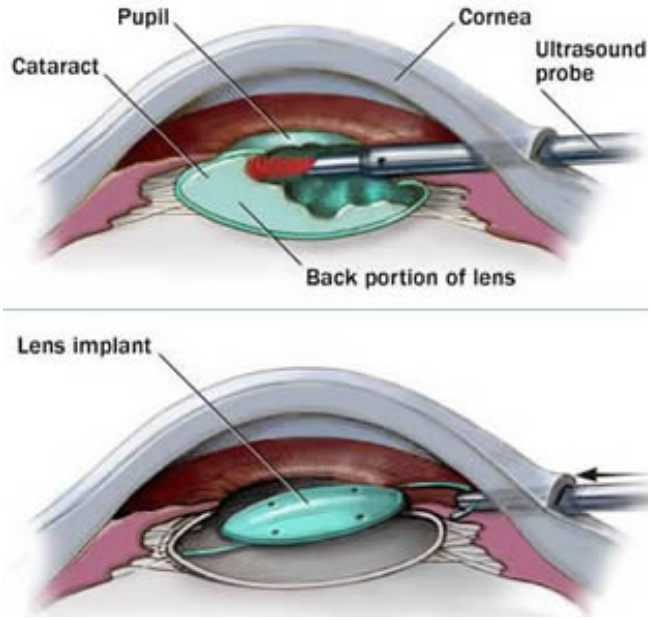

Figure 1.4: Phacoemulsification cataract surgery [13]

longitudinal-transverse motion at the tip. The stroke length of phaco technologies varies from 40 μm to 100 μm while the frequency of operation is normally between 27 and 60 kHz. Differing the stroke length and operating frequency can prove advantageous when tackling tissues of various densities. In phaco the damage mechanism combines mechanical energy and cavitation. Mechanically the cataract is chiselled away by the vibrating tip of the device. Multiple angles and configurations of tips are available such as bevelled, round, ellipsoid, bent or flared, designed to enhance the tip-tissue interaction. Cavitation occurs when micro bubbles are formed as the tip retracts from its original position which causes high negative pressure. The forward tip motion then compresses the bubbles. Bubbles oscillate and can implode causing a powerful shock wave.

Charles D. Kelman was the pioneer of phacoemulsification first introducing the technique in 1967 [14]. Despite benefits being apparent at the early stages of development, the adoption of phaco over extracapsular cataract extraction(ECCE) was slow. Not until 1995 did phaco replace ECCE and became the gold standard procedure for cataract removal in high income countries [15], [16].

1.2.3 Ultrasonic surgical aspirator

The Cavitron ultrasonic surgical aspirator (CUSA) is the original ultrasonically powered device for surgery introduced in 1977 [17]. The CUSA delivers ultrasonic waves at around

25 kHz removing target tissue through cavitation. The magnetostrictive transducer, shown in Figure 1.5, produces a vibrational amplitude of approximately 300 μm using a coil placed around a stack of nickel alloy plates.

The transducer transmits the vibration through a connecting body to a surgical tip, both providing amplification. The hollow 3 mm tip enables aspiration of the fragmented tissue and irrigation to be applied. The irrigation fluid flows around the outside of the vibrating tip to avoid heat accumulation. Different tips and handpieces were developed, further enhancing the capabilities of the system. A 24 kHz system could fragment tough, calcified tumours which require higher power and faster removal, while a 35 kHz system powered at low excitation provided enhanced precision and control. Not only has the original CUSA since been improved but this device has inspired a wide range of similar technologies.

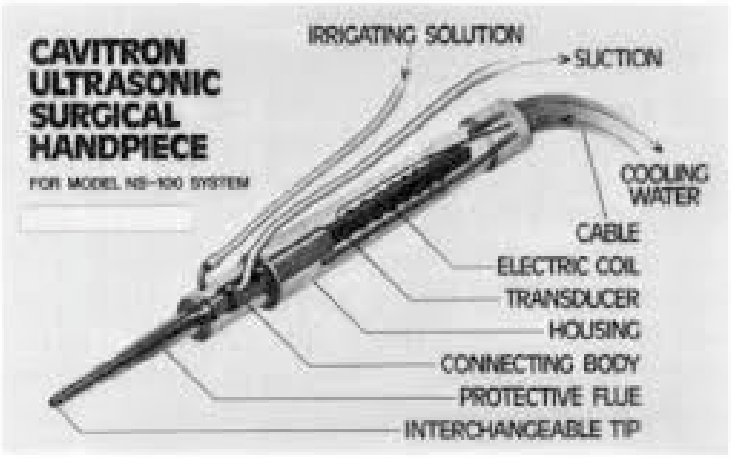

Figure 1.5: Cavitron ultrasonic surgical aspirator [18]

1.2.4 Soft tissue dissection

Following the widespread acceptance of CUSA, high power ultrasonics was considered for tissue cutting and coagulation. Unlike the latter technologies where propagation of the vibratory energy into the tissue was an important mechanism, the cutting or dissection of tissue occurs due to the tip-tissue interaction. The vibrational amplitude at the tip of these device can reach a few hundred microns across a frequency range of 20 to 60 kHz.

Ultrasonic devices have proven to be a superior alternative for soft tissue dissection over laser and electrosurgery which pose an inherent danger to both the patient and clinician. These predecessors generated heat commonly resulting in smoke which can limit the surgeon's

vision. Ultrasonics boasts advantages in precision and safety [19], combining cutting and cauterisation of tissue, which reduces bleeding and offering tissue selectivity, fragmenting one tissue type while sparing another [20].

There has been a multitude of devices developed since the CUSA was first proposed in the late 1970s, operating across a range of frequencies, developed with interchangeable tips to fit the needs of different surgical applications. This includes the Harmonic® Scalpel from Ethicon in Figure 1.6. The active blade or probe vibrates longitudinally at a frequency of around 55 kHz, acts as the bottom section of a jaw. The top arm which does not vibrate clamps the tissue for dissection. Advantages of the harmonic scalpel for soft tissue dissection include precision [21], steady haemostasis [22] and less lateral thermal spread [23].

Figure 1.6: The Harmonic® scalpel [24]

1.2.5 Hard tissue dissection

Cutting hard, dense tissue requires significant energy and motion traditionally achieved using manual instruments or oscillating bone saws or burs. Manual instruments require high forces to perform the cut, while rotary and oscillating saws require less force, but friction causes significant heat build-up. This can induce thermal injury in surrounding tissues leading to osteonecrosis and tissue necrosis [25]. Realising an ultrasonic bone cutting instrument for hard tissues such as bone or calculi involves exploiting a repetitive impact mechanic like that used in phacoemulsification.

Dentistry

Using ultrasonic instruments in dentistry to dissect hard tissue has been widely accepted for over 60 years. Scalers operating at frequencies between 25 and 40 kHz are used to remove deposits from the tooth. The longitudinal vibration at the tip of the device creates a 'chipping' action to eradicate dental plaque from the surface of the tooth. The devices reduce hand fatigue of the operator, remove the need for an ultra-sharp-edged scaler and decrease the scraping sensation felt by the patient [26]. Many variations of this device have appeared including the Cavitron system Touch^{TM} scaler in Figure 1.7.

Figure 1.7: The Cavitron Touch^{TM} ultrasonic scaler [27]

Bone surgery

Despite the success of ultrasonic devices in dentistry it was not until early in the 21st century that ultrasonic bone surgery was extended to other fields. For the past two decades it has become a popular technique as it suppresses the risk of damaging surrounding critical structures [28]. Piezosurgery® coined by Mectron S.p.A was used to describe the first commercially available ultrasonic device for osteotomy in Figure 1.8. Osteotomy in maxillofacial surgery requires control and precision to avoid damaging surrounding nerves and tissues. The device promotes selective cutting as the vibrations at the tip cuts bone tissue while sparing surrounding soft tissues. Comparable to the Harmonic scalpel it also reduces haemorrhaging [29], improves visibility and precision [30]. A longitudinal transducer is paired with a variety of cutting inserts depending on the procedure. The cutting inserts induce a longitudinal or composite longitudinal-flexural motion.

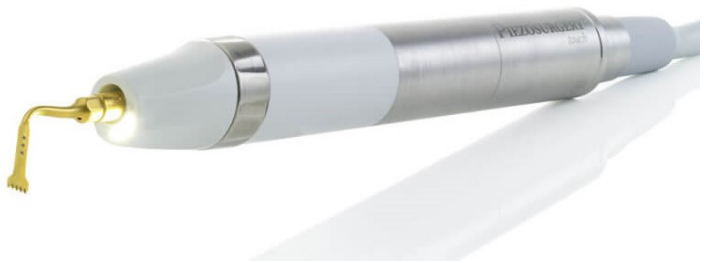

Figure 1.8: Piezosurgery® device [31]

Initially developed for maxillofacial surgery, a multitude of ultrasonic devices have since been developed by various companies for cutting a variety of bone tissues. Ultrasonic bone surgery is now used for several applications including neurosurgery [32], [33], orthopaedics [34], [35] and ear nose and throat surgery [36], [37].

1.2.6 Bone drilling

Bone drilling is extensively used in orthopaedic surgery where a hole is required for fixation. When performing this operation considerable frictional heat can cause extensive damage in the form of thermal necrosis [38]. The requirement for an improved technique has led a study of ultrasonically assisted drilling. Lab studies showed that US assisted drilling could reduce the force and torque required to penetrate cortical bone [39]. Axial ultrasonic vibration is superimposed onto the motion of a standard drill bit to reduce drilling-induced damage. Ultrasonically assisted drilling produced a superior surface finish over conventional methods.

1.3 Outline of work

There are several risks associated with performing a bone biopsy, this work endeavours to address these by realising a device which can perform the penetration with less force and precision higher than current techniques. The utilization of power ultrasonics across multiple surgical applications has increased substantially. This study aims to exploit the benefits of ultrasonic surgery which include selective cutting, low forces and improved precision by developing novel bone biopsy needles.

A class of ultrasonic needles are realised which will penetrate bone with a resonant needle. The tip directly impacts the bone, oscillating at a frequency of around 25 kHz. Finite

element analysis (FEA) is used to predict the resonant frequencies and modes of vibration of the devices before manufacture. By extracting the eigenmodes, while systematically altering the needle geometry, prototype designs are obtained. A longitudinal vibration is hence isolated from close neighbouring flexural modes and torsional modes which could be easily excited. Then, a composite, longitudinal-torsional mode, device is investigated with helical cuts introduced along the length of the needle to degenerate longitudinal vibration into combined longitudinal-torsional vibration. The aim is to avoid imprinting of the needle in bone and to improve debris removal.

Validation of the devices designed using finite element modelling was carried out by constructing prototype devices which are then characterised for their vibrational responses. Experimental modal analysis was conducted using a 3D laser Doppler vibrometer to measure the vibrational response of the devices and validate the FEA results. Next the driving signal of the ultrasonic needles is investigated by developing an impedance tracking system. A resonance tracking system, originally developed by the University of Dundee partners, allowed different signals to be proposed to improve speed and precision and reduce the temperature at the biopsy site.

Throughout the research penetration tests have been conducted in bone tissue mimic and in animal samples. Performance of each needle was evaluated based on the damage around the biopsy site through microscopy. Finally the first clinical tests were performed by an orthopaedic surgeon directly comparing the ultrasonic needles with a trephine bone biopsy needle.

Chapter 2

Literature Review

2.1 Bone biopsy

A biopsy is performed to investigate abnormalities within the human body by obtaining a sample of tissue. The anomaly under examination can be functional, such as liver disease or structural, such as swelling. The first diagnostic biopsy was performed in Russia in 1875 by Rudnev [40]. The word "biopsy" was then coined in 1879 by Ernest Besnier, a French dermatologist [41]. Despite these early procedures a lack of histologic procedure for living organs and tissue meant that the application was rare until the 20th century.

A bone marrow biopsy was first attempted by Pianese in 1903, who punctured the epiphysis of a femur utilizing a surgical trephine for diagnostic purposes [42]. In 1922, Morris and Falconer introduced a drill technique to obtain marrow from the tibia while Russian physician Anirkin utilised a lumbar puncture needle to obtain bone marrow from the sternum [43]. During the decades to follow, research focused on the design of the needle to improve its ability to efficiently retrieve a biopsy. In 1931 Arjeff introduced a guard onto the needle, an element then found on the common Klima needle realised in 1935, shown in Figure 2.1 (a) [43]. In 1934, Henning and Korth suggested a cannula to allow irrigation [44].

Until now, these procedures were completed without local anaesthetic which caused complications and morbidity during the 1940s. Improvements were continually sought, such as in 1954 when the Sacker-Nordin trephine was realised which could safely obtain samples from the iliac crest [46]. High rate of inadequate samples was addressed by McFarland and Dameshek using the Vim-Silverman biopsy needle [47]. In 1969, the Jamshidi needle was

Figure 2.1: (a) Klima needle (b) Jamshidi needle [45]

realised and patented [48], pictured in Figure 2.1 (b). The Jamshidi needle and similar technologies, described in Section 1.1.2, have led the bone marrow biopsy field for over 40 years. They have proven to provide specimens superior in size and architecture [49].

Since the inception of bone biopsies, a less painful method has been sought which can reliably obtain high quality biopsies. In 1987, Burkhardt performed a marrow biopsy with an electric drill and filed a patent two decades later for a power biopsy needle [50]. The device was not widely accepted as it did not provide substantial advantages over trephine needles. Despite the reliability of the Jamshidi needle suppressing advances in bone marrow sampling, a battery-powered bone marrow drill, the OnControl, was then released in 2007 [51]. Multiple clinical studies have been conducted to evaluate the performance of the OnControl powered drill and compare it with the trephine needles. Earlier studies by Berenson [52] and Swords [53] claim that the drill device yields superior specimens quicker than the Jamshidi. However, an independent study [54] found comparable sample quality and patient reported pain levels for both techniques. At three times the cost of the manual device, the powered drill has offered limited advantages [54].

The main challenge of performing a needle biopsy continues to be consistently obtaining a sample for analysis without causing excessive damage or pain for the patient. Additionally the large force required to penetrate cortical bone restricts the use of trephine needles near delicate structures. Ultrasonic surgical devices have proven capable of performing procedures where care and control is required which is why the ultrasonic biopsy needles will be investigated in this study.

2.2 The early development of ultrasonics

Ultrasonics is the branch of acoustics which describes sound waves above the range of human hearing. Pythagoras (580-500 B.C.), while widely credited as the "Father of Mathematics", is also considered the "Father of Harmonics". He was first intrigued by the notes produced by a blacksmith when using hammers of different weights. He proposed a mathematical explanation; ratios investigated by using strings of different lengths and densities [55]. Pythagoras was followed by Aristotle (384-322 B.C.), one of the first to claim that sound travelled in waves [56].

Modern acoustics was introduced during the 16th century by Italian physicist, Galilei who was the first to record the relationship between the frequency of the wave and the pitch it produces [57]. Following Galilei's work, French mathematician Mersenne studied the vibration of strings and was the first in 1640, to record the speed of sound as it travelled through air. Later in the 17th century, Hooke an English physicist provided an objective measure of pitch by producing a sound wave of known frequency measured using a rotating cog wheel [58]. Around the same time Swiss physicist Colladen determined the speed of sound in water using an underwater bell. These initial studies were carried forward and the study of sound was established as 'acoustics' by French physicist Sauveur who determined the relationship between frequency and pitch [59]. Perhaps the most significant paper in the field was published in 1877 by Lord Rayleigh. 'The Theory of Sound' defines the mathematics of sound waves, forming the basis of acoustics [60].

The study of frequencies outwith the limits of human hearing became an established topic during the 19th century. Despite this, it was first suggested by Spallanzani in 1794 who surmised that bats relied on their hearing to avoid obstacles in the dark [61]. Although dismissed at the time, he was the first to deduce the existence of sound waves inaudible to humans. French physicist Savart developed a system, now named the Savart wheel, to investigate the range of human hearing. It is deemed the first ever ultrasonic generator producing waves with frequencies up to 24 kHz [62]. Following this work, arguably the most significant development was conducted by Galton in 1883. The 'Galton Whistle' allowed Galton to roughly define the upper audibility limits of human hearing between 10 and 18 kHz [63]. While Galton's investigation gave the first marker, it was further investigated by Koenig in the late 1890s, using tuning forks capable of producing frequencies between 16 Hz

to 90 kHz [64].

It wasn't until the 1930s that Griffin and Galamos, two Harvard students under the supervision of physicist Pierce finally confirmed Spallanzani's theories, determining that bats generate and hear sounds an octave higher than the upper limit of human hearing. Griffin brought a cage of bats into Pierce's lab and the scientists discovered that the bats were emitting ultrasound. Coining the term "echolocation" Pierce developed one of the first devices which could detect sound waves with frequencies above the audible range of human hearing [65].

The discovery of magnetostriction and piezoelectricity also occurred in the 19th century, revolutionising the field of ultrasonics. Magnetostriction is a property of ferromagnetic materials that causes them to expand or contract in response to a magnetic field, first discovered by Joule in 1842 [66]. In 1880, the Curie brothers discovered the piezoelectric effect, the ability of some crystals to produce an electrical signal when mechanical pressure is exerted [67]. After being mathematically deduced by Lippmann one year later, the Curies then discovered the inverse piezoelectric effect in 1881. This is undoubtedly the most significant finding in ultrasonics, enabling the practical application of ultrasonics.

Following these discoveries, research and development was ignited by two major events. The first was the sinking of the Titanic, after it collided with an iceberg and the second was the start of World War 1. There was a need for a method of detecting obstructions at sea and submarines. The first patent for underwater sonar by Lewis Fry Richardson appeared a single month after the Titanic sunk [68]. The first operational sonar system was then realised by Fessenden in 1914, which could detect icebergs up to two miles away [69].

The most noteworthy developments during this time can be associated with Langevin. His use of high frequency acoustic waves and quartz resonators for submarine detection was the origin of modern ultrasonics. Originally proposed by Chilowsky, in 1915 Langevin developed an echolocation system with a resonant frequency of 150 kHz which consisted of a mosaic of quartz crystals glued between two steel plates [70]. This hydrophone was initially problematic as a sound projector as a large volume of quartz crystal and high voltage levels were required. Classified research activity from 1915-18 had Langevin continue to redesign and improve the hydrophone, which was employed extensively in the surveillance of German warships. This is now called the bolted Langevin transducer and was the first capable of sending and receiving

signals over long distances [71].

Post World War 1 research into ultrasound continued to steadily grow and extend across several fields. Cady [72], Pierce [73], Van Dyke [74] independently developed piezoelectric or crystal resonators. This followed the finding that quartz vibrating at resonance could produce an electrical signal with a very precise and stable frequency. One pioneer during this era was Sokolov, who explored the use of ultrasound technology for flaw detection within structures [75]. Perhaps the most significant development of this time in high power ultrasonics was achieved by Wood and Loomis, who developed an oscillator tube which was applied to several high-power applications, including etching, drilling and heating [76]. World War II forced those with expertise in ultrasonics to return their focus to sonar for anti-submarine warfare which stalled advances in other power ultrasonics application. However in the years following the war, development of medical applications would be fully pursued.

2.3 Power ultrasonics applications in surgery

Interest in ultrasonic surgery can be dated to 1952 when Catuna utilised an ultrasonic industrial impact grinder, originally patented by Balamuth, to drill extracted teeth [77]. This led to the invention of a specialised dental device in the form of a magnetostrictive Langevin transducer which delivered a longitudinal vibration to a straight cutting tip and a composite longitudinal-flexural motion by using a curved tip [78]. In 1955, Zinner performed early trials with an ultrasonic device capable of eradicating deposits from the tooth surface [79]. Improvements made by Johnson and Wilson two years later allowed the ultrasonic scaler to be conceived for the removal of calculus and plaque [80]. At the time it was reported that applying the device to the tooth surface with a large force had the potential to cause damage to the root surface and dentine.

Alongside studies on scaling, the application of ultrasonic endodontic instruments for bone cutting also occurred in the 1950s. Introduced by Richman in 1957 the technique gained patient acceptance posing as an alternative to an abrasive slurry [81]. In later years Martin et al. pioneered a system for root canal treatment based on using an ultrasonic generator to energise a file or diamond inserts, with irrigation to remove debris, cleanse and disinfect [82].

Parallel to the studies within dentistry the first investigation into using ultrasonics for

other surgical applications were being conducted by Lindstrom who was the first to describe an ultrasound-based system for neurosurgery in 1954 [83]. A substitute for lobotomy, ultrasound irradiation was applied via a hole in the patient's skull leaving no lesions or permanent changes in brain function. Brothers William and Frank Fry whose interest also lay in neurosurgery conducted tests on animals exploring the use of focused high intensity ultrasound to perform craniotomies [84]. The work conducted by the Fry Brothers was advanced a few years later by Meyers who was the first to conduct neurosurgery on humans [85].

The first use of high power ultrasonics to mechanically fragment tissue was reported by Kelman in 1967 [14]. This was the first study to describe modern day phacoemulsification now an established cataract surgery. Around the same period, the potential of cutting tissue with an ultrasonic scalpel was investigated by Poljakov [86]. Successful cutting trials were performed with an axial vibrating ultrasonic instrument with a vibrational amplitude of 30 – 60 μm at frequencies between 22 and 30 kHz. In 1974 Volkov [87] investigated using a surgical device driven with a 25 - 30 kHz longitudinal vibration to perform simple orthopaedic operations. In 1978, Flamm et al. utilised a modified phacoemulsification unit to investigate the effect of ultrasound on the brain and spinal cord tissue of a cat [88]. Interest continued to thrive through the 1980s with examples including the use of an ultrasonic scalpel for liver surgery [89], an ultrasonic aspirator for endoscope surgery [90] and an ultrasonic lithotripter for fragmenting urethral and bladder stones allowing them to be naturally passed [91].

Although initially proposed by Vang in 1955 [92] the use of power ultrasonics in bone cutting outside dentistry was limited and irregular. Volkov evaluated the use of an ultrasonic cutting instrument to simplify cutting hard tissue in 1974 [87]. This was followed by Aro in 1981 in orthopaedic surgery [93], and Horton in maxillofacial surgery [94]. Perhaps the most encouraging study was conducted by Khambay and Walmsley who developed an ultrasonic bone chisel [95], [96]. Their research showed a desirable cutting rate compared with conventional rotary burs, while reducing the required cutting force. Despite these findings the mainstream uptake of ultrasonics did not occur until the millennium.

The first device to appear on the market was patented in 2001 by Vercellotti, a maxillofacial surgeon and Mectron S.p.A [97]. Clinical studies showed that the Piezosurgery Device® could cut delicate bone structures with precision without damaging surrounding soft

tissue [98], [99] and [100]. The Piezosurgery device inspired several other ultrasonic surgical devices for cutting bone such as the Misonix BoneScalpel commercialised in 2013 [101], shown in Figure 2.2.

Figure 2.2: Misonix BoneScalpel® [101]

The advantages of the devices, found through clinical studies can be summarised as the improvement of cutting accuracy [98], [100], the reduction of cutting force [95], [102], the reduction of cutting damage to the bone and surrounding soft tissues [103], [104] and the reduction of bleeding [105].

Bone drilling is a common orthopaedic procedure where fractured bone segments are treated by drilling the bone to insert a screw and fix the fractured parts. During the procedure considerable force is required which results in significant heat production. The increase in temperature can cause osteonecrosis which can reduce the stability and strength of the fixation [106], while high levels of compressive force and torque can generate micro-cracks degrading the structure of the bone. To solve these problems, an ultrasonically assisted vibrational bone drilling technique has been proposed [39]. In a laboratory setting, Alam et al found that utilizing an ultrasonic assisted drill could reduce the force required during penetration and the temperature at the site compared to a traditional drilling device [107], [108].

2.4 Ultrasonic component design

Literature provides a strong insight into the design of resonant transducers which possess a small lateral dimension compared to the tuned length. This strongly applies to a long, thin ultrasonic needle. The first attempt to obtain numerical solutions for the displacement amplitude produced by ultrasonic horns was presented by Merkulov [109] and Balamuth [110] independently in the 1950s. Different profiles of ultrasonic horns; conical, exponential and catenoidal, were considered. Equations were established to calculate the resonant length and

the particle velocity gain coefficients. Balamuth concluded that the stepped horn provided the largest vibrational gain, while Merkulov reported larger amplitude gains for a catenoidal profile. Both reported that gain was constrained by the strain limit of the horn material. Merkulov continued his research alongside Kharitonov describing the design process and experimental data of increasingly complex horn profiles which achieved higher amplitude gains [111]. Merkulov's research was further advanced in the 1960s by Ensminger, who developed equations for the particle velocity, particle velocity amplification, stresses, component length and mechanical impedance for half wavelength solid cones [112].

In the early 1960s, within correspondence in the journal Acustica, Neppiras compared concentrators of different profiles based on the choice of material [113], [114]. Titanium was prevalent due to its low internal losses and high stress endurance. Approximately two decades later, Amza and Drimer published work obtaining accurate expressions of the resonant frequency for various horn profiles. The design and material choice of tapered horns was scrutinised seeking a closer correlation between calculated and experimental results [115]. A significant finding of this work was that undesirable torsional and radial vibrations can couple with the longitudinal vibrations. In 1990, Muhlen published work concluding that concentrators should not be too slender so to avoid lateral modes of vibration which could damage the device [116]. Muhlen also advised that a stepped horn may have low energy transfer factors because of the intense stresses at the junction which cause fractures in the material.

Finite element modelling (FEM) and simulation became a crucial tool in transducer design in the 1980's enabling more complex geometries to be considered. In 1991, O'Shea was one of the first to use FEA to design ultrasonic horns to study the effect of the quantity, position and size of slots in block horns on the uniformity of the amplitude [117]. In 1995, Amin et al, created an FEA based optimisation procedure to maximise the vibration magnification though different horn profiles. The geometrical shape of an axisymmetric ultrasonic machining horn was optimised to maximise magnification, for higher rates of material removal and to ensure safe working stresses [118].

Another key area in the characterisation of ultrasonic transducers is the ability to measure the vibration response. Developments in laser technology in the 1980s and 1990s, specifically the invention of the laser Doppler vibrometer (LDV) and electronic speckle pattern

interferometer (ESPI), enabled the non-contact measurement of ultrasonic vibrations. Laser Doppler vibrometry operate using optical interference where two coherent light beams, a measuring beam and a reference beam, are manipulated to detect the motion amplitude and direction. Lucas at al were one of the first to apply ESPI and one-dimensional (1D) LDV to analyse the vibrational response of ultrasonic horns and validate the response predicted using finite element models [119], [120], [121], [122] and [123]. Three-dimensional (3D) LDVs enabled further progress in ultrasonic tool design, allowing a more detailed characterisation of the vibration response. The 1D LDVs can measure the out of plane velocity or the normal-to-surface response. While 3D LDV can measure three mutually orthogonal components of the vibration response, allowing the in-plane modes to be captured. The single-point 3D LDV consists of three separate laser beams, oriented in three non-collinear directions which are manually focused on a single point on the measurement surface.

2.5 Materials: Piezoelectric

Since piezoelectricity was discovered in the 1880s a variety of piezoelectric materials have been utilised to exploit the phenomenon for a variety of applications. Underwater acoustic devices developed during WW1 were made using quartz and Rochelle salt single crystals. These were the only piezoelectric materials available in the early 20th century, both with limiting factors. Rochelle salt have a small temperature operating range and quartz commonly requires an unrealistic geometry. Post WW1 a search for a stable and reliable alternative led to Busch's discovery of potassium dihydrogen phosphate (KDP) in 1935 [124]. Busch theorised that ferroelectricity in Rochelle salt originates from the hydrogen bonds, which KDP also possessed. Similar water-soluble single crystal materials would be uncovered as piezoelectric during this period including; ammonium dihydrogen phosphate (ADP), ethylenediamine tartrate (EDT) and dipotassium tartrate (DKT), however these would soon be dwarfed in performance by synthetic quartz and ceramics.

Barium titanate (BaTiO3, BT) ceramics were discovered in the 1940s independently in the United States, Japan and Russia [125]. World War II prompted a requirement for compact high-value capacitors for radar systems which led to doping of oxides seeking high permittivity. BaTiO3 possessed a permittivity of ten times that of Titacon (TiO2-MgO) which at the time was the most widely used. Incorporating BT in transducers was initiated

when its piezoelectricity was verified by Gray in 1946 and was accelerated by its ease of manufacturability and superior dielectric, ferroelectric and piezoelectric properties [126]. However, the application of BT was affected by its small operating temperature range.

The same methodology which caused the discover of BT resulted in the discovery of PZT (lead zirconate titanate) only a decade later. Sawaguchi et al were the first to determine the phase diagram of Pb(Zr, Ti)O3 which led to Jaffe's discovery of its superior piezoelectricity in 1954 [127]. The success of PZT was made possible through advances in material science techniques which included an understanding of the relationship between perovskite crystal structure (a fundamental crystal lattice structure) and the electro-mechanical behaviour. Scientists have also developed the ability to precisely dope ceramics with metallic impurities to achieve the desired properties. PZT material had greater sensitivity and higher operating temperatures and could be tailored to a specific application's needs regarding dielectric constant, stiffness, piezoelectric coupling coefficients and ease of poling.

A comprehensive insight into the wide range of possible compositions was published by Jaffe et al in 1971 [128]. The ceramics fell into two general categories, 'hard doped' or 'soft doped'. Soft ceramics have high piezoceramic constants and are suitable for static applications where large amplitudes are required. However, they suffer from high losses which can cause overheating making them unsuitable for resonant applications. For high-power ultrasonic resonant applications, including surgical devices, hard materials are best suited. Hard doped piezoceramics possess a high mechanical quality factor, large electromechanical coupling factor and an improved stability over soft ceramics coupling, however they produce smaller displacements.

The U.S. Navy was prominent in the classification of these ceramics due to their usefulness in undersea warfare. Materials were categorised as 'Navy Type PZTs', defined in technical standard MIL-STD-1367B realised in 1995. Despite this standard being cancelled only four years later the 'Navy Type' classification remains widely used by manufacturers to classify their PZT materials. The standard classifies a piezoelectric ceramic based on its physical and electrical properties as opposed to their chemical composition. Hard-doped ceramics, Navy Types I and III, also called PZT8 and PZT4, remain the most widely used in high power ultrasonic applications [129]. PZT8 is popular for resonant devices due to its high mechanical quality factor and its ability to handle high levels of electrical excitation and

mechanical stress.

PZT remains the most widely used piezoceramic material despite environmental concerns as it contains lead oxide, a hazardous and toxic material. Investigations into lead-free alternatives to PZT have been conducted since the 1950s but materials with comparable performance attributes could not initially be found. Extensive research over the past two decades devoted to developing lead-free piezoceramic materials has led to alkali metal-based bismuth sodium titanate (BNT), bismuth potassium titanate (BPT) and potassium sodium niobite (KNN) [130], [131]. However, these materials possess a poor operational temperature range, a high corrosiveness and low piezoceramic properties in comparison with PZT, thwarting their significant uptake.

The most promising findings have occurred more recently with relaxor ferroelectric single crystals such as PZNT (lead zirconate titanate - lead zinc niobate) and PMNT (lead magnesium niobite - lead titanate) which possess high electromechanical coupling factors and piezoelectric coefficients. New ternary single crystal, PIN-PMN-PT (lead indium niobate–lead magnesium niobite – lead titanate) have ignited interests in the field. With superior properties to PZT, these materials have prompted the design of a new generation of ultrasonic transducer technologies previously deemed unachievable [132], [133]. Characterisation of these crystals and therefore a comprehensive understanding of their full potential is ongoing.

2.6 Materials: Biocompatibility

Biocompatibility is a significant consideration in the design of any device, instrument or piece of equipment used to treat, augment or replace a tissue, organ or function of the body [134]. Historically the choice of material was based on availability, such as wooden teeth, glass eyes or surgical instruments made from bronze, iron or steel. By the early twentieth century the naturally derived materials were replaced by synthetic polymers, ceramics and metal alloys [135]. Better performance, functionality and ease of reproduction led to an increase in the range of applications for biomaterials including contact lenses, artificial hips and dental implants.

Using metal for medical purposes is considerable and spans a range of applications despite environmental and health concerns over heavy metals. Technological advances in developing

ceramics and polymers have made it possible to manufacture implant devices from these materials. However, the strength, toughness and durability of metals over ceramics or polymers have maintained their popularity for surgical tools. As surgical tools require a toughness and corrosion free surfaces [136] it is conventional to see such tools manufactured using stainless steel or titanium alloys.

Stainless steels contain carbon, chromium, nickel manganese, iron and other minor components, a composition to ensure strength, corrosion-resistance and durability. Stainless steel has been utilised in surgical instruments since its formulation in the early 20th century, and steadily became the material of choice [137]. Titanium and titanium alloys, the most common being Ti-6Al-4V, are highly ranked in terms of biocompatibility due to their high strength to weight ratio and outstanding resistance to corrosion. Titanium first featured in medicine in dental implants in the 1940s then in prosthetics a decade later. In 1952, Brånemark discovered that titanium could integrate into the body without a negative immune response [138]. As titanium is lightweight and strong it is ideal for surgical instruments as it is simpler to handle during long or repetitive tasks. Acoustically, Ti-6Al-4V is considerably less lossy than steel which has resulted in its popularity in ultrasonic surgical devices since the first devices in the 1970s. For example, the CUSA employed a hollow titanium tip vibrating along its longitudinal axis [139].

2.7 Composite modes of vibration

The first high power resonant ultrasonics devices designed during the 1950s operated in a single mode of vibration, typically longitudinally. A decade later in 1964 Mason proposed a transducer for ultrasonic welding and drilling which vibrated with rotational and longitudinal motion. The geometry of the tapered horn of the device was designed so the frequency of a longitudinal mode and a torsional mode occurred close together, encouraging them to couple. In 1969, Rozenburg proposed an improved technique by achieving a longitudinal-torsional vibration by degeneration. Rozenburg applied a groove pattern to form a helix on the horn [140], which induced a torsional vibration when excited axially. The resultant frequency response exhibited an L mode and a T mode close in frequency. The composite L-T vibration was produced by exciting the system between the L and T resonant frequencies. Initially, a prevalent area of interest in using multiple modes of vibration was in ultrasonic

motors. First introduced in the early 1970s by Barth [141], multiple piezoceramic resonators drove the rotor to operate in different directions. Utilizing multiple transducers as positioners for rotors advanced throughout the 1980-90s, developed with enhanced precision and efficiency [142], [142], [143].

In 1978, Gallego-Juarez proposed an ultrasonically powered stepped plate for high power air-coupled applications in gases [144]. When longitudinally vibrating emitters could not achieve the large amplitudes required, high intensity ultrasonics was excited through flexural motion via a stepped circular plate with three nodal circles. While the range of applications expanded so did the variety of techniques used to generate complex modes of vibration. Initially introduced in 1989 by Ueha, then improved by Shuyu in the 1990s, two sets of piezoelectric discs differently polarised were used to achieve a composite vibration. Incorporated as a single sandwich transducer, the first set was poled in the thickness direction to generate the axial vibration whilst a second set is poled tangentially to generate the torsional vibration [145], [146]. The technique produced a high level of torsional motion but the different sets of piezoceramic were difficult to drive and control in unison when operating under load. In 1993, Watanabe proposed a similar design for a longitudinal-flexural complex-mode high-power ultrasonic transducer [147]. The device was constructed with two sets of ceramics, one to generate longitudinal vibration and one to generate the flexural motion, precisely located at the node of the respective vibration modes.

Through the 1990s into the early 2000s Tsujino was developing complex mode devices based on a mode degeneration approach [148–154]. Tsujino noted the potential for unwanted coupling with parasitic modes to occur by introducing the slits due to the reduction in stiffness, an important consideration when designing a device slender in geometry. Similar composite modes of vibration were considered and patented for cutting tips of surgical devices in the early 1990s [155–157]. In 1993, Wuchinich used a transverse ultrasonic motion combined with rotation to cut collagenous tissue such as cartilage and the meniscus. Wuchinich followed this work with the proposal of an ultrasonic tissue dissection device with a tip vibrating in a combined longitudinal and torsional motion. Utilizing a different technique Boukhny, realised a device which produced both longitudinal and torsional motion at the cutting tip for enhancing tissue dissection, which required two electrical generators to power two transducers [157].

Complex mode vibrations are commonly found in ultrasonic surgical devices, where a longitudinal-flexural or longitudinal-torsional motion improves the tissue-tool interaction. Piezosurgery® technology by Mectron utilises a bend in the cutting inserts which results in a longitudinal-flexural composite vibration mode, with a variety of tip bend geometries available dependent on the surgical application [158]. The spetzler claw bone tip of Stryker's Sonopet ultrasonic aspirator vibrates in a longitudinal-torsional motion achieved by degenerating the axial vibration into torsion through helical slots around the insert's shaft [159]. Strategies for the optimal design of longitudinal-torsional ultrasonic devices using helical cuts have been recently investigated by Harkness and Al-Budairi [160–163] and the potential of these approaches will be considered to improve the tip-tissue interaction of the bone biopsy needle in this study.

2.8 Driving conditions

Frequency control of an ultrasonic vibrating system must ensure the system is driven in resonance. High power ultrasonic transducers generally have a high Q factor associated with a narrow operational bandwidth. During operation the temperature and load will cause changes to the operational characteristics of the device which causes the resonant frequency to shift.

Ramos-Fernandez et al developed a technique in 1985 to dynamically maintain resonance of a stepped plate transducer [164]. The phase of the motional admittance of the system is kept at zero by adjusting the driving frequency. This provided the basis of resonance tracking widely used for driving ultrasonic systems [165–168]. Babitsky et al pioneered auto resonant control of ultrasonically assisted machining under variable cutting loads [169–171]. Resonance is obtained by matching the oscillating system with the dynamic loads imposed by the cutting process.

A multitude of systems have since been adopted including a software-based resonance tracking and vibrational stabilization system which can drive high power ultrasonic devices by Kuang et al. The system can be adopted by any ultrasonic transducer to lock the impedance phase at zero and stabilise the vibration amplitude by maintaining the motional current constant even when in contact with various loads [172] and [173]. A developed version of such a system will allow the ultrasonic needle devices realised throughout this research to be

evaluated.

2.9 Chapter conclusion

Over recent decades ultrasonic devices have become an established surgical technique offering numerous advantages, such as increased safety, precision and quicker healing. This thesis will describe the development of ultrasonic resonant bone biopsy needles. The device could penetrate hard bone tissue with precision, accuracy and without applying significant force down through the needle device to penetrate the bone.

The design and characterisation of full wavelength ultrasonic needle configurations are described in Chapters 3 and 4, achieved through finite element analysis, experimental modal analysis and harmonic analysis. Penetration tests within bone mimic and animal bones provide evaluation of these devices with the biopsy retrieved and penetration site damaged visualised through μCT. This cumulates in a case study, described in Chapter 6, into the surgical approach of the petrous apex adapting the ultrasonic resonant needle to fit the needs of the application.

Chapter 3

Design procedure for ultrasonic needle devices

Ultrasonic devices are routinely used to cut biological tissues, however the creation of an ultrasonic bone biopsy needle is challenging. Sufficient vibrational amplitude to penetrate mineralised tissue must be maintained without inducing a flexural response. The needle must be capable of penetrating 5 mm which represents a through penetration of the cortical bone of a typical human femur. Optimal design variables are sought to maximise the performance and stability of the device.

Early transducers were designed through either analytical modelling, an iterative prototype process or a combination of both. Analytical models utilise wave equations to approximate the geometric dimensions required for resonance at the ultrasonic frequency while the principle of wave propagation is used to investigate impedance matching and hence determine the material of each component. Both approaches commonly require unrealistic assumptions to simplify the transducer before analysis. Experimental prototypes were typically designed, analysed and modified until an acceptable solution was attained. The process was time and labour intensive and did not achieve the best possible design. Numerical analysis based on FEA was introduced for modelling of piezoelectric materials and devices in the 1970s. Mathematical analysis of the vibrational response is approximated by subdividing the domain into smaller elements that together forms a mesh representing the entire structure. Calculations are conducted for each element and combined to produce the result.

Initially the design of Langevin transducers are analytically proposed following half

wavelength synthesis. The device represents a full wavelength resonator consisting of a half wavelength Langevin transducer and a half wavelength needle insert. The geometry and materials are initially deduced based on high acoustic transmission, low mechanical loss and high strength. FEA is then used to model and optimise the geometry of the full wavelength ultrasonic needle. The device geometry is configured to ensure that it operates at the desired tuned frequency. Full wavelength slender devices possess high modal densities thus careful consideration of the tool geometry is required.

The longitudinally tuned vibrating needle is then reconfigured into a composite longitudinal-torsional device by adjusting the profile of the front mass and needle. The final design is chosen based on maximising the torsionality and large frequency spacing between the mode of interest and the neighbouring modes.

3.1 Design criteria

For the ultrasonic biopsy needle the design criteria were set:

3.1.1 Mode shape separation

The ultrasonic needle devices consist of a half wavelength Langevin transducer driving a half wavelength needle insert. Slender full wavelength devices have a higher likelihood of suffering from modal coupling than half wavelength devices due to the higher modal densities they exhibit. Two factors influence the chance of modal coupling occurring, the closeness or frequency spacing between two or more natural frequencies in the frequency spectrum and the damping of each mode, which is related to the sharpness of the resonance peak. Figure 3.1 shows alternate frequency spectrums with two modes, f_1 and f_2 separated by Δf. Low damping, high Q in Figure 3.1(a) suggest that each mode would be excited without coupling. While high damping, low Q of the modes, shown in Figure 3.1(b) shown significant coupling between f_1 and f_2 .

The resonant frequency and frequency separation between modes will both alter when operating caused by heat generation at the interaction between the load and the device and self-heating of the device itself. To reduce the likelihood of modal coupling a frequency separation of 10% between the tuned and neighbouring modes of vibration is set. If sufficient frequency spacing is not achieved there is also an increase likely of jumping to a parasitic

mode when being driven using resonance tracking.

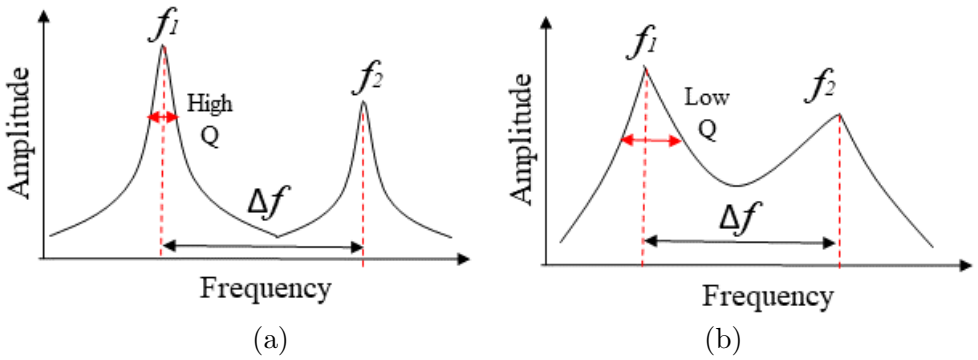

Figure 3.1: (a) High Q (b) low Q modes with same frequency separation

3.1.2 Torsional motion

Throughout this thesis torsion is measured using the tangential component of displacement at the needle tip. Torsion is then defined as the ratio of tangential to longitudinal vibrational displacement at the tip of the needle insert. For the ultrasonic bone biopsy device, the aim is to enhance the tip-tissue interaction by a employing a continuous torsional motion. It is proposed that a longitudinal-torsional (L-T) motion at the tip of the needle will aid debris removal and avoid the needle imprinting and stalling in the bone. The intention is to produce torsional (T) vibration by degenerating longitudinal (L) vibration into a combination of L and T vibration by incorporating helical cuts. However, these cuts will reduce the mass of the device and decrease its axial stiffness. The design should produce high torsional response while maintaining sufficient frequency spacing and longitudinal vibration. In ultrasonic drilling and thus for this application, it is desirable for the torsional response to be equal to the longitudinal response to fully exploit the advantages of inducing torsion.

3.1.3 Geometry

The geometry of the hand-held needle must be ergonomic offering dexterity, precision and comfort. Assuming a cylindrical handle, a smaller diameter helps with dexterity while a mass of around 0.5 kg offers precision and comfort. Alongside these considerations, the two factors which lead the design of the transducer is the resonant frequency and available piezoelectric rings.

To retrieve a sufficient biopsy size and allow a direct comparison the tip geometry is designed to be comparable with trephine bone biopsy needles. The gauge of trephine needles can vary between 8-13, equivalent to an outer diameter (OD) between 4.2 and 2.4 mm and inner diameter (ID) between 2.4 and 1.8 mm. The needle prototypes developed will vary in size within this range, although manufacturing limitations may restrict the creation of particularly slender geometries.

Class of prototypes

Initially two longitudinal mode devices were designed for fabrication. Ultrasonic needle 1 (USN1) which has a tip comparable with an 11 - gauge trephine needle which has a 3.0 mm OD and 2.3 mm ID, and a larger ultrasonic needle 2 (USN2) which is comparable with a 9 - gauge biopsy needle representing a 3.7 mm OD and 2.9 mm ID. Two versions of USN2, the larger of the two transducers, were designed one with a stainless steel needle insert and second with a titanium needle insert, USN3. USN3 is then adapted to form a composite longitudinal-torsional device, ultrasonic needle torsional (USNLT).

3.1.4 Summary of the design criteria

Mode separation	Frequency separation of 10% around the mode of interest to avoid coupling with surrounding parasitic modes.
Torsionality	Torsional response at the tip of the needle as close to equal the longitudinal response as possible.
Geometry	Needle should be ergonomic to offer dexterity, precision and comfort with a mass of around 0.5 kg. The tip should be comparable with that of a trephine bone biopsy needle, OD between 4.2 and 2.4 mm and ID 2.4 and 1.8 mm.
Class of prototypes	Four prototypes will aid validation of the efficacy of ultrasonically resonant needles and investigate the use of torsionality.

Table 3.1: Summary of design criteria

3.2 Design of a Langevin ultrasonic transducer

Langevin transducers, also called sandwich transducers are extensively used in high power ultrasonic applications. This is due to high electromechanical conversion efficiency and durability. As illustrated in Figure 3.2, a Langevin transducer consists of one or more pairs of longitudinally polarised piezoceramic rings, connected mechanically in series and electrically in parallel using electrodes. When an electric field is applied in the polarization direction of the piezoelectric elements, a mechanical deformation in the thickness direction occurs. The end masses and piezo rings are held under a compressive preload by a bolt which prevents tensile stress and gaping. The transducer design procedure is outlined in the sections to follow.

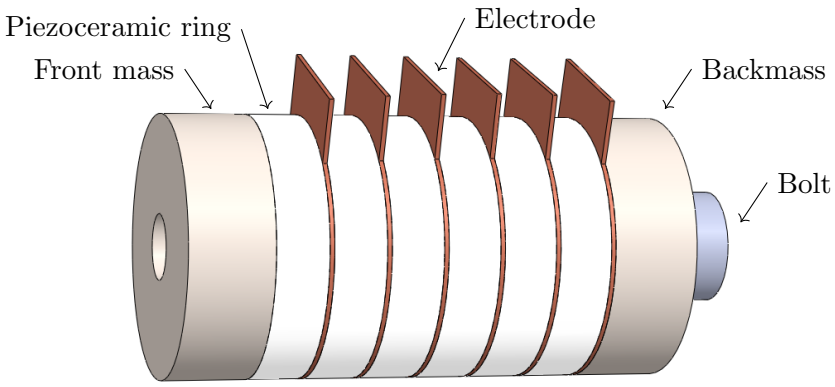

Figure 3.2: Configuration of a Langevin ultrasonic transducer

3.2.1 Resonant frequency

A power ultrasonic device operates at a single frequency, between 20 and 100 kHz. The relationship between the wavelength and the resonant frequency of a resonator with uniform cross section is expressed as:

$$\lambda = \frac{c_L}{f} \tag{3.1}$$

where c_L is the wave velocity of longitudinal vibration, which depends on the mechanical

properties of the resonating medium, calculated by:

$$c_L = \sqrt{\frac{E}{\rho}} \tag{3.2}$$

where E is the Young's modulus and ρ is the density. The wavelength is used to estimate the required length of the resonator. Langevin transducers are commonly designed as half wavelength devices. The transducers in this study are designed as half wavelength transducer connected via a threaded joint to a half wavelength resonant needle. Equations 3.1 and 3.2 provided an initial approximation of the device length.

3.2.2 Piezoceramic components

Piezoceramic components, which can be in the form of plates, disks or rings, convert an alternating electrical voltage into mechanical oscillations. For high power ultrasonic transducers, PZT is the most commonly used piezoelectric ceramic. Hard PZT materials are commonly selected for high power ultrasonic transducers due to the high mechanical quality factor, large electromechanical coupling, high dielectric constant and high Curie temperature. The mechanical quality factor the reciprocal of the mechanical loss factor, can be assumed as the amplification factor of piezoelectric rings operating in resonant conditions. The electromechanical coupling factor depicts the ability of the material to convert electrical energy to mechanical energy, while the dielectric constant or permittivity is the dielectric displacement per unit electric field. The Curie point is the temperature at which the material loses its piezoelectric characteristics. PZT8 rings (CeramTec) are selected, recommended for high power ultrasonic applications with a Curie temperature of 300°C, mechanical quality factor of 1200 and dielectric stability defined by a relative permittivity of 1000.

For high power ultrasonic transducers operating in a longitudinal vibration mode, literature suggests that the diameter of the piezoceramic ring should be less than a quarter-wavelength to avoid flexural coupling [174], while the total thickness of the piezo-ceramic stack should be less than one tenth of the wavelength to achieve high electromechanical coupling [175]. To select suitable piezoceramic rings, the length of the transducers, are approximated as 180 mm and 220 mm respectively to achieve a suitable resonant frequency. The geometry of PZT8 rings selected for each ultrasonic device in this study are listed in Table 3.2.

	Outer diameter (mm)	Inner diameter (mm)	Thickness (mm)
USN1	16	7.2	2
USN2	20	8.2	4

Table 3.2: Piezoceramic rings of each device

3.2.3 Electrode

To assemble a Langevin transducer the piezoceramic rings are connected in parallel to the power source using thin conductive discs, mesh or epoxy. Copper discs pose the simplest construction while also providing arguably the most consistent coupling across the face of the piezoceramic ring. The thickness of the electrode has a significant effect on its operation, increasing the thickness of the electrode improves the heat dissipation between the piezoceramic elements but has negative effects on both the electromechanical coupling coefficient and mechanical quality factor [145]. The thickness of the electrode should be carefully selected to balance both factors.

3.2.4 Bolt

The pre-stress bolt is an integral component in Langevin transducers. The main role is to deliver a pre-stress to the stack to avoid tension in the PZT rings. The mechanical pre-stress of the piezoelectric elements decreases the electrical impedance of the transducer and increases the potential power intensity. The bolt is key in preventing fracture of the PZT rings during cyclic loading while also decreasing mechanical losses between the transducer parts.

The amount of pre-stress of the piezoceramic rings is critical. Insufficient pre-stress results in the transducer exhibiting high impedance and low fatigue life. Excessive pre-stress can cause depoling of the piezoceramic rings and tensile bolt failure. Typical pre-stress values of the piezoceramic materials range from 20 MPa to 30 MPa.

The bolt material should be selected based on low axial stiffness, high fatigue and high yield strength. The electromechanical coefficient is maximised when the bolt has a low stiffness compared to the piezoceramics. High fatigue strength must accommodate the combined static preload stress and ultrasonic stress in the bolt. Yield strength is additionally

important as losing preload occurs during yielding before the bolt breaking [176]. Titanium would be optimal choice but is expensive, thus steel bolts will be used.

3.2.5 End masses

While the piezoelectric rings represent the vibrational generation elements, the metal end masses represent the vibration transmitters. The material must have a high fatigue strength, which is essential when being subjected to high cyclic loading. Additionally, a high mechanical quality factor, the inverse of the acoustic loss factor, is important. A high mechanical loss factor increases heat generation during operation and reduces the efficiency of the acoustic energy transmission. High tensile strength is also key for cutting and drilling applications when the target is a material with high compressive strength. Table 3.3 shows a list of common materials for the end masses of ultrasonic transducer and the properties.

Material	Tensile Strength (MPa)	Fatigue Strength (MPa)	Loss co-efficient (x 10^{-4})	Quality Factor Q_M
Titanium Ti-6Al-4V	850	410	1.4	7134
Stainless steel	600	270	4.6	2174
Aluminium 7075	572	159	3.0	3333
Tool steel	740	333	3.8	2632

Table 3.3: Properties of typical end mass materials [177], [178]

Stainless steel is low cost with relatively high strength and durability. Both varieties of steel (stainless and tool steel) have high fatigue strength but low quality factor. Acoustic loss in the horn causes heat which could be transferred to surrounding tissue; an undesirable effect. Aluminium alloy 7075 possesses a comparable quality factor, and tensile strength however higher loss coefficient and lower fatigue strength than the other potential choices. Titanium alloy Ti-6Al-4V is superior to the other materials for all four characteristics and is therefore selected for the end masses and needle inserts. Despite this, stainless steel is considered for the first prototype due to the unavailability of medical grade thick-wall titanium tubing with a small internal diameter .

An important consideration when designing the ultrasonic transducer is how the end masses interact with the piezoelectric material. The acoustic properties should be matched

to effectively transmit acoustic energy and minimise internal reflections of the stress wave. These equations are used to achieve acoustic matching [179].

$$Z_p = \sqrt{Z_\mathrm{b} Z_\mathrm{f}} \tag{3.3}$$

where Z_p, Z_b and Z_f are the acoustic impedances of the piezoceramic, back mass and front mass, respectively. These are calculated by multiplying the characteristic acoustic impedance Z_o by the cross-sectional area of the part, where Z_o is the product of the material density ρ and wave velocity c. The acoustic impedances of the transducer materials are listed in Table 3.4.

Material	Acoustic impedance x10^6(kg/m^{2}s)
Ti 6Al-4V	31.5
PZT8	29.9
SS 316	39.2

Table 3.4: Acoustic impedance of the transducer material

The transducer configuration of titanium-PZT8-titanium results in $\sqrt{Z_\mathrm{b} Z_\mathrm{f}} = 31.5\text{x}10^6(kg/m^2s)$. This is an error of less than 1% compared with the acoustic impedance of PZT8, $29.9\text{x}10^6(kg/m^2s)$.

3.2.6 Geometry of the transducer

Two factors generally determine the dimensions of a Langevin transducer; the wavelength and the required vibrational amplitude. The outer diameter of the back mass and electrodes should match that of the piezoceramic rings. The inner diameter of the end masses should be less than that of the piezoceramic rings and a gap between the bolt and the piezoceramic rings is required for electrical tape to be added to avoid an electrical short, shown in Figure 3.3.

The length of the Langevin transducer is usually one half wavelength. The back mass is usually a simple cylinder, while the front mass can be a more complex shape. A flange allows for attachment of the transducer to a housing and is generally located at the nodal plane so as not to influence the vibration. The remainder of the transducer front mass for the ultrasonic needle devices consists of an ultrasonic horn which is a tapered metal bar used to amplify the vibration amplitude. The cross-sectional area of the horn decreases to achieve

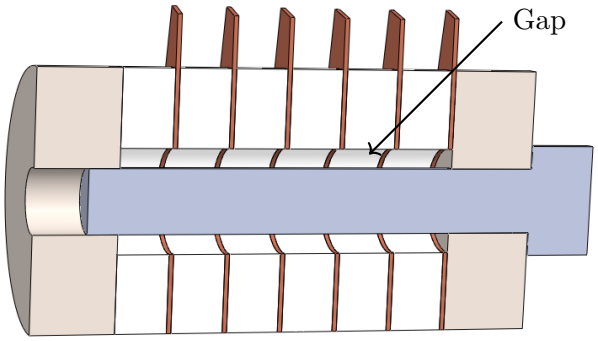

Figure 3.3: Sectioned view of the inside of a transducer

a tip radius comparable with a biopsy needle.

Three common horn shapes are used in high power ultrasonics; stepped, conical and exponential illustrated in Figure 3.4. The stepped horn consists of two sections with uniform cross-section and produces the largest amplitude gain of all the profiles, however a high stress concentration is induced at the step. This horn profile is usually therefore modified to include a fillet to reduce stress at the diameter change. The conical and exponential horns produce lower amplitude gain than a step horn but do not suffer from high stress concentrations. Combinations of these profiles (e.g. step-conical) are also common.

Figure 3.4: (a) Step, (b) conical and (c) exponentially shaped horn

FEA of the ultrasonic transducer will determine the final geometries of the end masses.

3.3 Modelling the ultrasonic transducer

FEA platform, Abaqus CAE, is used for modelling and analysis of the Langevin transducer. Initially a CAD model of the ultrasonic transducer is created defining the geometry and material properties of each component. The interaction between components and electrical boundary conditions are defined allowing the natural frequencies or eigenvalues of the ultrasonic transducer to be predicted.

3.3.1 Defining material properties

Defining a metal material for vibrational analysis is achieved by providing the general mass, in the form of the density and mechanical elastic properties, Young's modulus and Poisson's ratio. For analysis of the piezoceramic materials, the mechanical, electromechanical and electrical characteristics are defined by the elastic properties, piezoelectric properties, the electrical permittivity (dielectricity) and the density.

As piezoceramic materials are orthotropic, in FEA they are expressed in tensor notation. The order of a tensor, also described as the degree or rank, is the number of indices required to label a component of the array. For example, density is a scalar quantity represented by a single number and therefore considered a zero-order tensor. A fourth order tensor C_{ijkl} is used to represent the elastic stiffness constant of an orthotropic material. A compressed form is normally adopted by replacing the notation ij and kl with p or q respectively. Abaqus FEA requires that the material properties data is converted to the tensor form according to Table 3.5. Subscripts 1, 2 and 3 represents x, y and z in a rectangular coordinate system, while 4, 5 and 6 represent shear directions xy, xz and yz, respectively.

p or q	ij or kl
1	11
2	22
3	33
4	12
5	13
6	23

Table 3.5: Matrix to tensor form conversion

Elasticity

The modulus of elasticity C_{ij} is the ratio of the mechanical stress to the strain in the material. For the elastic modulus, the first subscript, i, indicates the stress direction while the second, j, indicates the strain direction.

For piezoelectric materials, the elastic modulus and elasticity compliance can be evaluated under a constant electrical displacement C_{ij}^{D} and s_{ij}^{D} respectively or a constant electric field C_{ij}^{E} and s_{ij}^{E} respectively, here the superscript D indicates a constant electrical displacement (open circuit) and superscript E indicates the constant electrical field (short circuit).

In Abaqus, the elastic modulus at constant electric field, C_{ij}^{E} is adopted and defined in the tensor form, D_{ijkl}. The data for D_{ijkl} of PZT8 is shown in Table 3.6, based on the data supplied by the manufacturers.

Piezoelectric properties

The piezoelectric properties of the piezoceramic material defines the relationship between the electric field and the mechanical deformation. Three parameters are used to define the piezoelectric properties of a material:

- piezoelectric charge constant, d_{ij}, relates the mechanical strain to the applied electrical field.
- piezoelectric charge constant, e_{ij}, relates the stress to the applied electrical field.
- piezoelectric voltage constant g_{ij}, relates the electrical field to the applied mechanical stress.

d_{ij} and e_{ij} are influential in this work as they strongly indicate the piezoelectric performance of the ceramic material for high power ultrasonic applications, while g_{ij} is more important in assessing the materials suitability for sensing. Piezoelectric charge constants d and e, are defined within Abaqus in matrix form:

$$[d] = \begin{bmatrix} d_{111} & d_{122} & d_{133} & d_{112} & d_{113} & d_{123} \\ d_{211} & d_{222} & d_{233} & d_{212} & d_{213} & d_{223} \\ d_{311} & d_{322} & d_{333} & d_{312} & d_{313} & d_{323} \end{bmatrix} \tag{3.4}$$

$$[e] = \begin{bmatrix} e_{111} & e_{122} & e_{133} & e_{112} & e_{113} & e_{123} \\ e_{211} & e_{222} & e_{233} & e_{212} & e_{213} & e_{223} \\ e_{311} & e_{322} & e_{333} & e_{312} & e_{313} & e_{323} \end{bmatrix} \tag{3.5}$$

The first index refers to the component of electric flux, while the second and third refers to the component of mechanical stress or strain. The stress e can be found from the strain d using the following expression:

$$[e] = [d][D] \tag{3.6}$$

For a piezoelectric material poled in the z direction (thickness direction) the matrices can be simplified to:

$$[d] = \begin{bmatrix} 0 & 0 & 0 & 0 & 0 & d_{123} \\ 0 & 0 & 0 & 0 & d_{213} & 0 \\ d_{311} & d_{322} & d_{333} & 0 & 0 & 0 \end{bmatrix} \tag{3.7}$$

$$[e] = \begin{bmatrix} 0 & 0 & 0 & 0 & 0 & e_{123} \\ 0 & 0 & 0 & 0 & e_{213} & 0 \\ e_{311} & e_{322} & e_{333} & 0 & 0 & 0 \end{bmatrix} \tag{3.8}$$

Manufacturers of piezoceramic materials provide piezoelectric charge constant in the strain form d_{33} , d_{31} and d_{15}. Equation 3.7 is used to convert from d_{ij} to d_{ijk}, using these relationships:

$$d_{123} = d_{15} = d_{213}, d_{311} = d_{31} = d_{322}, d_{333} = d_{311} = d_{33} \tag{3.9}$$

Permittivity

The piezoelectric permittivity (or dielectric constant) describes the dielectric displacement per unit electric field. Permittivity of a piezoceramic material can be assessed at either constant stress e_{ij}^T or constant strain e_{ij}^S. The first subscript represents the direction of the dielectric displacement while the second indicates the electric field. These constants are commonly provided in a relative dielectric constant which is the ratio of dielectric constant to absolute dielectric constant e_o, where $e_o = 8.85\text{x}10^{-12}$ farad/metre.

In Abaqus the dielectric properties of the piezoelectric materials are defined in matrix

form:

$$[\epsilon^s] = \begin{bmatrix} \epsilon^s_{11} & 0 & 0 \\ 0 & \epsilon^s_{22} & 0 \\ 0 & 0 & \epsilon^s_{33} \end{bmatrix} \tag{3.10}$$

For a piezoelectric material poled in the thickness direction, suppliers normally provide ϵ^s_{11} and ϵ^s_{33}, assuming that $\epsilon^s_{22} = \epsilon^s_{11}$. For the piezoceramics utilised in this study the relative dielectric constants are supplied, allowing easy calculation of the dielectric constants.

Summary of PZT properties

The elastic, piezoelectric and dielectric material properties of PZT8, from the data supplied by the manufacturers are listed in Table 3.6. Values not shown in the table are equal to zero.

Elastic properties of PZT8 (N/m^2)

D_{1111}	D_{1122}	D_{1133}	D_{2222}	D_{2233}
9.54x10^{10}	$-$7.73x10^{9}	2.58x10^{10}	9.54x10^{10}	2.58x10^{10}

D_{3333}	D_{1212}	D_{1313}	D_{2323}
8.59x10^{10}	4.39x10^{10}	4.39x10^{10}	4.39x10^{10}

Piezoelectric properties of PZT8 (C/N)

d_{123}	d_{213}	d_{311}	d_{322}	d_{333}
3.8x10^{-10}	3.8x10^{-10}	-9.50x10^{-11}	-9.50x10^{-11}	2.4x10^{-10}

Permittivity of PZT8 (F/m)

ϵ^S_{11}	ϵ^S_{22}	ϵ^S_{33}
1.11x10^{-8}	1.1x10^{-8}	8.85x10^{-9}

Table 3.6: PZT8 material properties calculated for FEA

3.3.2 Defining boundary conditions

Boundary conditions (BCs) specify the values of variables and define constraints at nodes at a material interface or structural boundary. For the ultrasonic transducer model the electrical potential of piezoelectric elements is prescribed using a boundary condition. In the eigenfrequency extraction step the electrical potential degree of freedom of piezoceramic element must be constrained to at least one node to remove singularities from the dielectric part of the element operator [180].

3.3.3 Interaction between parts

The interaction module of Abaqus is used to define the mechanical contact between parts of an assembly, using either the general contact algorithm or contact pairs. General contact defines the contact between many or all regions of a model. Contact pairs are then defined for all surface to surface pairs which require a special contact condition.

For this model the general contact is defined as a penalty enforcement used to prevent the penetration of one surface into another. Two types of contact pairs are then defined. The first is frictionless sliding between the bolt and the inside of the back mass and the second is tie contacts between the bolt and the front mass and the front mass and the needle insert.

3.3.4 Analysis steps

The step module of Abaqus allows the sequence of one or more analysis steps and the output request for each to be defined. The initial step allows boundary conditions, predefined fields and interactions applicable at the beginning of the analysis to be defined. This is followed by one or more steps defined by the type of analysis. These are classed as a general step where the response is non-linear or a linear perturbation step where the response is linear. To determine the resonant frequencies a linear perturbation procedure, a frequency extraction, is configured where an eigenvalue extraction procedure calculates the natural frequencies and corresponding mode shapes.

3.3.5 Discretisation of the domain

FEA discretises a structure with finite elements interconnected through nodes. The number of elements, the density of the mesh, the type and shape of the elements, all have a significant

effect on the final solution.

Abaqus offers three types of elements relevant to the transducer model; hexahedral (C3D20R), tetrahedral (C3D15) and wedge (C3D15). For each element type the first order elements use a linear interpolation and second order elements use a quadratic interpolation to approximate the solution. For modal analysis, the second order hexahedral element C3D20R is recommended. For piezoceramic material, C3D20RE has the same characteristic as C3D20 while also allowing for electrical potential. A tetrahedral element, C3D15 is used where geometrical complexities in the model such as helical cuts to the needle and front mass prevent the use of hexahedral elements.

3.4 Design of the longitudinal mode devices

Two longitudinally vibrating ultrasonic transducers scaled with a tip geometry to match a 9-gauge and 11-gauge trephine needles are used. The geometry of each transducer is tuned to meet the design criteria discussed in Section 3.2. The final design of the transducers, for the two devices referred to in this thesis as USN1 and USN2 are shown in Figure 3.5.

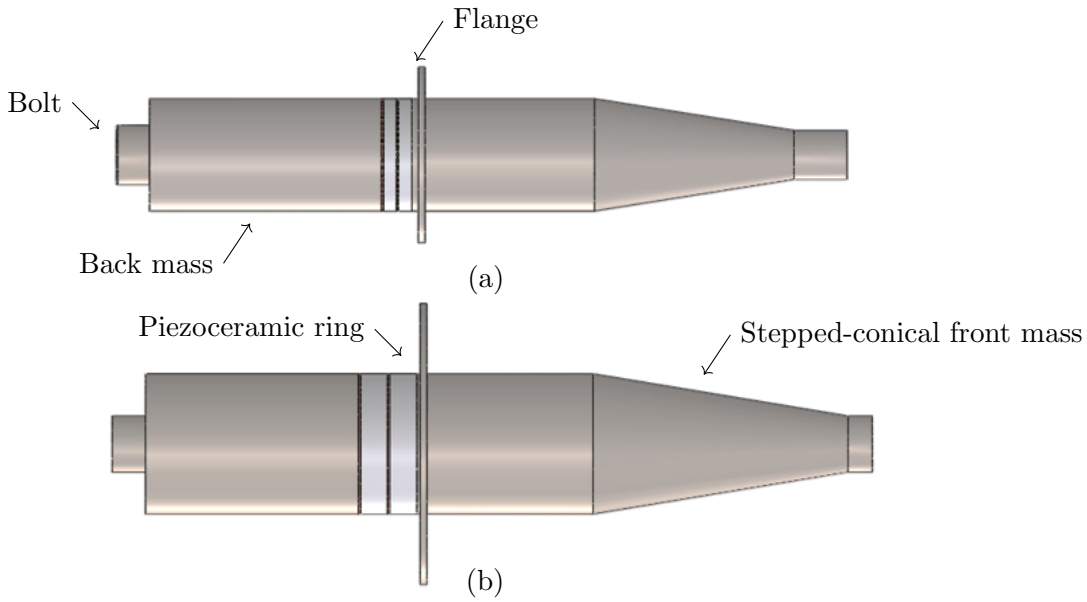

Figure 3.5: Configuration of longitudinally vibrating ultrasonic transducer (a) USN1 and (b) USN2

Each transducer comprises of piezoceramic discs, copper electrodes, titanium front and back masses and a steel prestress bolt. The diameter of the back masses matches that of the

piezoceramic discs of USN1 and USN2, 16 mm and 20 mm respectively, while the length of the back masses are 35 mm and 32 mm. The profile of the front mass consists of a flange and a cylindrical-conical horn. The cylindrical section of front mass, of constant radius, possesses a diameter matching that of the back masses, with lengths of 25.5 mm and 25 mm for USN1 and USN2 respectively. The conical section provides ultrasonic amplitude amplification while also reducing the radius of the device along a length of 30 mm and 38.5 mm respectively, the resulting diameters at the output face being 7 mm and 8 mm respectively. The USN1 and USN2 transducer are tuned at 27.6 kHz and 26 kHz respectively.

3.4.1 Mesh convergence

A mesh convergence study is conducted to ensure the density of the mesh produces an accurate solution. Mesh convergence seeks the mesh where the modal frequencies stabilize within the frequency range of interest. The mesh density in Abaqus CAE is altered by defining the seed size. Seeds are markers placed along the edges of the structure stipulating the target mesh density. Mesh convergence is conducted for the full wavelength USN1 device, of the transducer connected to a conical needle insert made from 316L stainless steel. Stainless steel is used in the initial prototype due to the availability of surgical grade tubing. Figure 3.6 shows the number of elements required to achieve mesh convergence, with the analysis covering the third and fourth torsional modes (T3 and T4), the 8th and 9th bending modes (B8 and B9), a bolt mode (Bolt) and the second longitudinal mode (L2). The results indicate that a finer mesh density is required for convergence of the higher order modes. Convergence is achieved for all modes within the frequency range when the system using 700 discrete elements, defined by a global seed size of 0.06 mm.

3.4.2 Resonant needle

Slender multiple half-wavelength power ultrasonic devices often exhibit modal coupling arising when the frequencies of different modes are close to each other. Modal frequency separation can reduce the likelihood of coupling and is achieved in this study by adjusting the needle insert geometry. The geometry and profile shape are systematically altered to identify the design that best isolates the tuned frequency from the neighbouring modes.

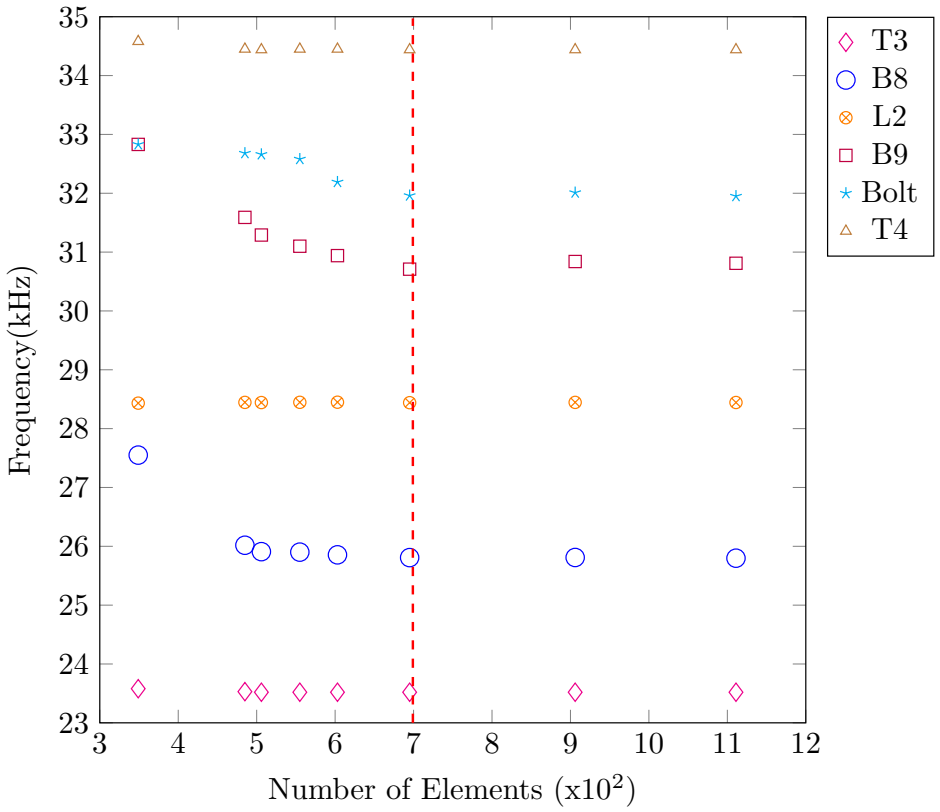

Figure 3.6: Elements required to obtain mesh convergence

Needle length

The first feature of the geometry to be studied is the needle length, L_{need}. A conical profile is adopted for the needle to reduce the outer diameter from 7 mm to 3 mm as shown in Figure 3.7. For each value of L_{need} an eigenmode extraction is executed to calculate the mode shapes and modal frequencies. All modes between 0 and 50 kHz are calculated.

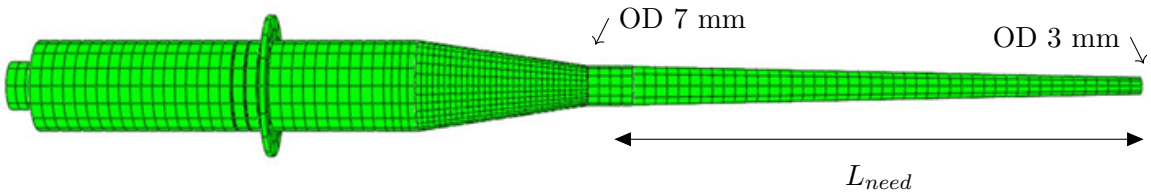

Figure 3.7: FE model adopted to study the needle insert length

Some insight into the relationship between modal frequencies and the length of the needle can be gained by looking at the analytical equations for a simple cylindrical rod. The resonant frequencies for the longitudinal and torsional modes are calculated using Equations 3.11 and 3.12 respectively.

$$f_L = \frac{n}{2L_r}\sqrt{\frac{E}{\rho}} \tag{3.11}$$

$$f_T = \frac{n}{2L_r}\sqrt{\frac{E}{2\rho(1+v)'}} \tag{3.12}$$

where n is the mode number, L_r is the length of the rod, E if the Young's modulus of the rod, ρ is the density of the rod and v is the Poisson's ratio. As the length L_{need} increases, the modal frequency decreases. As seen in Figure 3.8, the frequency-length relationship is linear for L1 and L2 modes. Torsional mode frequencies are similarly related to length and are similarly exhibiting a linear relationship in Figure 3.8 for low order modes.

For bending modes (B) the frequency is given as:

$$f_B = S_n \frac{\pi K}{8L^2}\sqrt{\frac{E}{\rho}} \tag{3.13}$$

where K is the radius of gyration and the S_n term is given as,

$$S_n = \begin{cases} 3.011, & \text{n} = 1 \\ (2n+1), & \text{n} > 1 \end{cases} \tag{3.14}$$

Equation 3.13 suggests that f_B depends inversely on the square of the length. However, Figure 3.8 exhibits linearity across the modes for the frequency - length relationship, except for the length where there is a frequency cross-over of two modes and for high order modes. The distinguishing influence here, for a conical needle, is the placement of the nodal planes in the thicker and thinner sections.

The length of needle L_{need} of 90 mm provided the largest frequency spacing around L2, which has a predicted frequency of 28.5 kHz. The two closest modes to the tuned mode of vibration are the second bolt bending mode (Bo2) and the eighth bending mode (B8), which provides a frequency spacing of 8% and 10.6% respectively. This length will be maintained as different needle profiles are investigated. Incorporation of the different needle profile should aim to meet the criterion set in Section 3.1 of a 10% frequency spacing.

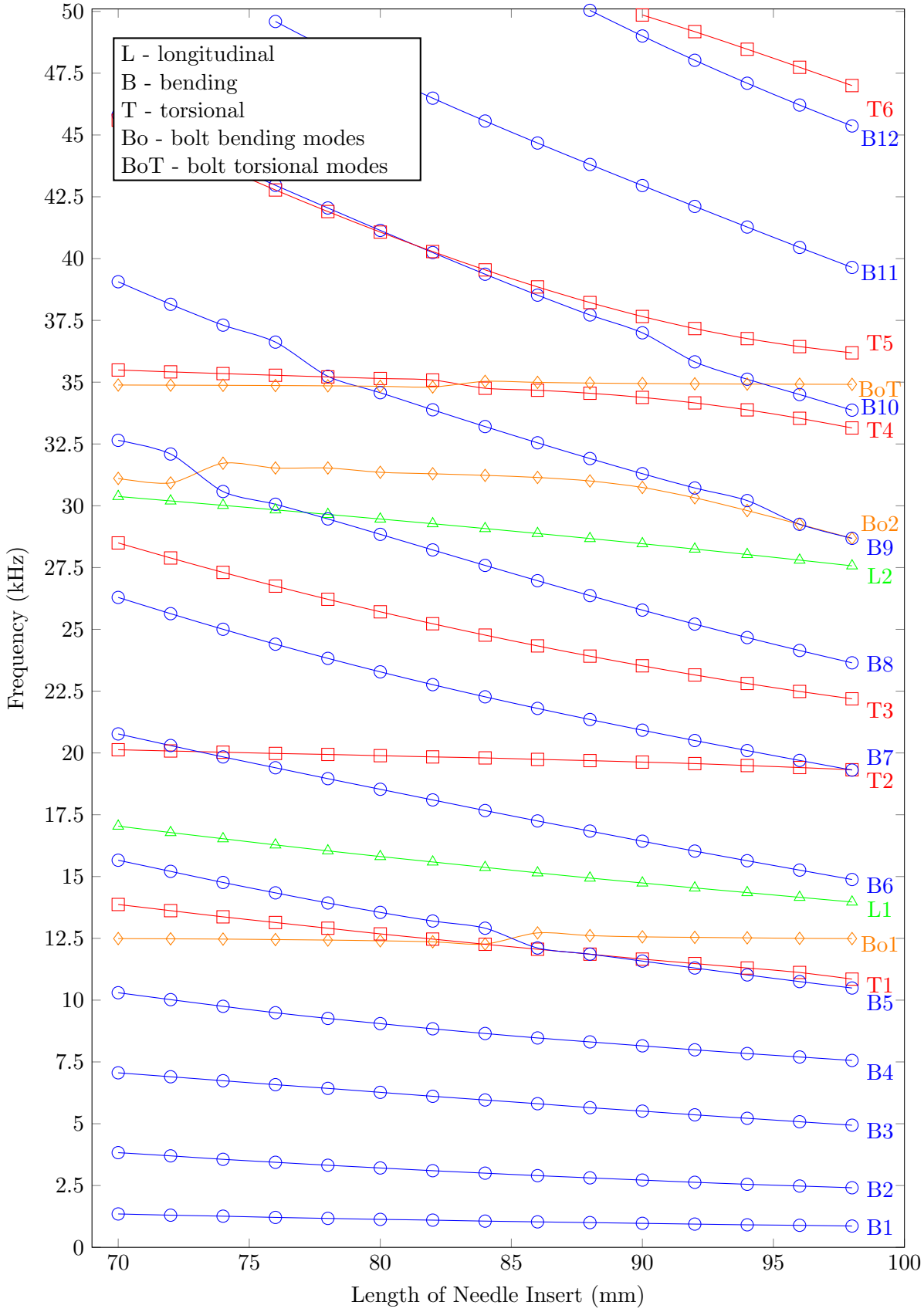

Figure 3.8: Modes of vibration for varying needle length, L_{need}

Needle profile

To form a cylindrical needle tip with a gauge suitable for insertion into bone tissue, two profiles are investigated. A cone to cylinder and cylinder stepping down to a cylinder of reduced radius, both in Figure 3.9. Both profiles decrease the outer diameter from 7 mm to 3 mm equivalent to a gauge 11 bone biopsy needle.

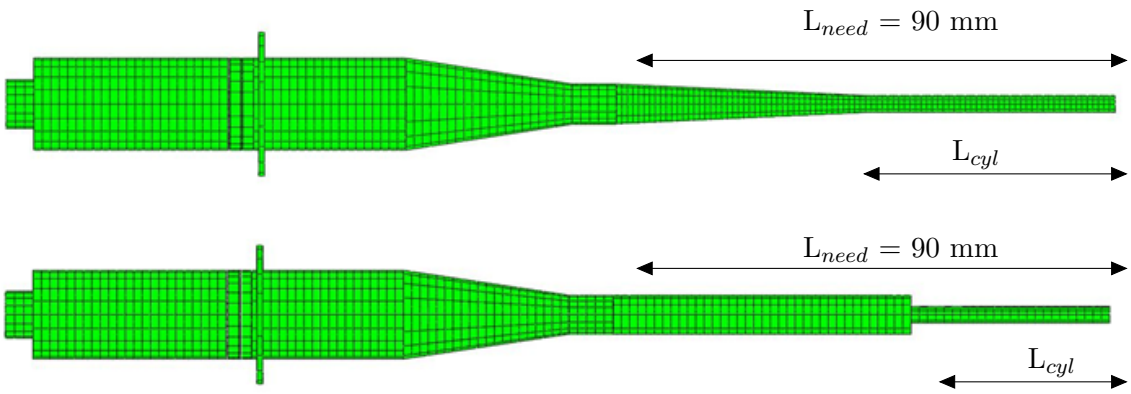

Figure 3.9: Needle profiles (a) conical and (b) stepped

For both profiles the length of the cylinder section, L_{cyl} is adjusted to investigate the frequency separation between the second longitudinal and its neighbouring modes. The results for each profile, showing the frequency of the operating mode L2 and surrounding modes which occur between 0 and 50 kHz are shown in Figure 3.10. Altering the needle profile causes changes in the stiffness and mass distribution along the axial length of the needle insert.

For the conical-cylindrical profile the bending mode frequencies all decrease as the length of the cylindrical section increase, a direct effect of a decrease in stiffness. The behaviour of the lower order longitudinal and torsional modes seem to be affected by the nodal planes. For the stepped-cylindrical profile every mode within the frequency range suggests the nodal plane directly affects the mode frequency. Clarification of this behaviour is sought by mapping how the nodal plane of each mode is affected by the location of the join of the two parts of the profile.

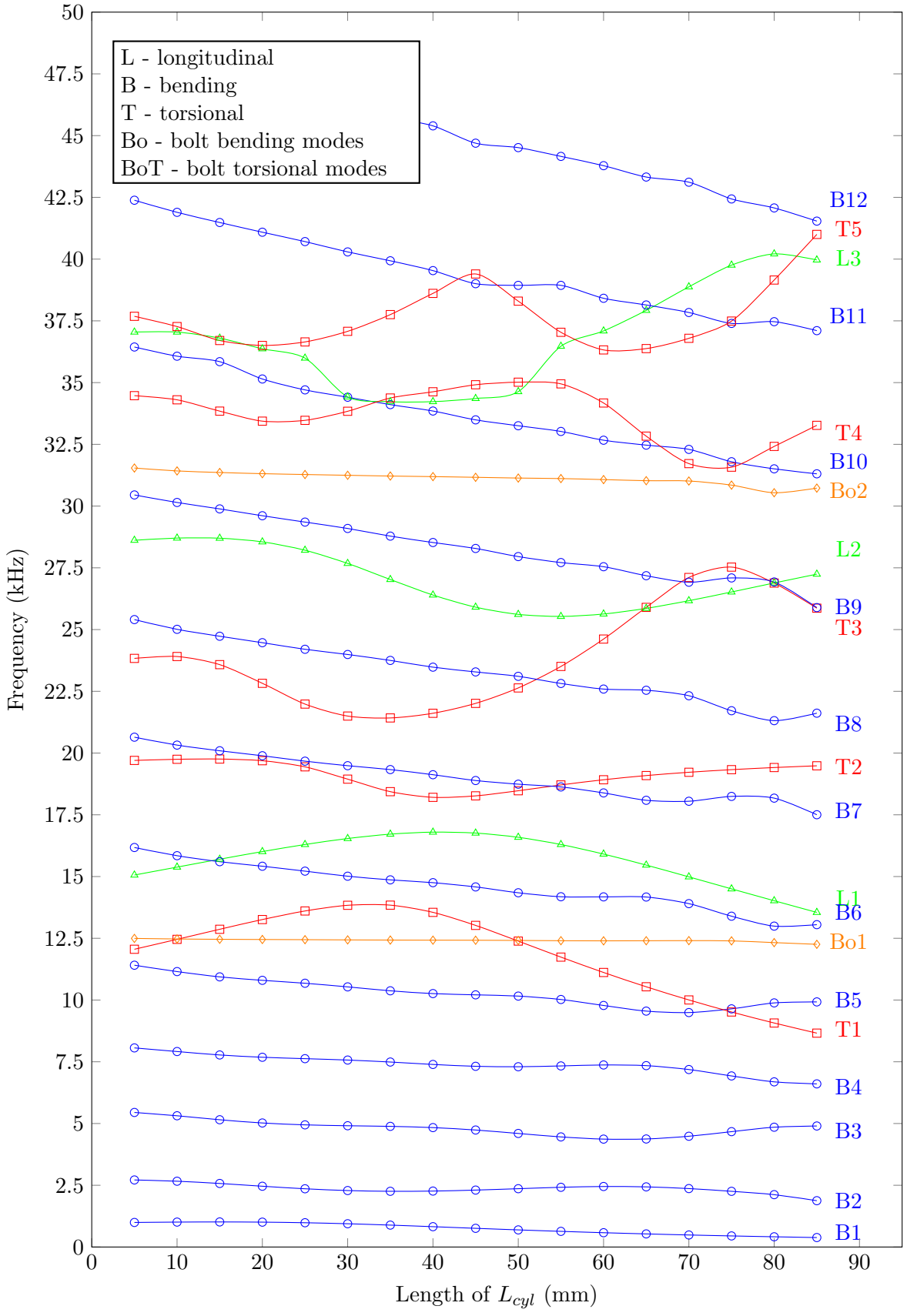
L - longitudinal
B - bending
T - torsional
Bo - bolt bending modes
BoT - bolt torsional modes
Frequency (kHz)
Length of L_{cyl} (mm)
B12
T5
L3
B11
T4
B10
Bo2
L2
B9
T3
B8
T2
B7
L1
B6
Bo1
B5
T1
B4
B3
B2
B1

(a)

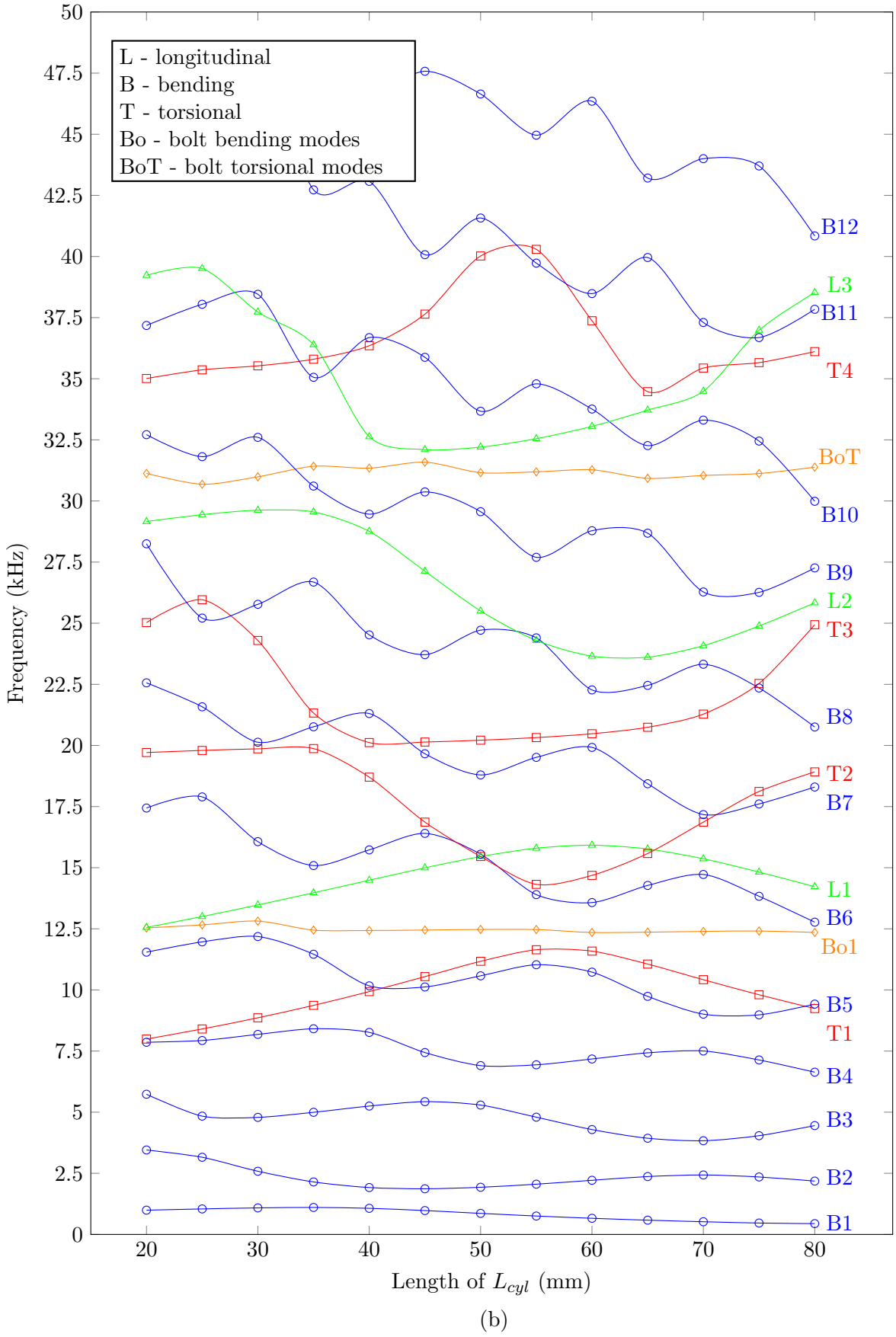

(b)

Figure 3.10: Modal frequency of vibration for varying L_{cyl} for needle with (a) conical-cylindrical profile and (b) cylindrical-step profile

3.4.3 Effect of needle shape on the nodal plane

First considering the cylindrical-stepped needle profile the results in Figure 3.10 indicate that the modal frequencies of the torsional and bending modes increase and decrease in a pattern as L_{cyl} is increased. This can be explained by investigating the axial positions of the nodal planes of these modes in relation to the location of the plane of the step in the profile. For example Figure 3.11 shows the nodal planes of the third torsional mode of vibration T3, n_1, n_2 and n_3 are the positions of the nodal planes extracted from the FEA model. The position of the step is shown as *step*.

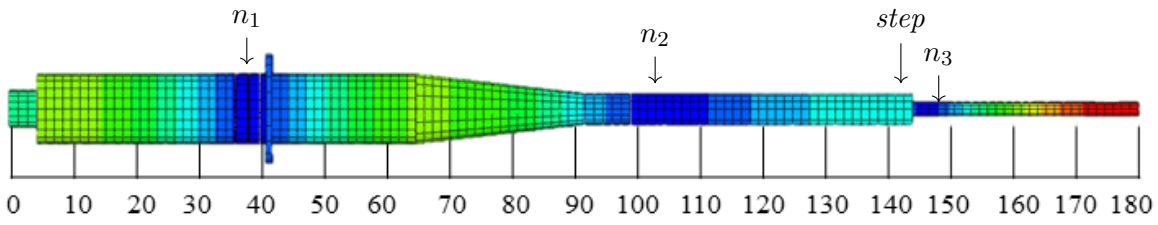

Figure 3.11: Nodal planes of the 3rd torsional mode of the stepped needle profile

How the modal frequencies are affected by the needle profile is investigated by monitoring the separation between the step and the location of the closest node, *step* - n_i, and these are shown in Figure 3.12. From the results small changes to the profile are significant, sweeping 6 kHz, 4 kHz and 6 kHz for L2, B8 and T3 respectively.

For lower order modes L2 and T3, the frequency of the mode decreases as the node and the *step* become aligned at the same location, corresponding to a lowered stiffness. For B8 a higher order mode, the nodal planes clusters towards the needle insert where the diameter is small. This causes changes to the location of the *step* along the needle insert to be highly influential, increasing and decreasing the frequency of the mode.

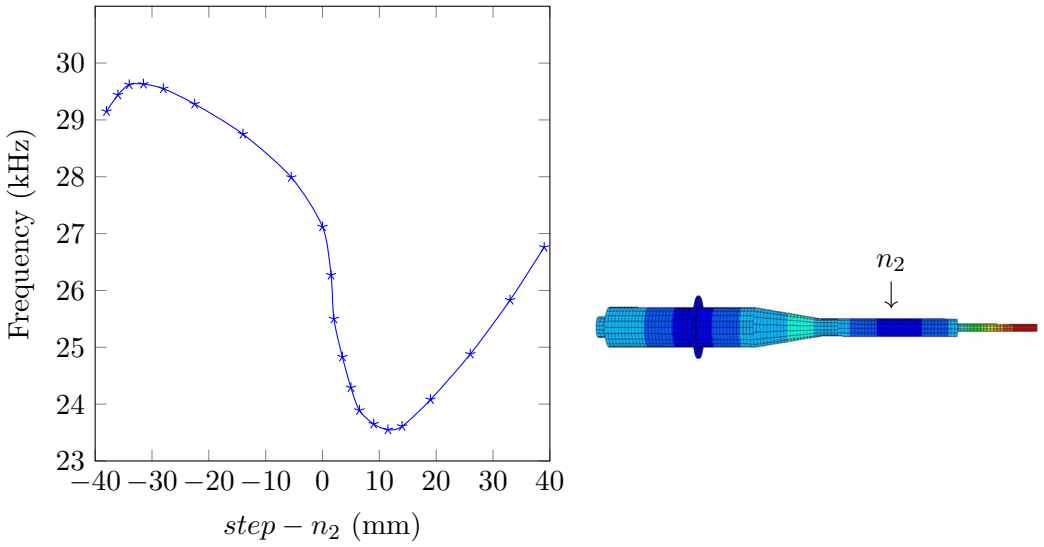

(a) L2

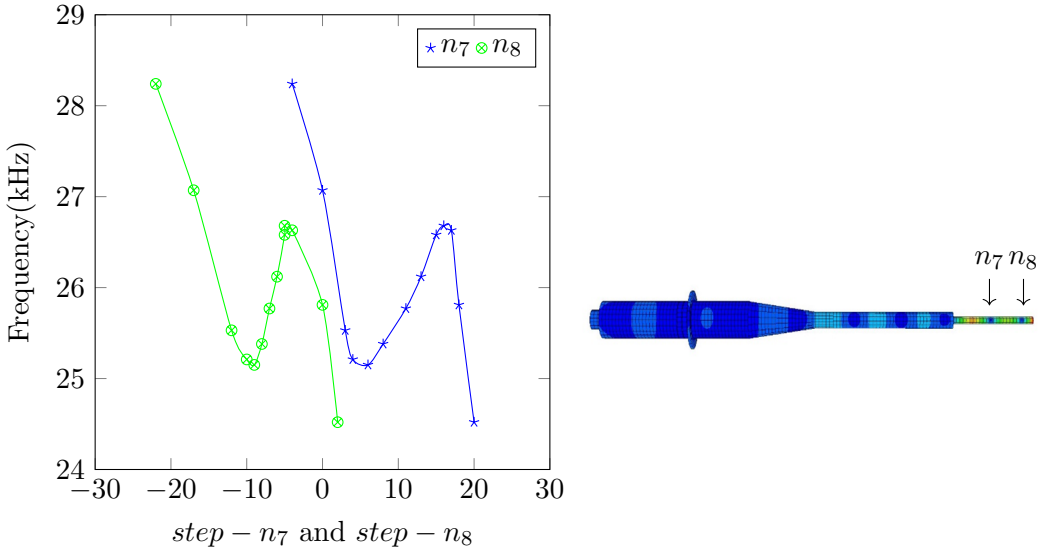

(b) B8

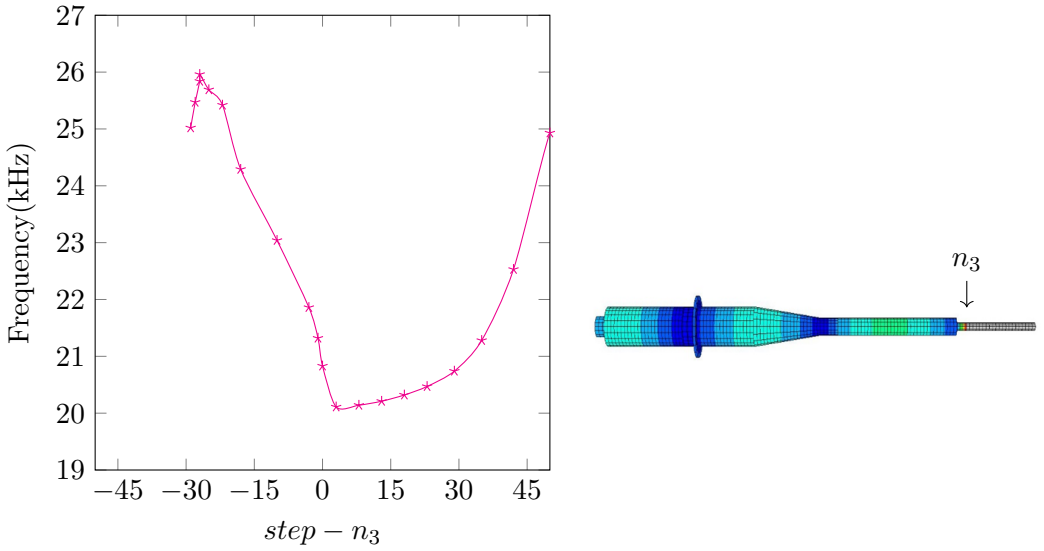

(c) T3

Figure 3.12: Nodal plane investigation of stepped profile

Now considering the case of the conical-cylindrical needle profile. Here, the joining plane of the two cones is shown as Δcon in Figure 3.13, which shows n_1 and n_2 of the L2 mode.

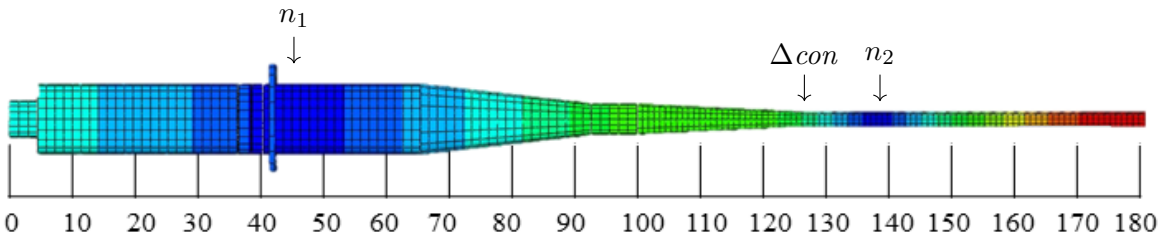

Figure 3.13: Nodal planes of the 2nd longitudinal mode for the conical-cylindrical needle profile

The effect on frequency of the location of a nodal plane close to Δcon is shown in Figure 3.14. For L2 and T3 the frequency decreases as the node plane and Δcon corresponding to lowering of the axial stiffness. Although the slender needle profile causes the nodal plane of B9 to cluster toward the narrow diameter component, the location of the nodes of B9 did not change as the location of Δcon was altered, contrary to the *step* profile. This can be attributed to the stress at the step caused by the immediate decrease in stiffness. Consequently, a conical-cylindrical profile will be used for the prototypes.

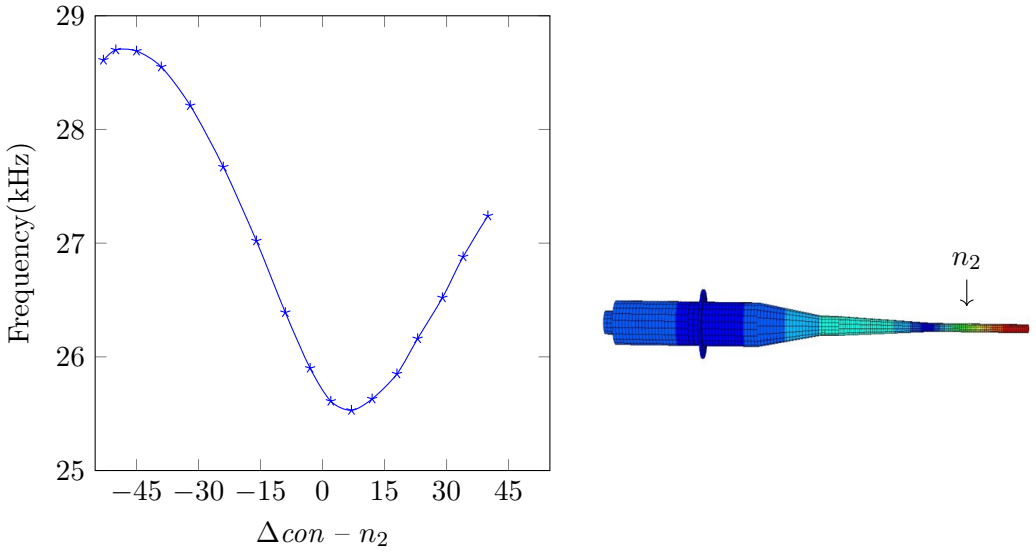

(a) L2

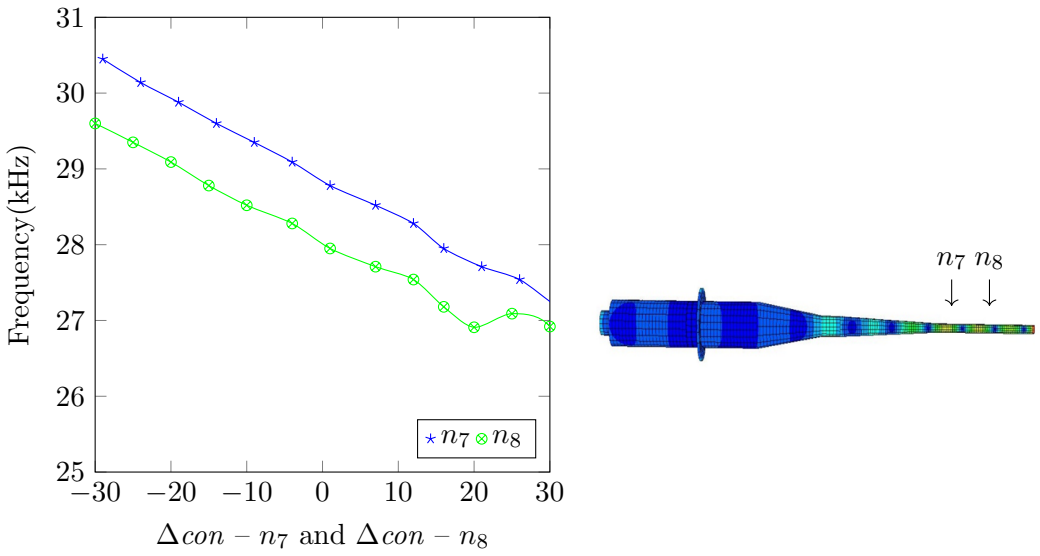

(b) B9

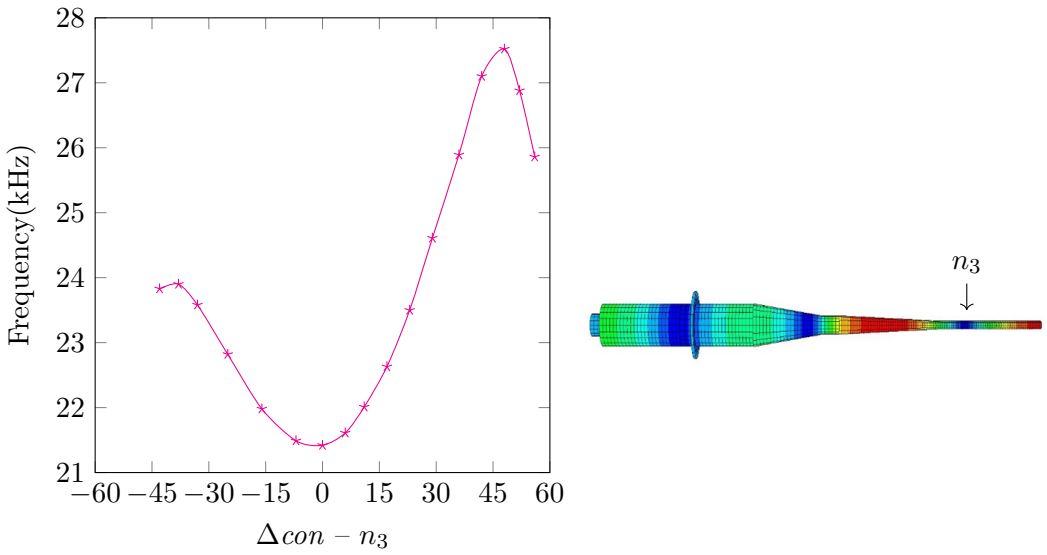

(c) T3

Figure 3.14: Nodal plane investigation of conical profile

3.4.4 Finalised longitudinal devices

Following the findings of the previous sections the designs of USN1 and the larger, USN2 are finalised for manufacture. For USN1, the length of L_{cyl} which resulted in the highest frequency spacing between L2 and the surrounding modal frequencies is 45 mm where the frequency spacing between the L2 and B8 and B9 is 10% and 9% respectively, while for USN2 needle the frequency spacings are largest, 9% and 16% respectively for B8 and B9 for L_{need} = 122 mm and L_{cyl} = 30 mm. The final designs of USN1 and USN2 are illustrated in Figure 3.15.

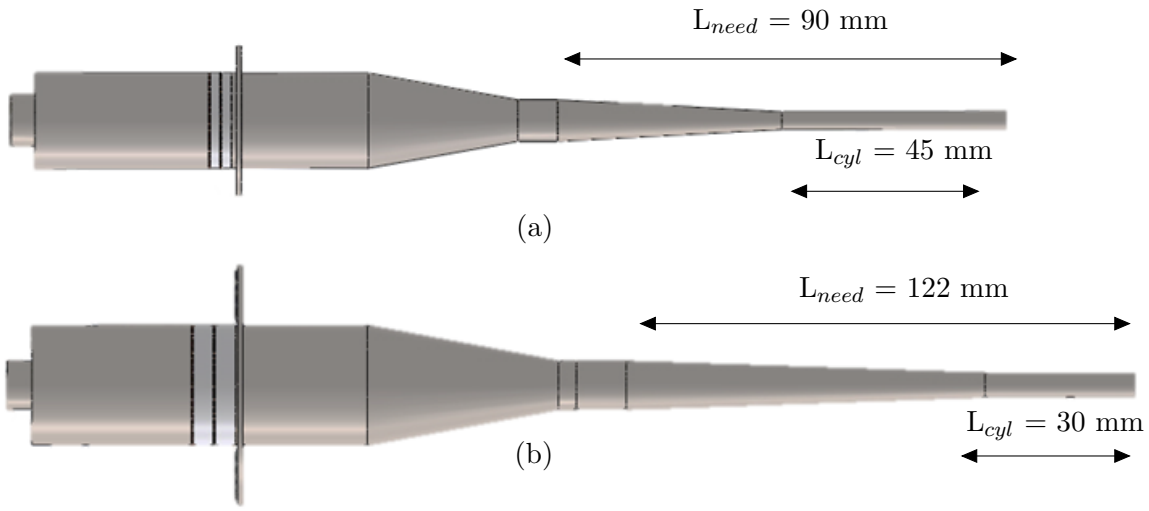

Figure 3.15: Final design of (a) USN1 and (b) USN2

3.5 Design of composite longitudinal-torsional mode needle device

Longitudinal-torsional (L-T) coupled vibrations have proven advantageous in many ultrasonic applications including several ultrasonic surgical devices. In this study, the potential of an L-T motion at the needle tip to improve penetration into bone is investigated.

The generation of the L-T vibration is accomplished by degenerating part of the longitudinal wave into torsional motion through geometrical modifications to the horn and needle insert and follows the work on L-T transducers by Al-Budairi [181]. A transducer was designed consisting of an exponential horn with a quarter circle cut, lofted around the horn section. The optimisation of this geometry focused on the effects of the helical cuts and the twisting angle on the vibrational response of the device.

The L-T biopsy needle device is compared with the L-mode needle device based on their ability to penetrate animal bone samples. The L mode device, USN3, consisted of the same transducer of USN2 but replaced the stainless steel needle insert with a Ti-6Al-4V titanium alloy needle, to reduce losses and PZT8 rings with PZT26 rings of the same geometry due to availability. Following the design procedure of the L-mode devices, a conical needle insert is adopted with the needle length L_{need} of 96 mm and straight section L_{cyl} of 40 mm. The tuned longitudinal mode frequency is 24.6 kHz, with the closest neighbouring modes and the frequencies of the surrounding T3 and B9 estimated as 21.3 kHz and 27.2 kHz respectively, a 11.2% and 10.5% frequency respectively. Helical cuts are introduced lofted along the conical lengths of the front mass and needle. This investigation scrutinised the frequency spacing between the L-T mode and surrounding parasitic modes and calculated the torsional response at the tip of the device based on the design criteria set in Section 3.1.

3.5.1 Front mass helical cuts

A quarter circle cross-sectional slot pattern, as illustrated in Figure 3.16, is extruded with a twist along the length of the conical horn of the front mass, utilising the Abaqus pitch feature. The depth and twist angle are altered to investigate how they affect the frequency of the modes of interest and torsionality at the tip, where torsionality is defined as the tangential displacement at a node on the tip of the needle given as a fraction of the longitudinal displacement.

The pitch, p, is defined as the axial length within which a 360° twist occurs, defined for different twist angles θ by the following expression:

$$p = L_{cut}\frac{360}{\theta} \tag{3.15}$$

Six twist angles, θ, are selected; 60°, 120°, 180°, 240°, 300°, 360°and three depths of cut D_{cut}; 4, 5 and 6 mm as illustrated in Figure 3.16.

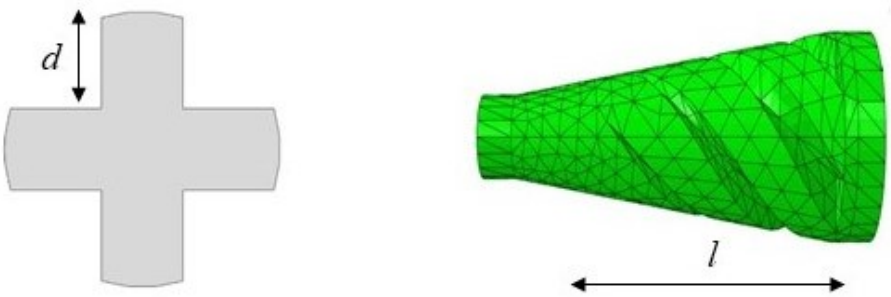

(a) (b)

Figure 3.16: Quarter circle cut (a) cross section (b) on the front mass

Depths of cut, D_{cut}, of 4, 5 and 6 mm result in cut lengths along the front mass, L_{cut}, of 20 mm, 28 mm and 34 mm respectively. The modal frequency dependency on D_{cut} and θ are shown in Figure 3.17. Frequency spacing meets the design criteria for all combinations, but Figure 3.17(d) shows that the highest torsionality is achieved for 6 mm cut depth and a 180°twist angle. However, a better combination of frequency spacing (seen in Figure 3.17(c)) and torsionality is achieved for a twist angle of 240° and therefore that is selected for the USN3 device.

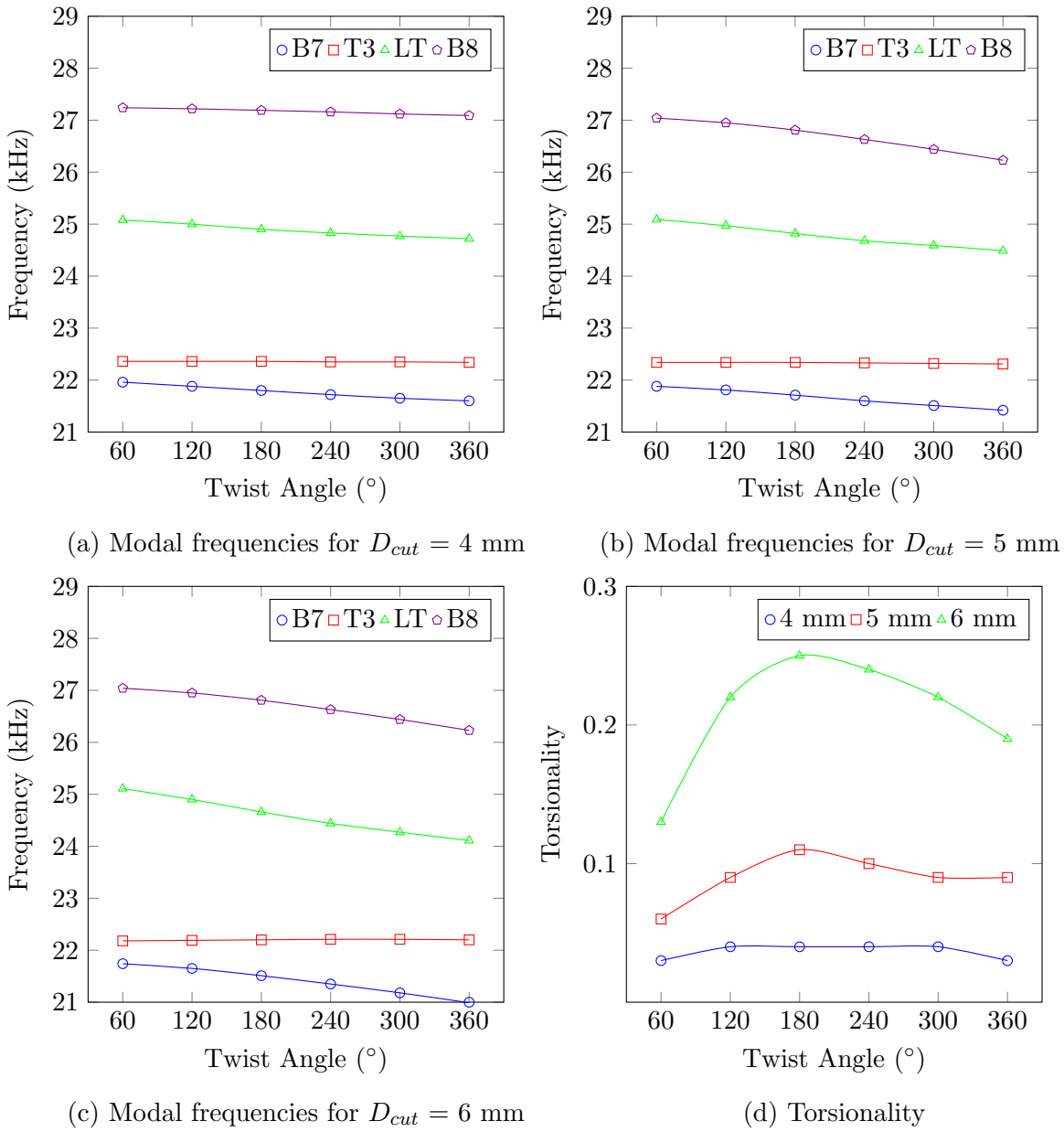

(a) Modal frequencies for D_{cut} = 4 mm

(b) Modal frequencies for D_{cut} = 5 mm

(c) Modal frequencies for D_{cut} = 6 mm

(d) Torsionality

Figure 3.17: (a), (b) and (c) Modal frequency and (d) torsionality dependence on D_{cut} and twist angle for helical cuts on front mass.

3.5.2 Needle helical cuts

With a 6 mm deep 240° helical cut on the front mass, three depths of cut are investigated for the needle geometry of 1 mm, 1.5 mm and 2 mm. The pitch angle follows the front mass cut. These then correspond to 24 mm, 35 mm and 48 mm cut lengths along the length of the conical section of the needle. The results are shown in Figure 3.18. The highest torsionality is achieved for 2 mm depth cut which results in upper and lower frequency spacings are 13.7% and 8.7% respectively for the B8 and T3. This configuration is suitable as the mode with a

frequency spacing less than 10% is T3 and it would be beneficial to couple with this mode to increase torsion at the tip of the needle.

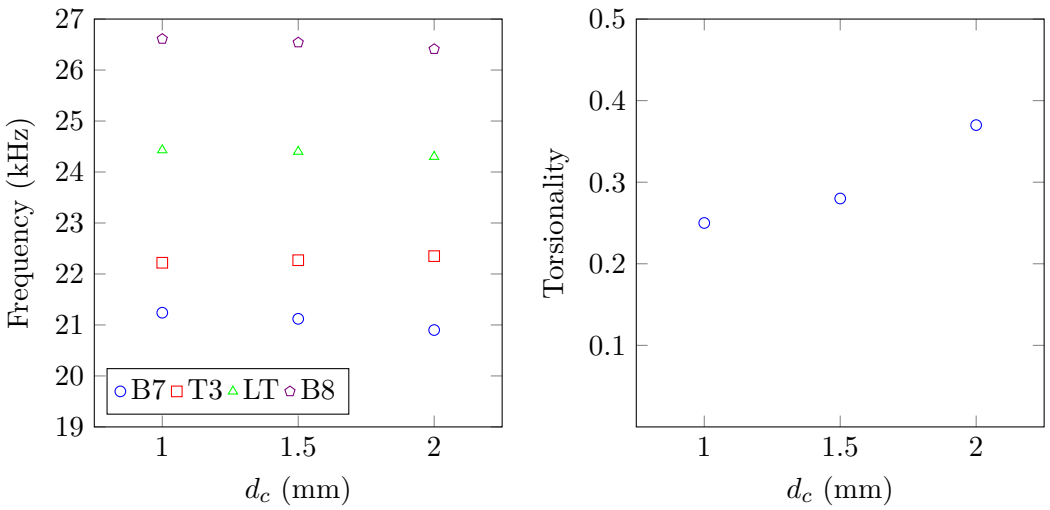

(a) Needle depth cuts (b) Torsionality

Figure 3.18: (a) Modal frequency and (d) torsionality dependence on cut depth for helical cuts on needle.

3.5.3 Finalised longitudinal-torsional device

The configuration of the longitudinal-torsional device, USNLT is defined based on the design criteria set in Section 3.1 for a sufficient frequency spacing and maximum torsionality. A 6 mm cut depth which resulted in a 34 mm long cut along the length of the front mass is matched with a 2 mm cut depth, 48 mm length along the needle insert. As illustrated in Figure 3.19 the final configuration consists of a lofted cut around the front mass and needle turning 12° per mm along the axial length.

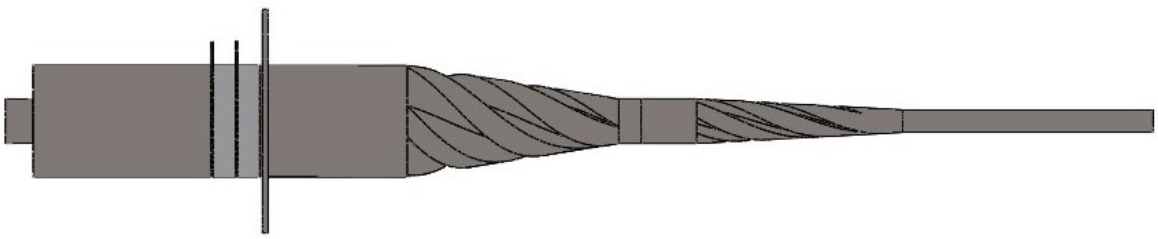

Figure 3.19: Finalise longitudinal-torsional device

3.6 Investigating piezoceramic volume

Section 3.2.2 describes design guidelines for the piezoceramic stack of a Langevin transducer. However, these design rules are often broken during the design phase of ultrasonic surgical devices. Therefore, the influence of piezoceramic volume on the vibration response of USNLT is investigated to increase the vibrational amplitude.

Preceding sections have used a frequency linear perturbation procedure to predict the natural frequencies and corresponding mode shapes. The longitudinal and torsional displacement output values are normalised responses of the displacement distribution across the device. Abaqus steady state response step offers the steady state amplitude and phase response across a frequency range of interest. However, additional settings are required.

3.6.1 Defining material properties

Additional to the general mass and mechanical elastic properties, damping is required to accurately calculate the steady state response. Abaqus provides Rayleigh damping for this purpose which provides actual displacements around the natural frequencies. Rayleigh damping is specified by two damping factors: α_R is the mass proportional damping and β_R is the stiffness proportional damping. α_R introduces damping forces relating to the absolute velocities of the model while β_R relates to damping proportional to the strain rate or elastic material stiffness. β_R is required in this analysis and is approximated as:

$$\beta_R = \frac{1}{\omega_R Q_M} \tag{3.16}$$

where ω_R is the natural resonant frequency of the system which is obtained from the frequency step and Q_M is the mechanical quality factor of the material.

3.6.2 Defining boundary conditions

Within previous models boundary conditions (BCs) were used to constrain the electrical potential degree of freedom of the nodes representing the piezoceramic rings. The response of the steady state dynamic analysis is calculated directly in terms of the physical degree of freedom of the model. These BCs are used to apply an electrical potential across the face of the piezoelectric elements for the steady state dynamics step. It is defined as a 1

V_{pp} sinusoidal waveform at the positive face of the piezoelectric rings and 0 V_{pp} across the negative face.

3.6.3 Defining analysis step

Defining a steady state dynamic step is achieved by specifying the frequency range of interest and the number of frequencies at which results are required. Sampling can also be specified as either linear, logarithmic or biased towards the ends of the frequency range. The displacement components for each node of the system is the requested output.

3.6.4 Ceramic volume: Bar

Initially a simple cylindrical Langevin transducer is used to investigate the effect the number of piezoceramic rings has on the vibrational response. The number of ceramic rings is altered from 2, 4, 6 and 8, with the axial length of the end masses adjusted to realise four devices, tuned to as close to 30 kHz as possible.

The transducer comprises of copper electrodes, titanium end masses, PZT26 piezoceramic rings and a steel preload bolt. The piezoceramic rings match those used in USN3 with outer diameter of 20 mm, inner diameter of 8 mm and width of 4 mm. The inner and outer diameter of the end masses matches the piezoceramics with axial lengths of 29.9, 21.5, 13.5 and 6.4 mm for 2, 4, 6 and 8 rings respectively. The copper electrodes match that used in USN3 with the steel bolt length adjusted for each configuration to ensure a constraint between the bolt and front mass. Figure 3.20 shows the 6-ring half wavelength transducer.

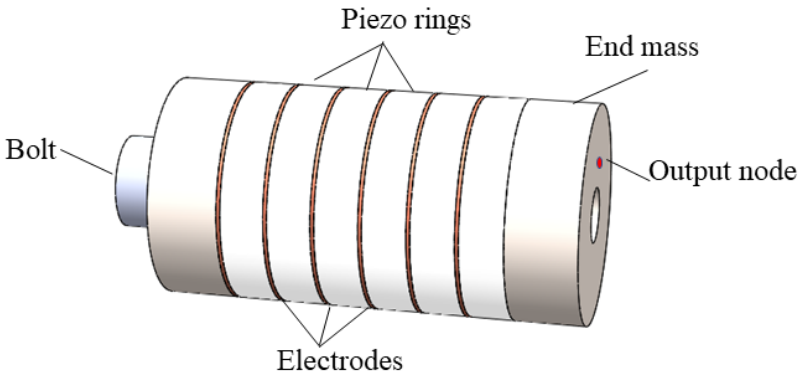

Figure 3.20: Six ring configuration

Steady state response

The steady state response for each 30.1 kHz configurations is calculated for a 1 kHz frequency sweep between 29.5 kHz and 30.5 kHz. The output of the system is extracted as the displacement amplitude response of a unique node on the face of the front end mass (see Figure 3.20). The predicted response when 1 V_{pp} is applied across the transducer stack is shown in Figure 3.21 for each of the four configurations.

The peak displacement amplitude for 2, 4, 6 and 8 rings are predicted as 0.35, 0.65, 0.71, 0.78 μm respectively. Incorporating 4 rings rather than 2 almost doubled the predicted response, however additional rings provided little response. Traditionally a Langevin transducer locates the piezoceramic stack at the node of the longitudinal mode to maximise the piezoceramic element efficiency and reduces the effects of aging. The nodal plane for L1 for each configuration is shown in Figure 3.22. The 6 and 8 ring configurations (Figure 3.22 (c) and (d)) suggest that the portions of the stack located further away from the node have a reduced contribution to the vibrational displacement.

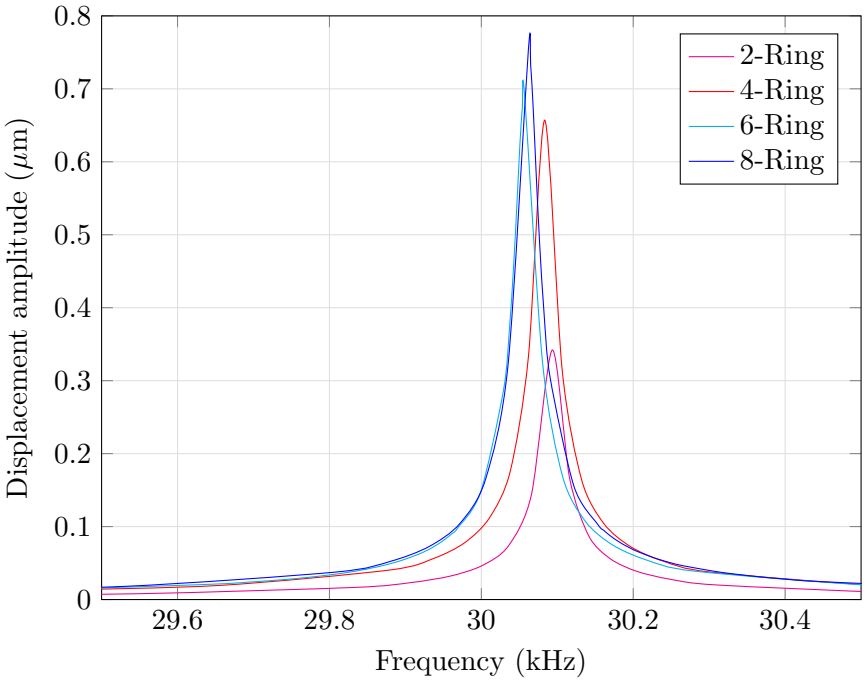

Figure 3.21: Steady state dynamics of different ring quantities

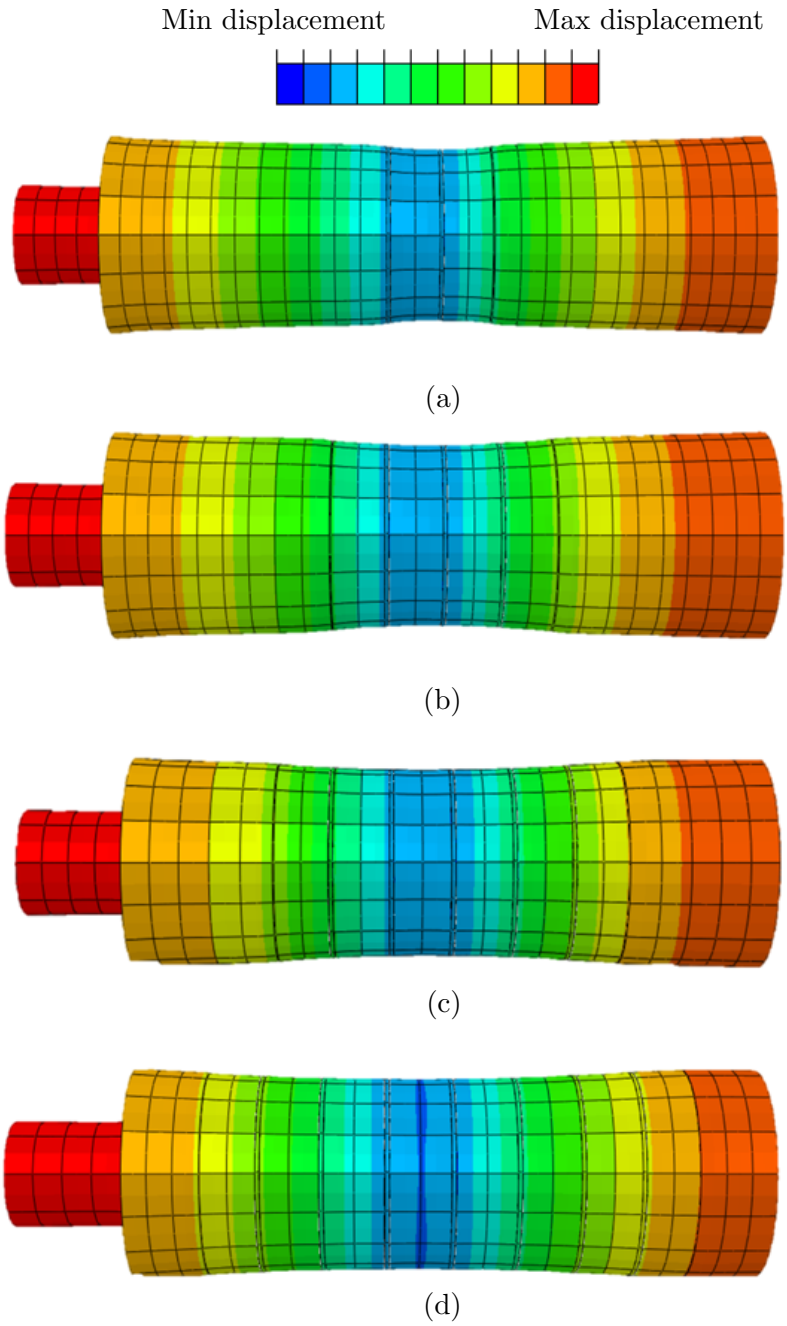

Figure 3.22: Nodal plane of L1 for the (a) 2-ring, (b) 4-ring, (c) 6-ring and (d) 8-ring configuration

3.6.5 Ceramic volume: USNLT

Next, ceramic volume is investigated by altering the ceramic volume of USNLT. The length of the device remained constant, with a second pair of piezoceramic rings accommodated by reducing the length of the back mass. FEA predicted the L-T mode for the 4-ring configuration at 22.9 kHz a shift of 1.1 kHz from the 2-ring configuration. The surround

modes are predicted as T3 and B8 at 22 kHz and 25.3 kHz respectively, resulting in a final frequency spacing of 3.7% and 10.7%. Although the frequency spacing between LT and T3 is lower than desired by the design criterion of 10% however as it is a torsional mode it is likely to add constructively to the torsional vibration of the L-T mode.

Steady state response

The steady state response is calculated for a 1 kHz sweep between 23.5 and 24.5 kHz for the 2-ring configuration and 22.5 and 23.5 kHz for the 4-ring configuration. The voltage across both stacks is 1 V_{pp} and the output is extracted from a node at the tip of the needle insert. Figure 3.23 (a) and (b) shows L and T response for the 2-ring and 4-ring configurations of USNLT respectively.

The maximum longitudinal displacement is 1.37μm and 3.28μm for 2 and 4-ring respectively while the tangential response peaked at 0.35μm and 0.77μm. This predicts that doubling the volume of rings, increasing from a single pair to two pairs of piezoelectric rings, doubles the vibrational displacement at the tip. However, the percentage of tangential displacement per micron of longitudinal vibration (i.e. torsionality) is predicted as 0.25 and 0.23, considerably lower than the prediction of 0.39 in Section 3.4.3. Experimental validation of both configurations is discussed in Chapter 6.

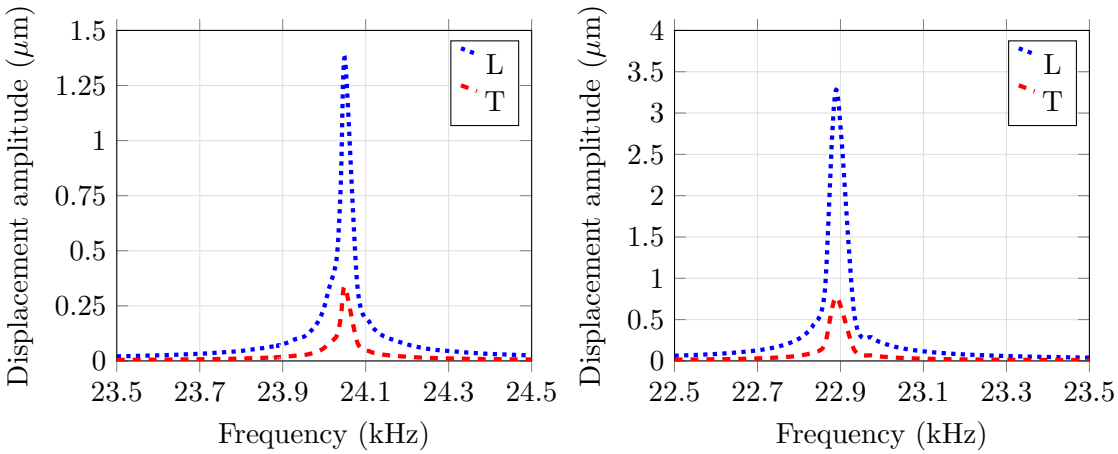

Figure 3.23: Steady state dynamics of (a) 2-Ring vs (b) 4-Ring

3.7 Chapter conclusion

The design of full-wavelength ultrasonic bone biopsy needles has been investigated in this chapter. The design criterion established based on the operating environment and required vibrational response.

Initially the design of each component is discussed based on low acoustic losses and the effective transmission of acoustic energy and the resonant frequency. FEA software Abaqus is used to study the effect of the needle length and profile on the resonant frequencies and mode shapes. Modal frequencies are influenced by small changes to the needle profile. A step, in particular affects the nodal planes which are clustered along the length of the slender needle insert due to the instantaneous decrease in stiffness. The knowledge is used to carefully design the needle profile to meet the design criteria of 10% frequency spacing around the tuned resonant frequency.

Helical cuts are introduced along the length of the conical sections of USN3, the third ultrasonic prototype, to realise a composite L-T motion at the tip of the needle. The design of USNLT is finalised based on the frequency spacing and torsionality at the tip of the device. Table 3.7 provides a summary of the key feature of the four prototypes developed during this research.

Finally, steady state dynamic modelling within the FEA calculates the steady state response of transducers of varying piezoceramic volume, the results suggest that piezoceramic rings located away from the node have a reduced contribution to the vibrational response. In a similar manner the longitudinal and torsional vibrational response, of 2-ring and 4-ring configurations of USNLT, is predicted.

		Prototypes			
		USN1	USN2	USN3	USNLT
Piezo	Material	PZT8	PZT8	PZ26	PZ26
	Outer diameter (mm)	16	20	20	20
	Inner diameter (mm)	7.2	8.2	8.2	8.2
	Length (mm)	2	4	4	4
Backmass	Material	Ti64	Ti64	Ti64	Ti64
	Outer diameter (mm)	16	20	20	20
	Inner diameter (mm)	5	5	6	6
	Length (mm)	35	32	32	32
Frontmass	Material	Ti64	Ti64	Ti64	Ti64
	Profile	cylindrical-conical horn			
	Radius back face (mm)	16	20	20	20
	Cylindrical length (mm)	25.5	25	25	25
	Conical length (mm)	30	38.5	38.5	38.5
	Radius output face (mm)	7	8	8	8
Needle insert	Material	SS316	Ti64	Ti64	Ti64
	Back face diameter (mm)	7	8	8	8
	Tip outer diameter (mm)	3	4	4	4
	Tip inner diameter (mm)	1.8	2.9	2.9	2.9
	Profile	conical-cylindrical horn			
	Needle length (mm)	90	122	92	92
	Cylinder length (mm)	45	30	45	45
Bolt	Material	Steel	Steel	Steel	Steel
	Thread size (mm)	5	5	6	6
	Thread length (mm)	60	60	60	60

Table 3.7: Summary of prototype devices

Chapter 4

Experimental characterisation of prototypes

Prototype ultrasonic needles are characterised through experiments to validate the FEA models before carrying out penetration tests. Predictions made during device design can be limiting because complex geometries, joints and damping are difficult to model accurately. It is therefore vital to validate and improve the model through experiments. The experimental validation procedure for characterising the vibration behaviour of the ultrasonic needle devices is achieved through electrical impedance analysis and experimental modal analysis (EMA).

One use of electrical impedance analysis is to monitor the effect of the pre-stress applied by the bolt of the device. Electrical impedance analysis is also used to match the device with the driving system. The electrical impedance spectrum allows extraction of the resonant frequencies, the electrical impedance and the electromechanical coupling coefficient of the device. EMA is used to obtain the modal parameters of the device, particularly the resonant frequencies and the corresponding mode shapes. The EMA data is used to validate the results predicted by the FEA models and is used to adjust consequent models. This chapter focuses on the complete prototype fabrication and analysis of an L2 mode device named USN3, which is the 3rd prototype designed.

High power ultrasonic surgical devices possess a high Q factor presenting a narrow bandwidth of operation in resonance. However, changes in temperature or load generally cause the resonant frequency to shift slightly, meaning the vibration amplitude decreases and the device is not being driven at resonance. It is therefore proposed that an adaptive

resonance tracking and vibration stabilisation system is adopted and developed. A tracking system is therefore developed based on that reported by Kuang [182] and adapted in this study to enable wider control of driving signals.

4.1 Assembly of the device

The components of the ultrasonic transducer for USN3, are shown in Figure 4.1. The device consists of a bolt, back mass, electrodes, piezoceramic rings, front mass and needle insert. Strong electrical and mechanical contact between components is required to ensure the efficiency of the transducer. Acetone is used to remove dirt or grease from the contact surfaces, particularly on the inner faces. Insulation tape is placed over the bolt section exposed to the inside of the piezoceramic rings to avoid an electrical short circuit.

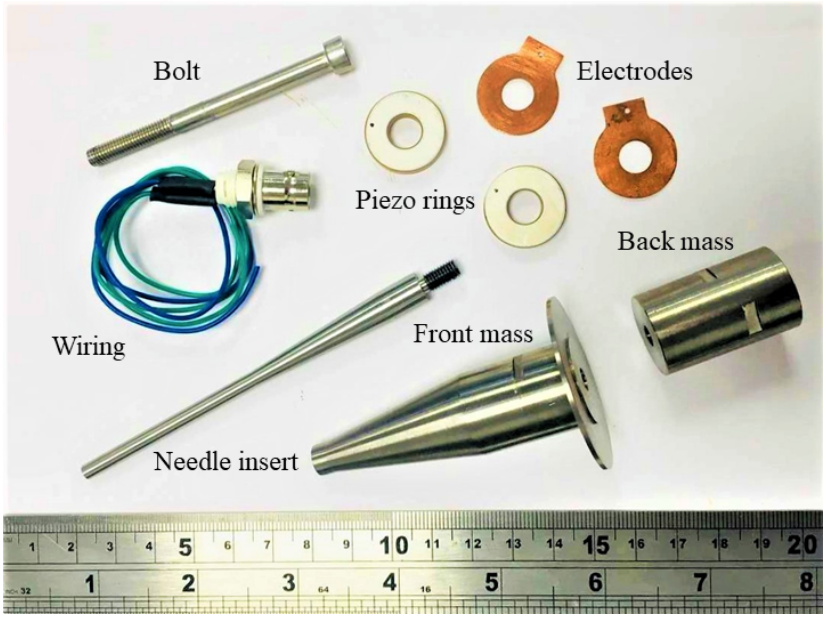

Figure 4.1: Components of USN3

4.1.1 Preload exercise

Preload is a crucial stage in the assembly of a Langevin transducer. As mentioned in Section 3.2.4, the correct prestress delivers no gaps between contacting components, effective electro-mechanical coupling and the lowest attainable impedance. To apply the preload, the transducer is fixed in a vice using fabricated clamps in Figure 4.2. A torque wrench (Norbar,

TT20) is used to apply the preload in five steps as shown in Table 4.1. The impedance spectrum and the generated charge across the piezoceramic stack is used to monitor the transducer performance.

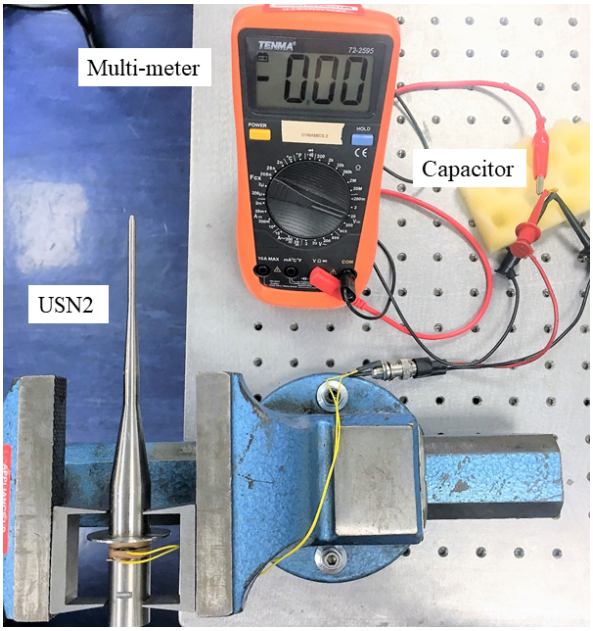

Figure 4.2: Preload setup of USN3

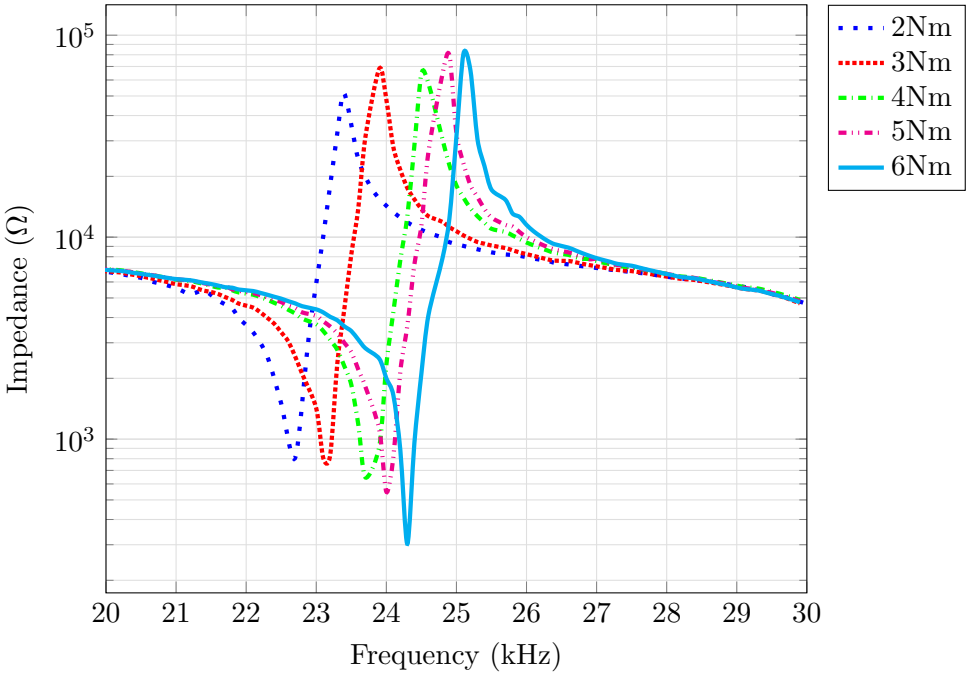

Figure 4.3: Electrical impedance spectrum for USN3 for different applied torques

Step	Applied torque (Nm)	Measured charge x10^{-6}(C)	Prestess (MPa)	Resonant frequency (kHz)	Anti-resonant frequency (kHz)	k_{eff}
1	2	0.86	13.72	22.7	23.4	0.243
2	3	1.1	17.55	23.1	23.9	0.256
3	4	1.35	21.54	23.8	24.6	0.252
4	5	1.59	25.36	24.0	24.8	0.251
5	6	1.77	28.24	24.3	25.2	0.262

Table 4.1: Prestress derivations for USN3

The charge generated during each preload step is obtained by connecting a 1 μF non-electrolytic capacitor across the piezoceramic stack. A digital multi-meter (Tenma, 72-2595) with high internal resistance of 10 MΩ is used to obtain the charge stored within the capacitor achieved by quickly tightening the bolt. The charge is calculated by measuring the voltage and using the following equation:

$$q_e = CV \tag{4.1}$$

where C is the capacitance of the capacitor and V is the voltage across the component. Consequently, the preload on the piezoceramic stack F_{pl} is calculated using:

$$F_{pl} = \frac{q_e}{N_o d_{33}} \tag{4.2}$$

where N_o is the number of piezoceramic rings and d_{33} is the charge constant of the piezoceramic rings in the thickness mode. The stress is then calculated by dividing the force by the cross-sectional area of the piezoceramic ring.

Additionally, an impedance analyser (Agilent, 4294A) is used to measure the impedance across the desired frequency range. From the spectrum, the magnitude of electrical impedance Z_e, series and parallel resonance frequencies f_s and f_p for the desired modes of vibration are monitored. As the electrical signal is small, the series and parallel resonant frequencies, f_s and f_p, can be equated to the resonant and anti-resonant frequencies f_r and f_a. Electrical stability is reached when these frequencies consolidate and become invariant with increased

prestress, and the maximum effective electromechanical coupling coefficient k_{eff} is reached, calculated using Equation 4.3.

$$k_{eff}^2 = 1 - \frac{f_r^2}{f_a^2} \tag{4.3}$$

The impedance spectrum, impedance and stress for each preload step are shown in Figure 4.3 and Table 4.1. The results found that the measured impedance and f_r and f_a is stabilised at Step 5. This corresponds to applying 6 Nm torque equating to 28.24 MPa, which is the prestress required to ensure sufficient compressive stress of the piezoceramic stack.

4.2 Experimental modal analysis

EMA is a process to identify the modal parameters of a structure to extract its vibration characteristics. Originally pioneered by researchers in the aerospace industry EMA is now extensively used to analyse the vibration behaviour of structures.

Vibration of a real structure can be modelled through linear superposition of a system with a single degree of freedom (SDoF), shown in Figure 4.4, to generate system with a multiple degree of freedom (MDoF) system.

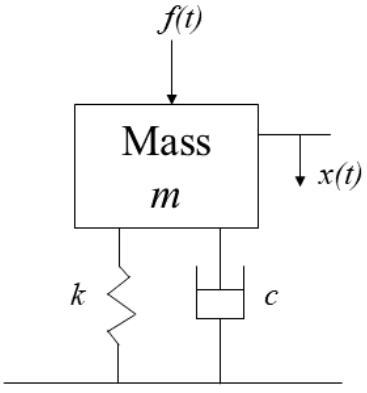

Figure 4.4: System with a single degree of freedom

$$m\ddot{x} + c\dot{x} + kx = f(t) \tag{4.4}$$

where m, k and c represent the mass, spring and damping and *f(t)* and *x(t)* are the time

varying force and displacement.

The frequency response function (FRF) is obtained by dividing the output signal by the input signal of the system in the frequency domain, as shown in Figure 4.5. Hence, Fast Fourier transform (FFT) algorithm is used to transform the data captured in the time domain.

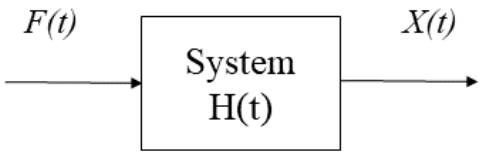

Figure 4.5: Frequency response function

$$f(\omega) \times H(\omega) = x(\omega) \tag{4.5}$$

Typically, the FRF is defined as the ratio between the harmonic displacement response and the harmonic force. Combining this with the SDoF the FRF can be defined in terms of the compliance $\alpha(\omega)$, the ratio between output displacement $x(\omega)$ and applied input harmonic force $f(\omega)$ in the frequency domain. This results in the FRF, $H(\omega)$ becoming:

$$\alpha(\omega) = H(\omega) = \frac{x(\omega)}{f(\omega)} = \frac{1}{(k - \omega^2) + j(\omega c)} \tag{4.6}$$

The FRF can then be calculated dependent on the measurement technique using either the displacement $x(\omega)$, velocity $v(\omega)$ or acceleration $a(\omega)$.

4.2.1 Excitation signal

Vibration measurement can be separated into two methods; free vibration and forced vibration. For an ultrasonic device a forced vibration method is utilised, the excitation being an electrical signal converted into mechanical motion by the piezoceramics. For an FRF to be calculate the input signal must excite all frequencies within the range of interest with the same level of energy. Determining modal parameters is typically achieved by exciting the ultrasonic system with a swept sine or true random signal. In this study, a true random signal is used to capture the response between 0 and 80 kHz. The signal is generated by the

data acquisition system with an amplifier to ensure an acceptable signal to noise ratio.

4.2.2 Measurement

Instruments suitable for performing EMA can be generalised into two groups, contact and non-contact. Contact instruments introduce a mass loading which can induce errors in small structures. Non-contact instruments are non-invasive and do not affect the response of the vibrating structure. Some examples of these instruments include laser Doppler vibrometers, high speed laser interferometers and high-speed cameras.

A laser Doppler vibrometer (Polytec, 3D CLV) is utilised to measure the vibrational response of the ultrasonic needle. Four lines distributed evenly around the device creates the grid, one of which is shown in Figure 4.6. The grid density is selected to ensure all mode shapes predicted within the frequency range of interest are identified. The vibrational response is measured under a free-free boundary condition by supporting the device at the flange, located at the node point.

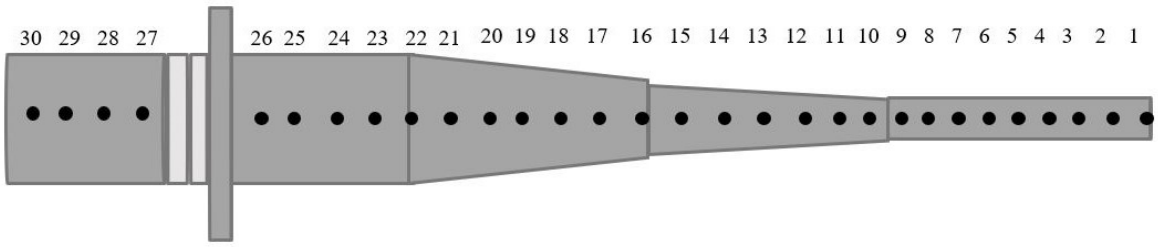

Figure 4.6: EMA grid along length of the Device

4.2.3 Data processing

A spectrum analyser is used to digitise and transform the measured signals from time to frequency domain. The data is collected in analogue form and filtered to remove any high frequency components aliasing within the frequency range of interest. It is then digitised using an analogue to digital converter during which the signals are sampled at a rate to sufficiently capture the frequency range of interest. Windowing is used to reduce distortion caused by processing the non-periodic random wave over a discrete period. The Hanning window, a special time domain window is preferred for random excitations. For this work the number of spectral lines is 51200, resulting in a resolution of 1.56 Hz for the frequency

range of interest, 0 to 80 kHz.

Fast Fourier transform (FFT) transforms the time domain to the frequency domain. The resulting set of frequency response functions (FRFs), three directions for each point across the grid, are then exported to modal analysis software MEScopeVES (Vibrant Technology Inc). Curve fitting allows the extraction of the modal shapes by transforming the FRFs into a single FRF function. The curve fitted trace represents the modal response of the full structure, the peaks representing the vibrational modes of interest and the corresponding resonant frequency which can then be modelled on a 3D wire-frame model.

4.2.4 Experimental setup

The setup for EMA of the needle devices is shown in Figure 4.7. The transducer is excited between 0 and 80 kHz with a random excitation signal produced by data processing and hardware (Data Physics, Quattro). Before exciting the transducer, the signal is passed through a power amplifier (ETS Solution, HPVA-62) to gain a resolvable signal to noise ratio. The vibration velocity response is measured using a 3D LDV, (Polytec, 3D CLV) across the grid of measurement points on the transducer. The FRFs obtained are recorded on a desktop PC using data acquisition software (Signal Calc 240, Data Physics Corp). The data is then exported for processing in MEScopeVES.

4.2.5 Validation of FEA results

EMA validates the modal frequencies and mode shapes predicted by FEA and confirms that the device is designed to the design criteria defined in Table 3.1. This validation is completed for every prototype and the results for USN3 are detailed in this section. The results for the other prototype devices are then summarised in Chapter 5. Figure 4.9 shows a zoomed curve fitted FRF extracted from EMA showing the three modes in 20 - 30 kHz range. Figure 4.8 compares the resonant frequencies and corresponding mode shapes measured by EMA and predicted by FEA for USN3 of the tuned L2 mode and the B7 and B8, modes with the closest resonant frequencies.

As seen in Figure 4.9 the L2 mode dominates the response due to the axial excitation of the transducer, which does not promote bending responses. The results show a frequency

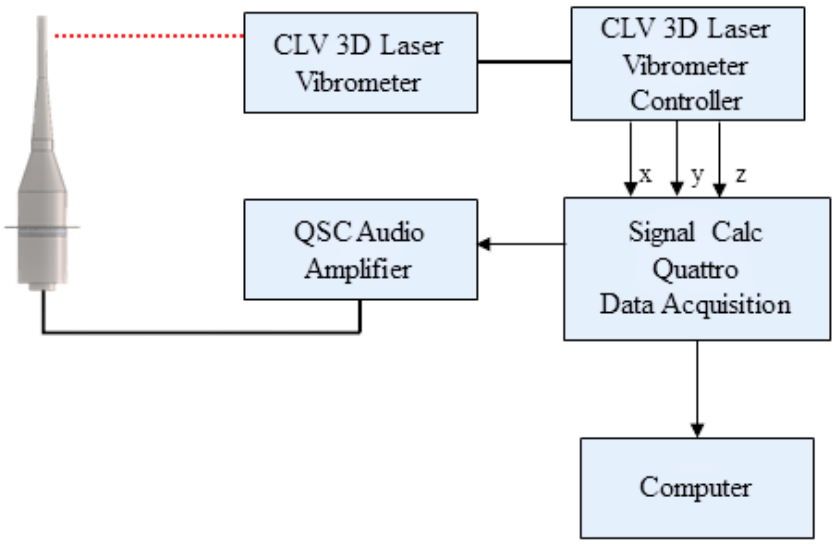

Figure 4.7: Schematic of EMA set-up

spacing of 11% and 7% for B7 and B8, respectively. While a 10% frequency spacing is the design criteria, and therefore target spacing, it is known that it is more important to adhere for the lower frequency mode because the L2 mode frequency tends to decrease under operation of the device.

The EMA shows good correlation with the FEA predictions with the FEA model being marginally stiffer in bending motion than the actual needle device, which is typical for FEA dynamic models. The differences between FEA estimates and the EMA measured frequencies are 0.4%, 0.9% and 3% for L2, B7 and B8 respectively. There is a strong correlation between the FEA and EMA for all prototypes (see Chapter 5) confirming FEA as an accurate technique for designing ultrasonic needle devices based on their modal behaviour.

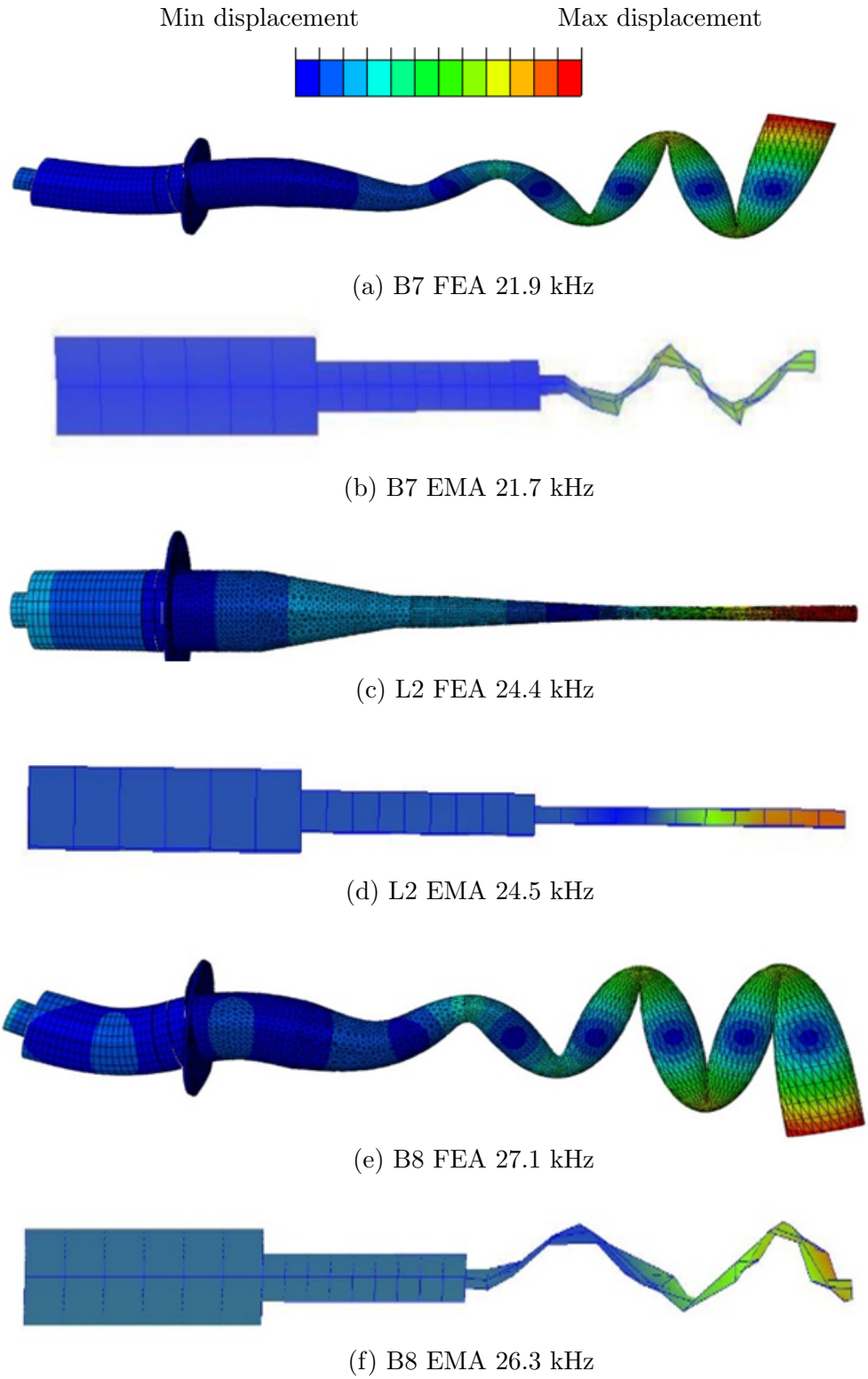

(a) B7 FEA 21.9 kHz

(b) B7 EMA 21.7 kHz

(c) L2 FEA 24.4 kHz

(d) L2 EMA 24.5 kHz

(e) B8 FEA 27.1 kHz

(f) B8 EMA 26.3 kHz

Figure 4.8: Resonant frequencies and corresponding mode shapes from FEA and EMA

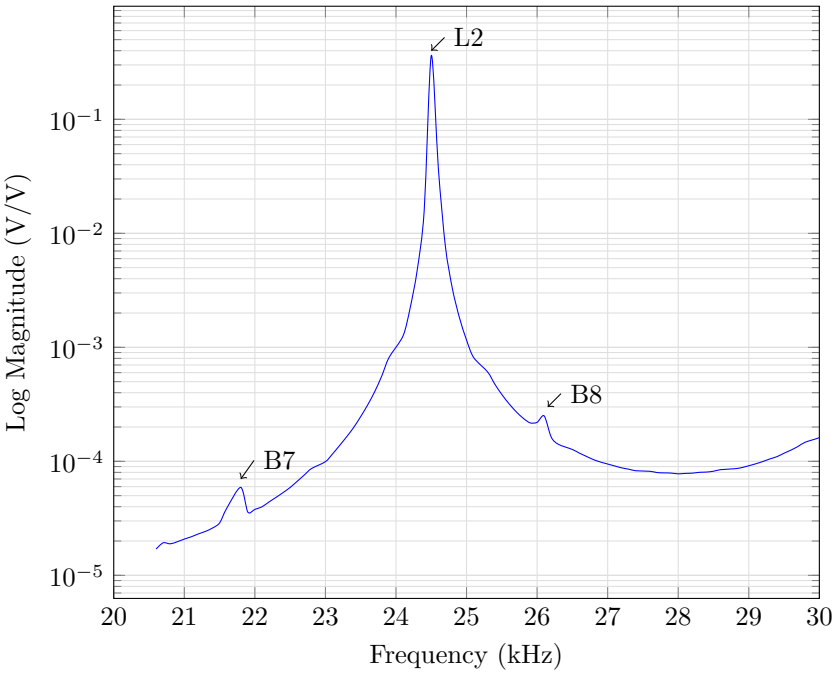

Figure 4.9: Curve fitted FRF of USN3

4.3 Resonance tracking system

Power ultrasonic transducers are susceptible to resonant frequency shifts and electrical impedance variations due to high input power levels, changing loading conditions and self-heating. The result can be low power conversion, poor performance and unstable vibration response. To ensure that the power ultrasonic devices are driven continually at their tuned resonant frequency, a resonance tracking system is used. This system measures the voltage and current in real-time and calculates the impedance of the power ultrasonic device, then adapts the voltage and frequency to ensure that the device is driven at zero phase and constant current amplitude [182].

The resonance tracking system is developed in this study to provide more control of the driving signal. Perhaps the most significant adjustment is the removal of the vibration stabilisation component of the driving system, instead focusing on maintaining resonance throughout operation. As the ultrasonic needle devices tend to excite high order bending modes close to the tuned L2 mode frequency, it is deemed important to focus efforts on driving the needle with a purely axial motion. The system will allow for altering the driving signal profile, achieved by enhancing the functionality of the system to investigate different waveforms and pulsing. An investigation of different driving signal is a key part of the study

to analyse the effects on penetration speed and temperature.

4.3.1 Operating principle

The principle of the resonance tracking system is that ultrasonic transducers are operating in resonance when the impedance phase is zero. To model the operation of the transducer-needle device, the Butterworth Van Dyke model (BVD) is assumed. The BVD model is a lumped parameter model commonly used to analyse piezoelectrical transducers operating at resonance. The model consists of a mechanical arm with a capacitor C_1, resistor R_1 and inductor L_1 in series, representing a mechanical compliance, a mass component and a mechanical loss respectively. The electrical arm comprises of a capacitance, C_o, representing capacitance of the clamped transducer and R_o, the dielectric loss resistance. R_o is neglected in this study as it commonly has a value much higher than the other parallel components.

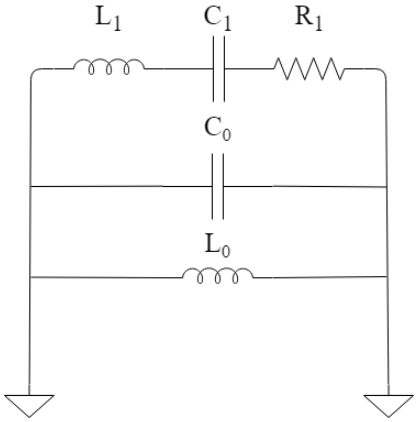

Figure 4.10: BVD model of a transducer operating near resonance with a shunt inductor

The components of the mechanical arm R_1, L_1 and C_1 vary considerably while driving due to the high-power levels, self-heating and load variations. Changes to the component values of L_1 and C_1 will shift the resonant frequency while alterations in R_1 impacts the electrical impedance at the resonant frequency. These variations are addressed by maintaining resonance and adjusting the amplitude of the driving signal to maintain constant vibration amplitude. When unloaded, C_o does not greatly influence the transducer performance $f_s \approx f_r$. However, when loaded, the resulting reactive impedance results in low admittance. Figure 4.10 illustrates a solution where a shunt inductor L_o is used to tune out the clamped capacitor C_o. The adoption of this technique is discussed in Section 4.3.4.

4.3.2 Software

The resonance tracking system is implemented in LabVIEW (National Instruments), an abbreviation of Laboratory Virtual Instrument Engineering Workbench. LabVIEW differs from traditional programming language as it uses graphical notation. Advantages of LabVIEW are the extensive support for accessing instrumentation hardware and the modularity which allows the system to be extended.

The resonance tracking system consists of two main modules, the impedance calculation and the control module. Within the impedance calculation the current and voltage are sampled and digitised by a cross-correlation method and used to calculate the magnitude and phase of the electrical impedance. To keep the impedance phase at zero and achieve resonance tracking the control module adjusts the frequency of the function generator using a proportional-integral-derivative (PID) controller. The phase error $\Delta\theta$, which is the difference between the target phase and the measured, is applied to the PID controller to compute the frequency increment. The frequency at the output of the function generation is incrementally altered until the phase error, $\Delta\theta$, equals zero. The vibration stabilisation loop, if in use, operates in a similar manner where the current error, Δi, which is the difference between the target current and the measured current is applied to the PID controller. The output is used to adjust the amplitude of the driving voltage until the current reaches the desired value.

In the original setup the vibration stabilisation loop would only operate when the $\theta < 5°$. This is for safety reasons as high impedance is apparent when the phase is far from zero. To maintain a practical current value a large voltage amplitude is required which could damage the transducer.

4.3.3 Hardware

The experimental setup can be seen in Figure 4.11. The frequency tracking algorithm is controlled using LabVIEW within a data acquisition device (National Instruments, PXIe 5122 on PXIe-1071 chassis). The voltage and current signals are measured using a voltage probe (Tektronix, P6139A) and current probe (Tektronix, P6022). The resonant tracking protocol controls the settings of a function generator (Agilent, 33210A) which generates the driving signal, with frequency and voltage amplitude determined by the tracking algorithm. A power amplifier (E&I, 240L) is used to amplify the output signal of the function generator

before it is supplied to the ultrasonic device.

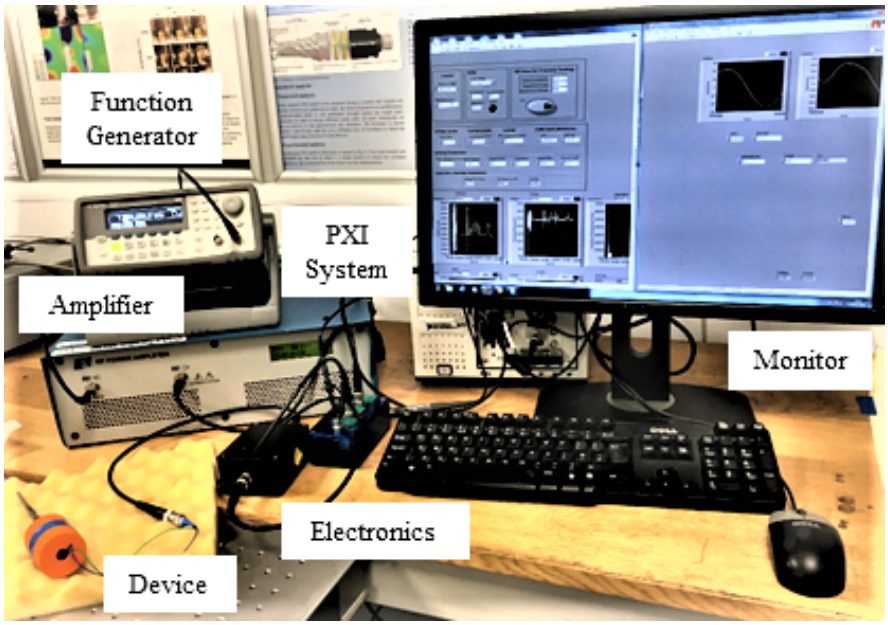

Figure 4.11: Resonant tracking system set-up.

4.3.4 Impedance matching

Impedance matching is crucial in high power applications to achieve optimal power transfer. Commonly defined as the maximum power transfer theorem, optimal power is transferred to the source from the load when the load impedance matches that of the source. For an AC source, with internal impedance of Z_S driving a load with impedance of Z_L, the basic circuit is shown in Figure 4.12. The BVD model representing a transducer at resonance is utilised to propose an appropriate technique to match the ultrasonic transducer device with the amplifier of output impedance 50Ω.

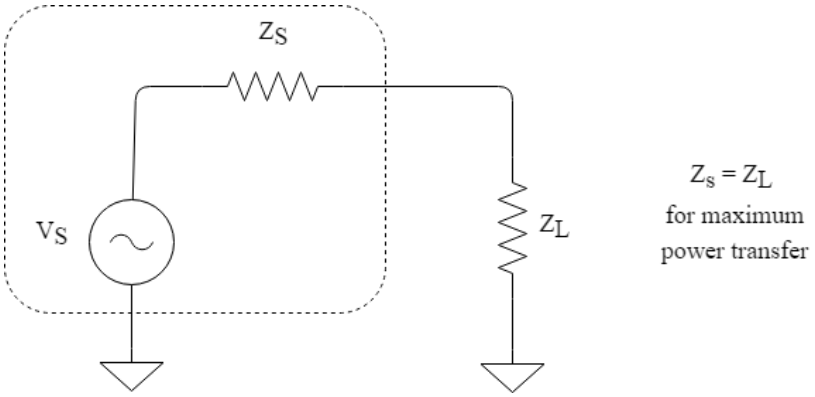

Figure 4.12: Impedance matching circuit for a voltage source and load

Coil Transformer

A transformer is used to transform one voltage or current into a voltage or current either higher or lower than the original value. The most basic equation for a transformer coil for voltage is given as:

$$\frac{V_P}{V_s} = \frac{N_P}{N_S} \tag{4.7}$$

where V_P over V_S is the transformer voltage ratio, defined by the ratio between the number of turns on the primary winding, N_P, to the number of turns on the secondary winding, N_S. Using Ohm's Law, the transformer impedance ratio is obtained:

$$\frac{Z_P}{Z_s} = \left(\frac{N_P}{N_S}\right)^2 = \left(\frac{V_P}{V_S}\right)^2 \tag{4.8}$$

The operating principle of the transformer is based on mutual inductance; a magnetic link between two coils due to a common magnetic flux. This is achieved based on Faraday's law of induction which defines a relationship between the changing AC electric field and the resulting magnetic field. Stray or leakage inductance is a common issue with this type of transformer and would normally be compensated for. However, for the resonance tracking system the inherent inductance of the coil acts as the shunt inductor to cancel out C_o in the BVD model. The inductance of a toroid coil can be approximated as:

$$L \approx \frac{\mu_{rp} N^2 A}{2\pi r} \tag{4.9}$$

where μ_{rp} is the relative permeability of the core, N is the number of turns, A the cross-sectional area and r the radius of the toroid. Equation 4.9 is used to define a coil suitable to match the output impedance of the amplifier and shunt the inductive component of the ultrasonic needles.

Experimental validation

A ferrite toroid, Ferroxcube and copper wire is used to create the transformer. The impedance analyser is used to validate that the impedance of the transducer is lowered by adding the transformer. Figure 4.13 displays the final coil created for USN3 while Figure 4.14 shows the electrical impedance and phase magnitude with and without the matching coil.

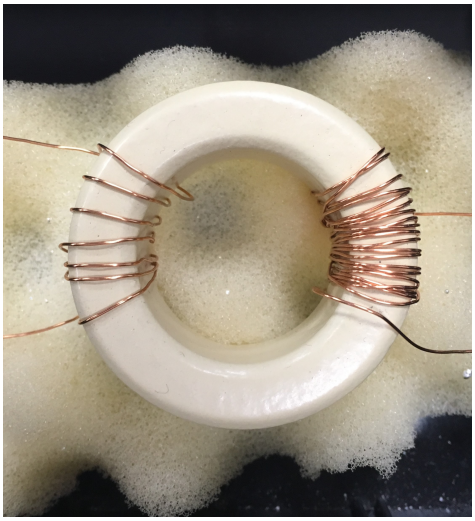

Figure 4.13: Transformer coil of USN3

The transformer coil possesses seven turns on the primary side which connects to the amplifier and twenty-one turns on the secondary side which connects to the transducer. Without the coil the impedance curve is capacitive, the slope decreasing to a minimum impedance magnitude which corresponds to the resonant frequency f_r, before a sharp incline until the maximum impedance is reached which corresponds to the anti-resonant frequency f_a. However, the coil causes a 180° shift, resulting in an inductive response characterised by an upward slope reaching the anti-resonant frequency f_a before a sharp decrease until the minimum occurs at the resonant frequency f_r. The load impedance Z_L of the resonant frequency f_r is 415 Ω with no coil and 52 Ω with the coil, better matching the power amplifier

which has an output impedance of 50 Ω. The 180° shift is also represented in the phase spectrum as shown in Figure 4.14(b). Although the phase amplitude sweeps between +90° and -40° in comparison to the transducer without matching which sweeps 180° between +90° and -90°, the phase magnitude is 0° at the f_r, as desired.

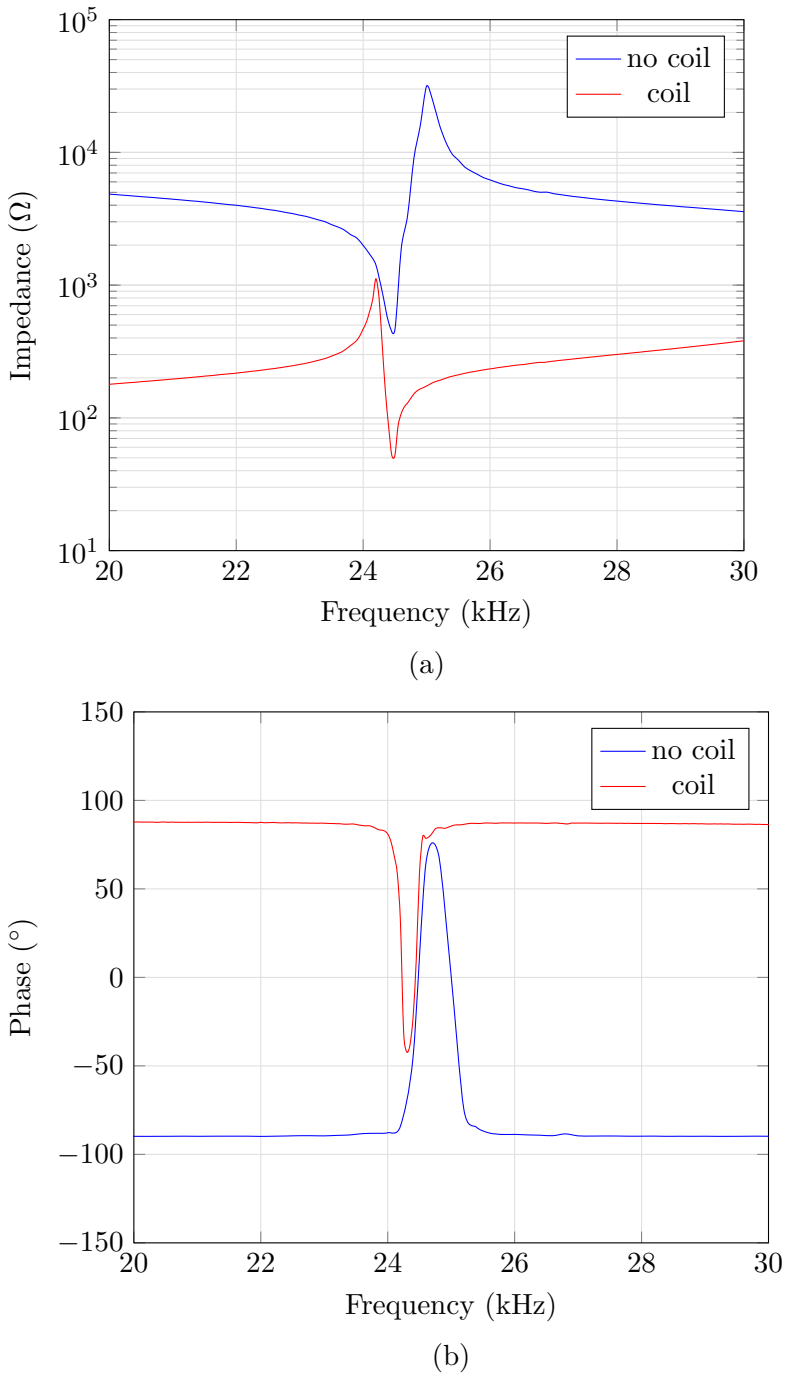

Figure 4.14: Impedance (a) magnitude and (b) phase of USN3 with and without the matching coil

Validation of the transformer's ability to improve the operating amplitude of the needle is sought by measuring the longitudinal component of the displacement amplitude at the tip of the needle using a 1D laser Doppler vibrometer (Polytec, OFV 3001 with OFV 303 sensor head). The 1D LDV is configured to measure the longitudinal vibration by directing the laser axially onto the needle tip. The device is driven under no-load conditions with the transducer driven at incremented excitation values up to 60 V_{pp}.

Figure 4.15 displays the displacement amplitude at the needle tip with and without the matching circuit. The longitudinal displacement of the device is considerably higher adding the matching circuit. For example, for a supplied excitation of 40 V_{pp}, without a coil produced 12 μm while adding a coil produced 25 μm, an improvement of over 100%. The difference in the response is larger at higher excitation levels as coil transformers operate more effectively at higher excitation levels.

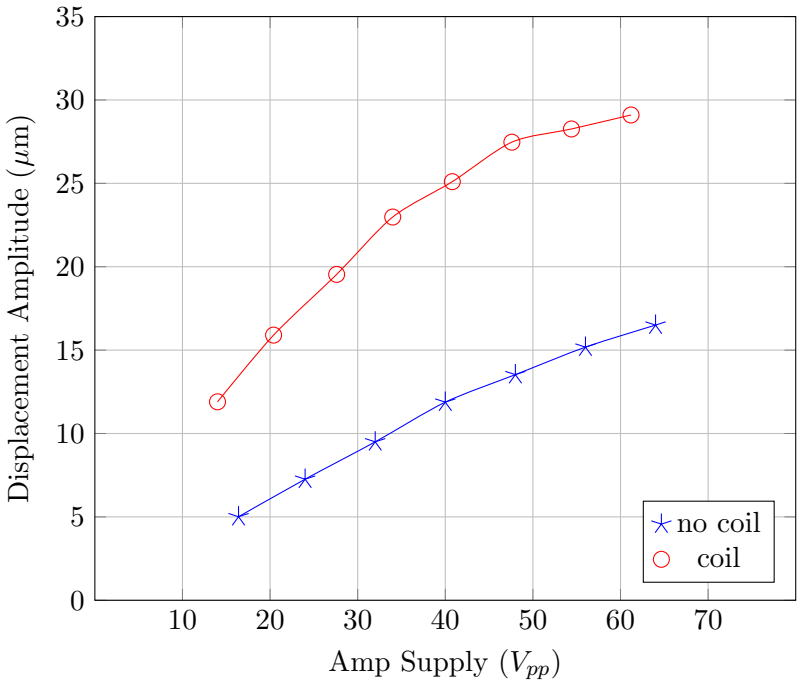

Figure 4.15: Displacement amplitude with and without matching transformer

4.3.5 Experimental validation of tracking system

Following the study of the matching circuit, validation of the whole tracking system is conducted. USN3 is driven under no-load in air and the 1D LDV (Polytec, OFV 3001 with OFV 303 sensor head) is used to measure the longitudinal displacement at the needle

tip. Initially the needle is driven at a fixed frequency for two minutes for three voltage levels, 34 V_{pp}, 48 V_{pp} and 62 V_{pp}. The constant driving frequency, f_r, as determined from the measured impedance. In the second set of tests the tracking system is used to monitor the impedance of the device, altering the frequency to maintain zero phase. The matching circuit is used in both tests, and the results are shown in Figure 4.16.

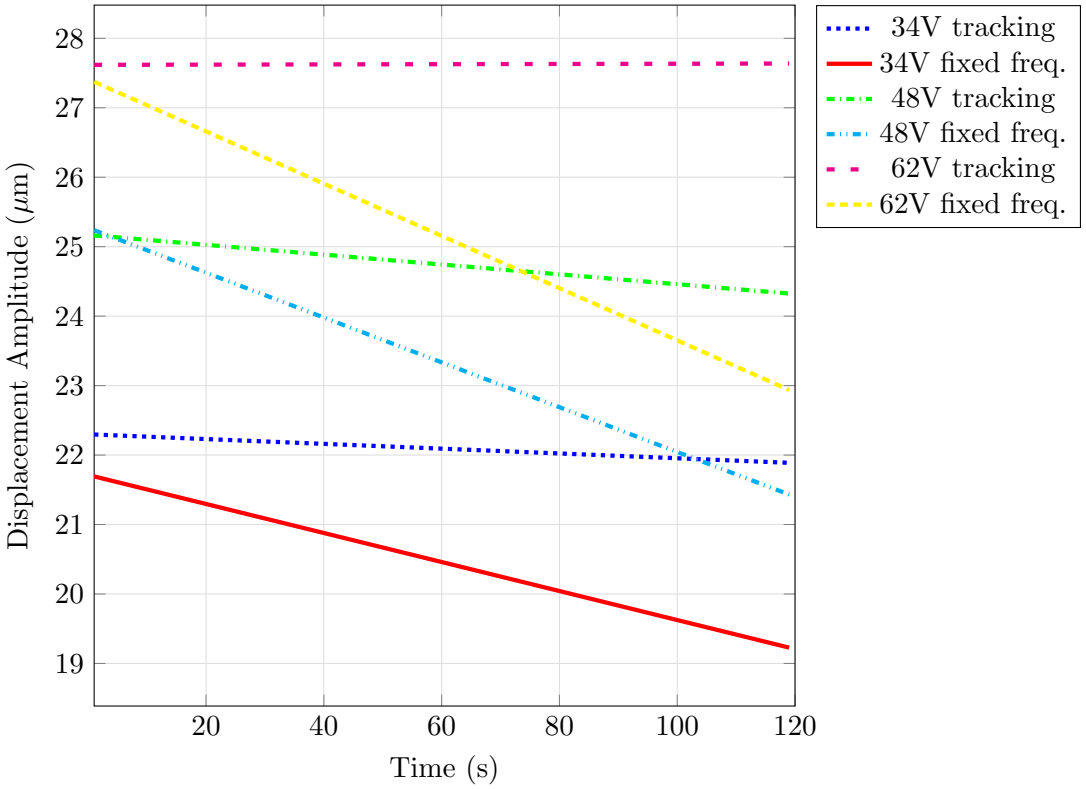

Figure 4.16: Needle tip displacement amplitude for fixed frequency and for tracking.

Using frequency tracking the displacement amplitude remains constant for all three driving voltage levels, while the phase is being tracked and the frequency adjusted. However, when tracking is not used the displacement amplitude at the tip of the needle drops by 1.1, 1.8 and 2.2 μm per min for 34, 48 and 62 V respectively.

These results are consistent with device self-heating where heat affects the elastic compliance of the piezoelectric material which causes the resonant frequency to shift downwards as it becomes less stiff. Self-heating increases with increasing excitation level, meaning that the frequency change is larger, and the amplitude reduces at a higher rate.

The LabVIEW program provides the facility to monitor the frequency corrections. Figure 4.17 shows the frequency at which the device is driven for the three voltage levels over the two-minute period. Predictably, the frequency shift required to maintain resonance is larger

the higher the input voltage. After two minutes, the maximum adjustment is 238 Hz for the highest voltage level, demonstrating the importance of using tracking when driving high power ultrasonic devices, both under no-load and under load.

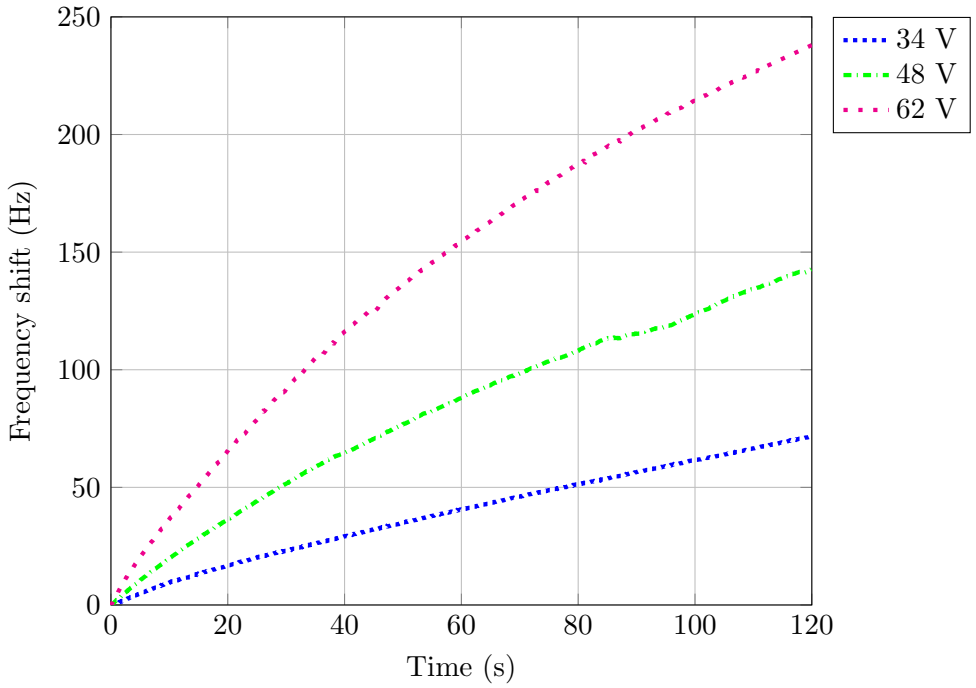

Figure 4.17: Frequency shift when driving USN3 at three excitations levels for 2 minutes

4.4 Investigation of optimal driving conditions

One of the primary advantages of adopting a system which is LabVIEW based is that the functions can be altered and extended, enabling an investigation into how modifications of the driving signal affect the rate of penetration progress of the needle and the temperature at the site. One of the main concerns related to high power ultrasonics surgical devices is heat, the two main sources being self-heating of the device and frictional heat at the contact site. Frictional heat is related to the displacement amplitude of the needle and the activation time [183], while self-heating is commonly sourced at the piezoelectric stack.

Power modulation is an established technique in phacoemulsification, an ultrasound-based surgery discussed in Section 2.3, where ultrasound energy is delivered to break up a cataract before removal. Power modulation has proven advantages in reducing heat and therefore the risk of thermal injury. The aim in phacoemulsification is to avoid burning the cornea or damaging the delicate ocular structures, by applying less 'phaco' energy to the site to

avoid thermal damage, which is also an important consideration for the ultrasonic needle application.

The three most widely used methods of power modulation are continuous, pulse and burst and are shown in Figure 4.18 and all are controlled by the clinician through depression of a food pedal of the phaco driving system. In phaco continuous, the energy is delivered with increasing power as the foot pedal is pressed. In pulse mode, pulses of energy are delivered at increasing power level on depression of the foot pedal. After each pulse of energy there is a period where no energy is delivered, the 'off period'. Equal 'on' and 'off' time reduces heat and delivers half the energy into the eye. Finally, in burst mode the power is constant for all the 'on' but the interval between each burst decreases as the foot pedal is depressed so that the 'off' period is shortened and the burst frequency increases. At full depression the power delivery is continuous.

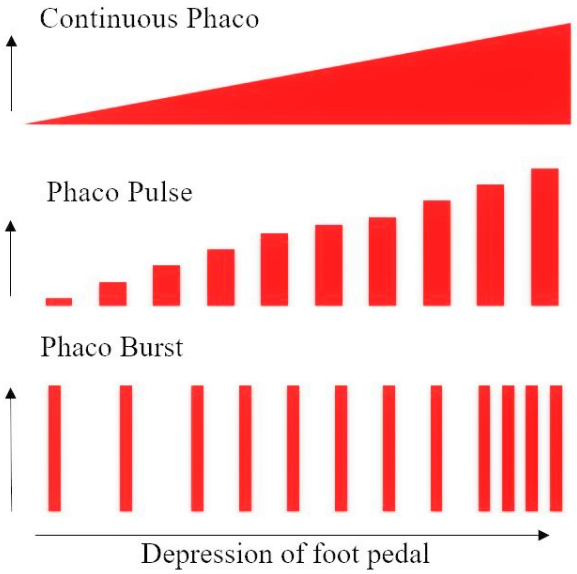

Figure 4.18: Power modulation methods

This study adopts a variation of these power modulation techniques to determine if they can similarly result in heat reduction benefits in penetration of bone using the ultrasonic needles. Initially various waveform shapes (sine, square, ramp-down and triangle) are tested to determine whether the resonance tracking system could maintain resonance of the needle device. The signals which produce the highest displacement amplitudes are used to excite the needle while penetrating Sawbone®. The speed of penetration and the temperature around the site are monitored to evaluate each signal.

4.4.1 Vibrational amplitude: waveform shapes

The displacement amplitude at the needle tip is measured while driving under no load for four waveform shapes. The displacement amplitude of the tip of an ultrasonic cutting device is known to be related to the achievable cutting speed. Generally higher ultrasonic amplitude results in a faster cut. These tests therefore initially evaluate which waveforms could provide the fastest penetration speed. The different waveform shapes are tested at three voltage levels as shown in Figure 4.19.

The square waveform excites the highest displacement amplitude, followed by sinusoidal, triangular then ramp-down. The ramp down and triangular waveforms are similar because they are constructed by combining a series of sine waves harmonics. This may be reducing useful energy that can be translated into motion by the transducer as the energy of these harmonics are not at the tuned frequency. However, the square wave also contains harmonics so further investigation of the waveforms for the ultrasonic needle under loaded conditions. A sinusoidal, square and triangular waveform are used for this.

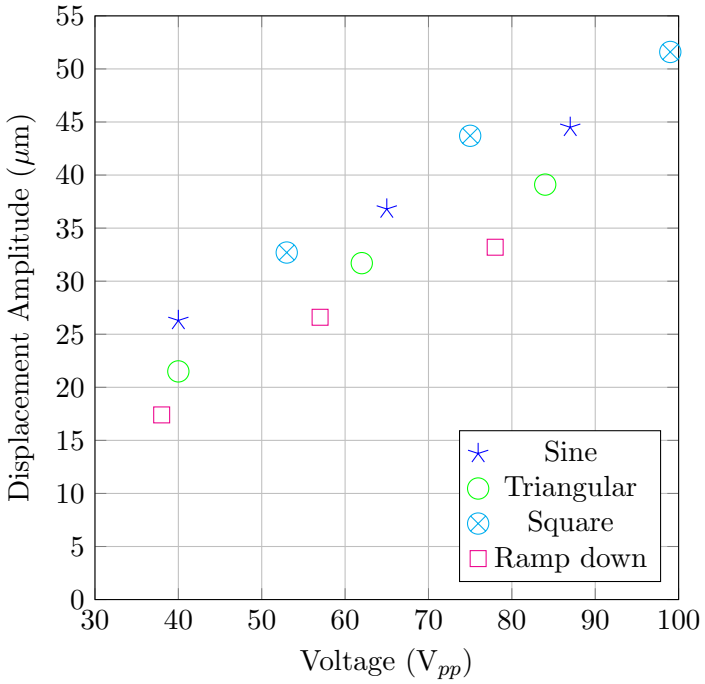

Figure 4.19: Displacement amplitude at the tip of the needle for different driving waveform and voltage levels

4.4.2 Penetration tests: waveform shapes

The waveforms are further investigated as driving signals for needle tests within a bone mimic material, Sawbones® (Pacific Research Laboratories, Inc). Sawbone® is chosen as the target material as it is homogeneous and has similar Young's modulus and density of trabecular bone, making it suitable for comparative measurement of the penetration speed. Sawbones® is not suitable for directly evaluating temperature in bone as it does not exhibit comparable thermal properties, however it does provide a suitable consistent test material for comparing the effects of the driving signal waveform and power modulation on the temperature at the needle.

Two voltage levels are used; 85 V_{pp} and 125 V_{pp}, which are both capable of producing sufficient displacement amplitude at the needle tip to penetrate 5 mm into Sawbone® within twenty seconds. A twenty second duration is selected to follow a typical time to perform the same needle penetration in Sawbone® with a trephine needle. The three waveforms (sine, square and triangular) are used to drive the needle device at the two voltage levels. Repeating each test three times, the time to penetrate 5 mm is recorded and the maximum temperature within the boxed area, as shown in Figure 4.20, at the penetration site measured using a thermal camera, T420, Flir Systems.

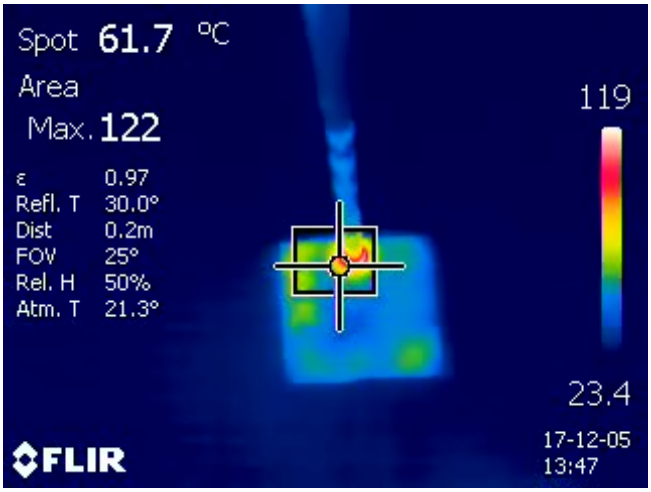

Figure 4.20: Thermal image of ultrasonic needle penetrating Sawbone sample

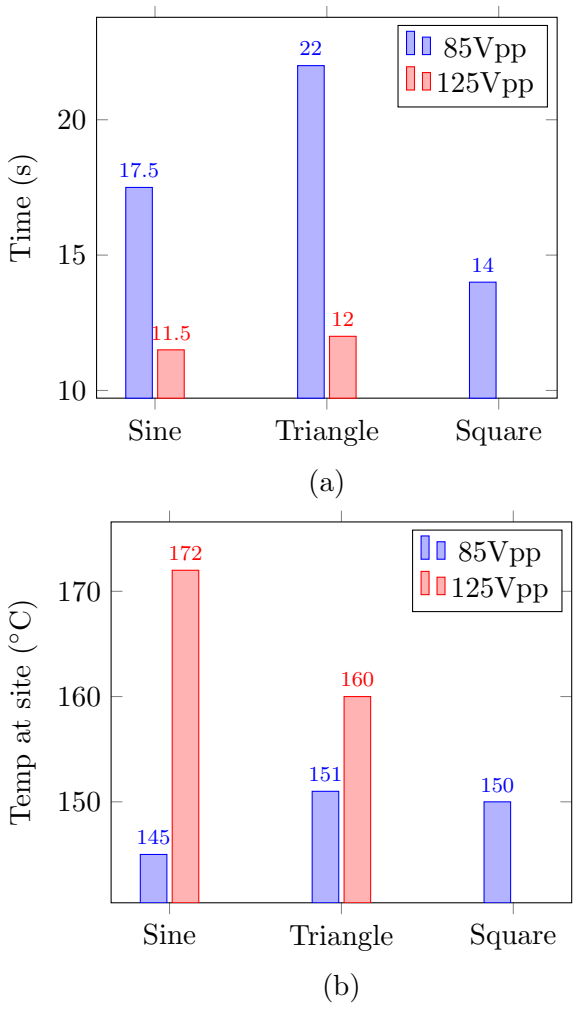

Figure 4.21: Penetration (a) time and (b) temperature for three driving waveforms and two voltage levels

Figure 4.21 shows that the fastest penetration is achieved using a sinusoidal waveform at both voltage levels, but this also resulted in the highest temperature at the site. Faster penetrations are achieved for higher excitation levels, correlating with the suggestion that larger displacement amplitudes will allow faster penetrations. However, temperature at the penetration site is also higher for the higher voltage levels suggesting higher displacement amplitudes result in high amounts of friction at the tip to mimic interaction.

A penetration could not be achieved for a square wave at 125 V_{pp} because when driving with a square wave under load, power is reflected back to amplifier. Square waves are generally accepted for low power ultrasonics, however for power ultrasonic applications where high voltage levels are required the high current slew rate can cause cracking, reduced life of the piezoceramics and other failures.

Despite the sinusoidal waveform producing the highest temperature for the highest excitation, it is surmised that this is due to the high vibrational response as it also penetrated the sample in the quickest time. For this reason, it will be used to investigate potential pulsing regimes.

4.4.3 Penetration tests: power modulation

Next, power modulation similar to those used in phacoemulsification, is investigated, aiming to reduce temperature at the site. The effect of different power modulation variables defined in Figure 4.22 on penetration speed is investigated. A sinusoidal waveform is selected, with a maximum input voltage (MIV) of 125 V_{pp} and pulse period of 8 seconds. The duty cycle (DC, the percentage of time the signal is at the MIV) and the low power percentage (LPP, the percentage MIV applied during a low power period) are both varied between 25 and 100%. Once again, the penetration time and temperature are monitored using the thermal camera.

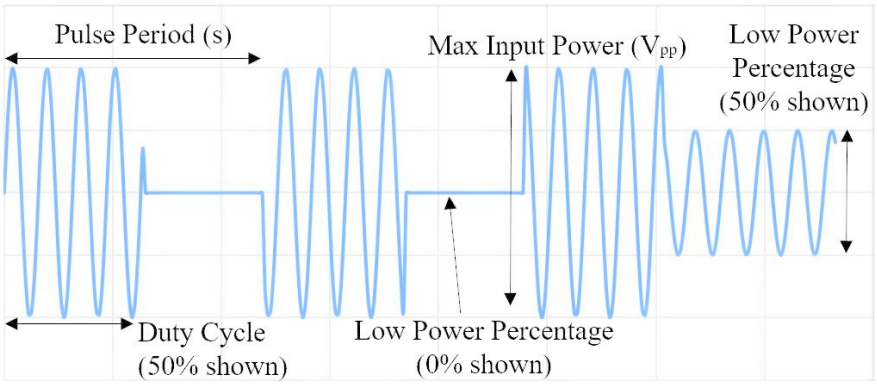

Figure 4.22: Variables of power modulation

The results are presented in Table 4.2 and show that low duty cycle or lower LPP cause substantially longer penetration times. However, the temperature at the penetration site of the Sawbones® also decreases as the duty cycle and LPP are lowered. The results suggest that incorporating a duty cycle with periods of lower excitations could be an effective technique to reduce thermal build-up at the penetration site however a trade-off between the time and temperature is required.

Duty Cycle	Time (s)	Low Power Percentage 0%	25%	50%	75%
	25%	85	60	28	14
	50%	27	24	17	13
	75%	14	13	13	13
	100%	10	10	10	10

(a)

Duty Cycle	Temp (°C)	Low Power Percentage 0%	25%	50%	75%
	25%	136	141	156	173
	50%	144	150	170	174
	75%	165	167	172	171
	100%	174	174	174	174

(b)

Table 4.2: (a) Time and (b) temperature for the different power modulations

4.5 Chapter conclusion

Characterisation of the devices is conducted using electrical impedance analysis and experimental modal analysis (EMA). Assembly of the device involves preloading the piezoceramic stack with sufficient prestress identified by consolidation of the modal frequencies and a high electromechanical coupling factor. Experimental modal analysis measures the dynamic behaviour of the device validating the predictions of the FEA. Close correlation between FEA and EMA of USN3 with errors of 0.4%, 0.9% and 3% for L2, B7 and B8 confirms FEA as an accurate technique for the design ultrasonic needle devices. The L2 mode dominates the response of the curve fitted FRF of USN3 suggesting that an axial response without coupling with neighbouring bending motion has been excited.

Driving the needle at its tuned frequency is achieved by adopting a resonant tracking system. Alongside a matching circuit the vibrational stability and power conversion is improved, validated by monitoring the longitudinal vibration at the tip of the needle insert. Waveform shapes and power modulation of the excitation signal is then investigated by expanding the functionality of the system. A square waveform excited the highest displacement amplitude but proved unstable when driven under load. Inspired by power modulation used in phacoemulsifcation, intervals of low voltage were introduced to reduce temperature at the penetration site. The results suggest that a trade-off between the penetration time and the temperature is required if duty cycle or periods of lower excitation are incorporated. A summary of the experimental procedures conducted in Chapter 4 is provided in Table 4.3.

Assembly	Configuration	The transducer components (bolt, end masses, piezo rings and needle) are carefully configured to ensure strong electrical and mechanical contact. Acetone is used to remove dirt or grease, while insulation tape prevents a short between piezoceramic rings.
	Preload	Preload is applied in steps using a torque wrench to ensure no gaps between components, effective electro-mechanical coupling and lowest possible impedance. The transducer performance is monitored by obtaining the impedance spectrum and the generated charge across the stack.
Validation	EMA	EMA was performed by exciting the device and measuring the vibration response across a grid of points on the surface of the device. FRFs were measured across a grid of points and curve-fitted. The magnitude and phase data are then applied to a geometric model of the measurement grid, allowing animated mode shapes to be derived at each modal frequency.
Excitation	Driving system	A resonance tracking system is used to ensure the devices are driven at their tuned resonant frequency, at zero phase and constant current amplitude. The system consists of the frequency algorithm implemented in LabVIEW, a voltage and current probe, function generator and power amplifier.
	Impedance matching	To achieve optimal power transfer a coil transformer is realised using a toroid. The ultrasonic transducer device is matched with the amplifier with an output impedance of 50Ω while also compensating for reactive capacitance.
	Driving conditions	Power modulation techniques including waveform shapes and pulsing were investigated by monitoring time and temperature during the penetration of Sawbone.

Table 4.3: Summary of experimental procedures

Chapter 5

Device evaluation

Preceding chapters have described the design of four variants of a high power ultrasonic needle for bone biopsy; three axial vibrating needles, USN1, 2 and 3 and a composite mode L-T needle, USNLT. This chapter details the penetration tests conducted to evaluate each device. Biomechanical test mimic, Sawbones®, is used initially as it offers similar mechanical properties to bone and is available in different variations to represent the different bone tissues.

Penetration tests in animal bone samples followed, evaluated against a conventional trephine needle. The structural quality of the penetration site and the samples retrieved by the needles are assessed using micro-Computed Tomography (μCT), in collaboration with the University of Edinburgh project partners.

For the L-T mode needle, the torsionality of the needle tip is measured over a range of input driving voltages. USNLT is then used to penetrate Sawbones® and animal bone, comparing the architecture of the biopsy samples and the penetration time against an L-mode device. The damage comparison is achieved through X-ray micro-Computed Tomography (μCT), conducted at the University of Strathclyde.

5.1 First prototype of longitudinal needle: USN1

Resonant needle USN1 pictured in Figure 5.1 is the first device to be realised during this study. The transducer consists of titanium end masses, copper electrodes, two PZT8 rings, held under compression by a class 12.9 M5 screw. This is connected by an M6 threaded joint to a stainless steel needle with inner diameter of 1.8 mm tuned by FEA at 25.9 kHz.

Figure 5.1: Longitudinal ultrasonic needle, USN1

EMA measured L2 at 25.7 kHz with the closest bending modes B8 and B9 at 22.8 kHz and 27.7 kHz respectively. This gave a final frequency spacing of 11% and 8%. The error between the FEA estimated and EMA measured frequencies for the bending modes, B8 and B9, is 2.1% while L2 differed by only 0.8%. The high modal density can be observed in the curve fitted frequency response, FRF, for USN1 in Figure 5.2. The dense modal response due to the slender hollow profile of the needle results in many high order bending and torsional modes excited in the measured range between 0 and 80 kHz frequency range. However sufficient frequency spacing, 8% attained through a combined FEA and EMA process will reduce the likelihood of modal coupling during operation. The vibrational amplitude gain of the device is 6.25.

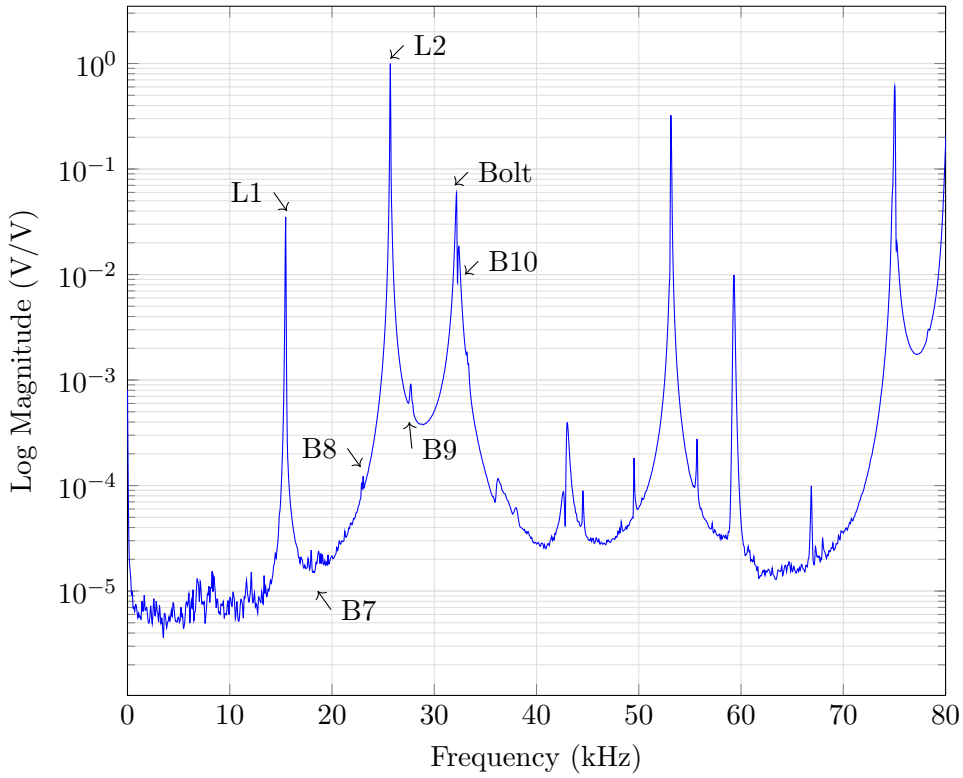

Figure 5.2: Curve fitted FRF of USN1

5.1.1 Penetration tests: Sawbones®

The first penetration tests are conducted in the biomedical bone mimic Sawbones®. Sawbones® is available in a variety of densities from 0.12 to 0.32 g/cm^3, with cell sizes ranging from 0.5 to 1.0 mm. Sawbones® nomenclature give their density values as pound per cubic foot (PCF), the PCFs of 10, 20 and 30 are shown in Figure 5.3 (a). USN1 performed a smooth 50 mm deep penetration into PCF 10, as shown in Figure 5.3 (b). There is little force required beyond self-weight and no signs of charring in or around the hole.

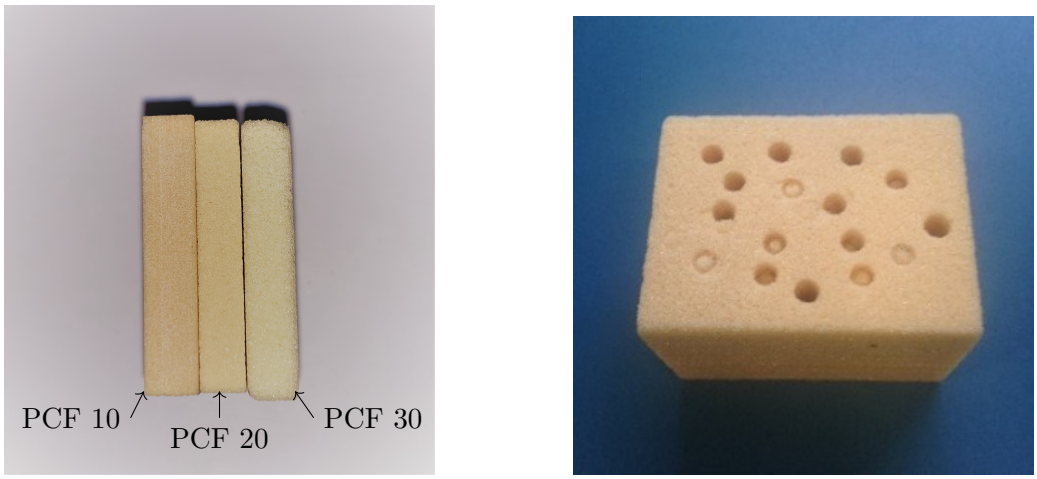

(a) (b)

Figure 5.3: (a) Sawbones® samples of PCF 10, 20 and 30 PCF (b) penetration tests through 10 PCF with USN1

5.1.2 Penetration tests: Wistar rat

USN1 is then tested in the femur bone of a 3 month old Wistar rat. Wistar rat is an outbred albino rat and a common laboratory rat strain. The femur is fixed into a bench-top vice and a 20 ml/min flow of phosphate buffered saline (PBS) is used to irrigate the site and prevent heating. Penetration is achieved by the operator applying only sufficient force to maintain good contact and sustain a forward motion. However, the operator also needed to apply a slow 120° rotation of the needle to sustain penetration without stalling.

It can be seen in Figure 5.4(a) that USN1 penetrated the cortical bone, however, no biopsy sample recovery is attempted in this test. A micro-CT (μCT) is used to characterise the mechanical damage. The internal structure of tissue is assessed non-destructively by scanning through 360° using a Bruker Skyscan 1172. A voxel resolution of 2.93 μm is used to ensure high quality images alongside four frame averaging and a random movement value of five for all scans. After scanning, the images are reconstructed and analysed using proprietary software (Nrec version 1.6.9.4, CTAn 1.13.5.1, and CTVox 2.6, also all by Bruker).

The μCT image in Figure 5.4 (b), revealed an irregular shaped hole but no large cracks. This suggests that the device can penetrate through rat bone without inducing severe mechanical damage, which is not possible using a trephine biopsy needle of similar diameter without inducing a catastrophic fracture. This demonstrated early that a power ultrasonic needle could penetrate delicate bone structures with a thin cortical layer and small diameter

without significant damage of the bone around the hole.

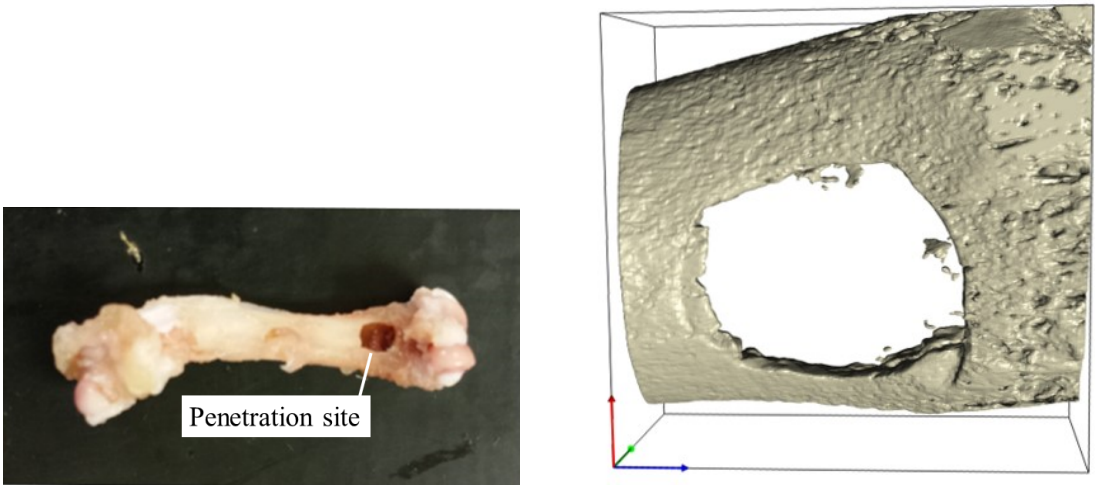

(a) (b)

Figure 5.4: (a) Wistar rat femur (b) μCT image of penetration site of Wistar rat femur

5.2 Second prototype of longitudinal mode needle: USN2

The second prototype needle displayed in Figure 5.5 consists of a Langevin transducer possessing two PZT8, titanium end masses and copper electrodes held under compression by a 12.9 M5 caphead screw. The stainless steel needle diameters tapers from 8 mm to 4 mm with a constant inner diameter of 2.8 mm and is connected to the transducer via a M6 threaded joint.

The device is tuned using FEA to be resonant in the second longitudinal mode at 23.0 kHz with neighbouring modes, the 8th and 9th bending modes, predicted at 21.0 kHz and 25.0 kHz. EMA identified the resonant frequency of L2 at 23.5 kHz and the 8th and 9th bending modes at 20.8 kHz and 24.5 kHz, respectively. This is a close match to the predicted values with errors of 0.8%, 2.1% and 1.8% for B8, L2 and B9 respectively. The FRF for USN2 shown in Figure 5.6 shows a dense modal spectrum. When driven the second longitudinal mode is excited without flexural or torsional modal coupling. The profile of USN2 provided a vibration gain of 8.

Figure 5.5: Longitudinal ultrasonic needle, USN2

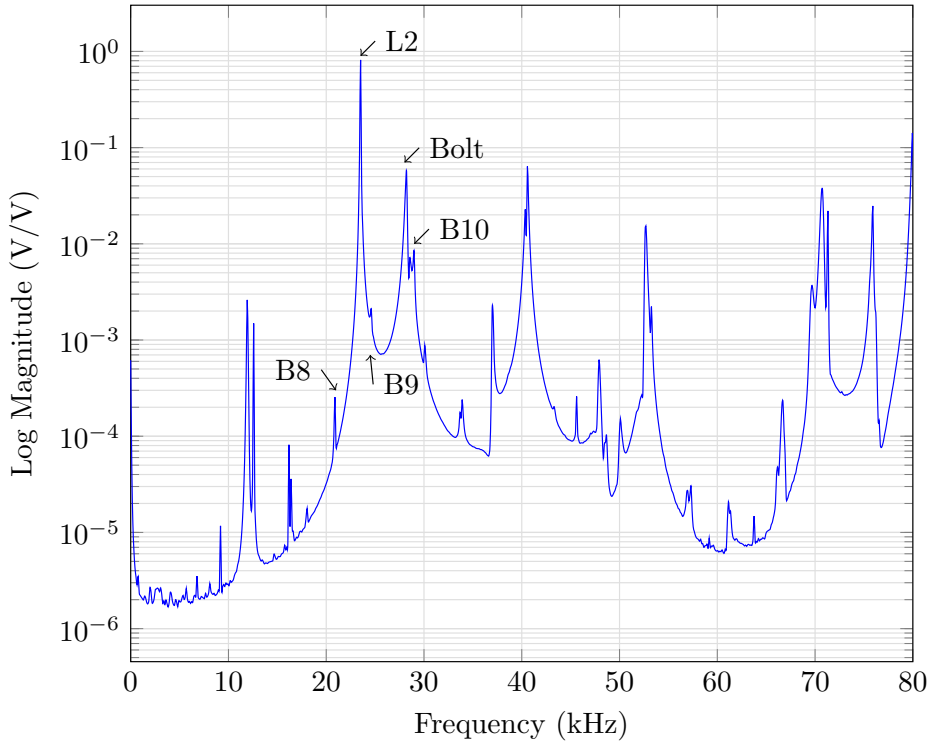

Figure 5.6: Curve fitted FRF of USN2

5.2.1 Ovine metaphyseal bone penetration

USN2 is used to penetrate the ovine metaphysis bone and recover biopsy samples. The metaphysis is the wider section, also called the growth plate and is located at the end of a long bone between epiphysis and the diaphysis, depicted in Figure 5.7. The test set-up is consistent with that used for USN1 with the bone fixed in a bench-top vice and a flow of PBS applied to the site and along the length of the needle length (Figure 5.8(b)). A trephine bone needle is also used to extract a bone biopsy sample.

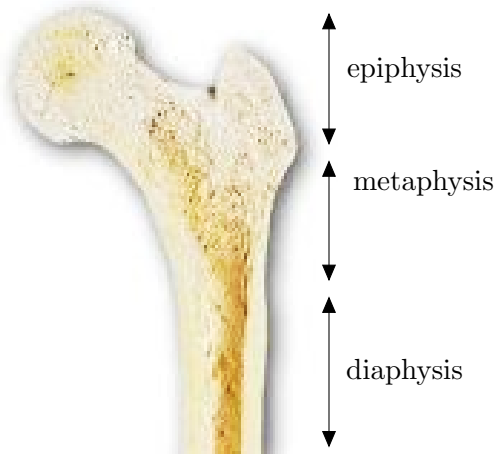

Figure 5.7: Structure of a long bone

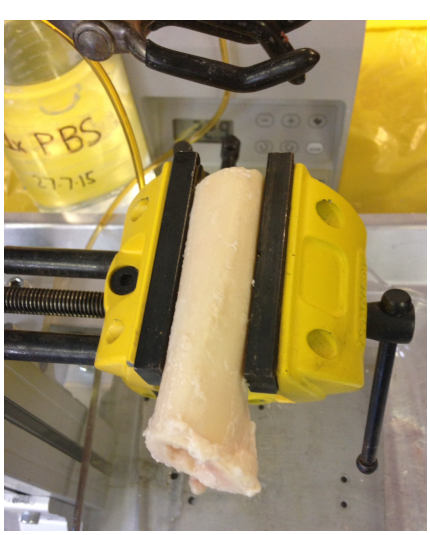

(a)

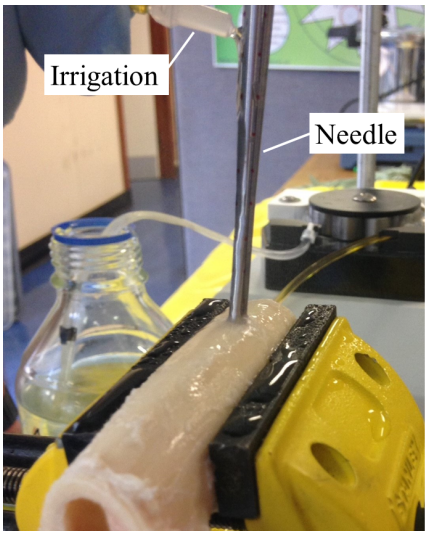

(b)

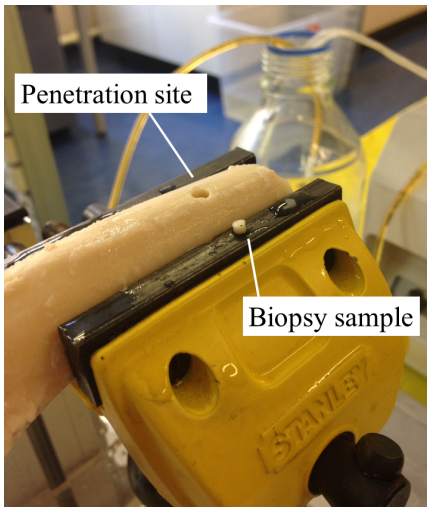

(c)

Figure 5.8: (a) Ovine metaphysis in clamp (b) USN2 during penetration (c) resulting penetration site and biopsy sample

μCT images of the frontal, sagittal and transverse planes and a 3D reconstruction of the metaphysis biopsies are presented in Figure 5.9 and Figure 5.10 for the trephine biopsy and USN2 frontal respectively. The samples extracted consisted of trabecular bone. Also called cancellous or spongy bone, these resemble a porous mesh structure and are found at the end of long bones and in the interior of vertebrae. From the μCT reconstruction, show in Figure 5.9(d), it can be seen that the trephine induced the least damage. However, damage to the trabeculae is observed at the right-hand side of the sample extracted by USN3, shown in Figure 5.10(d). Despite this USN3 extracted an intact and viable biopsy sample for analysis.

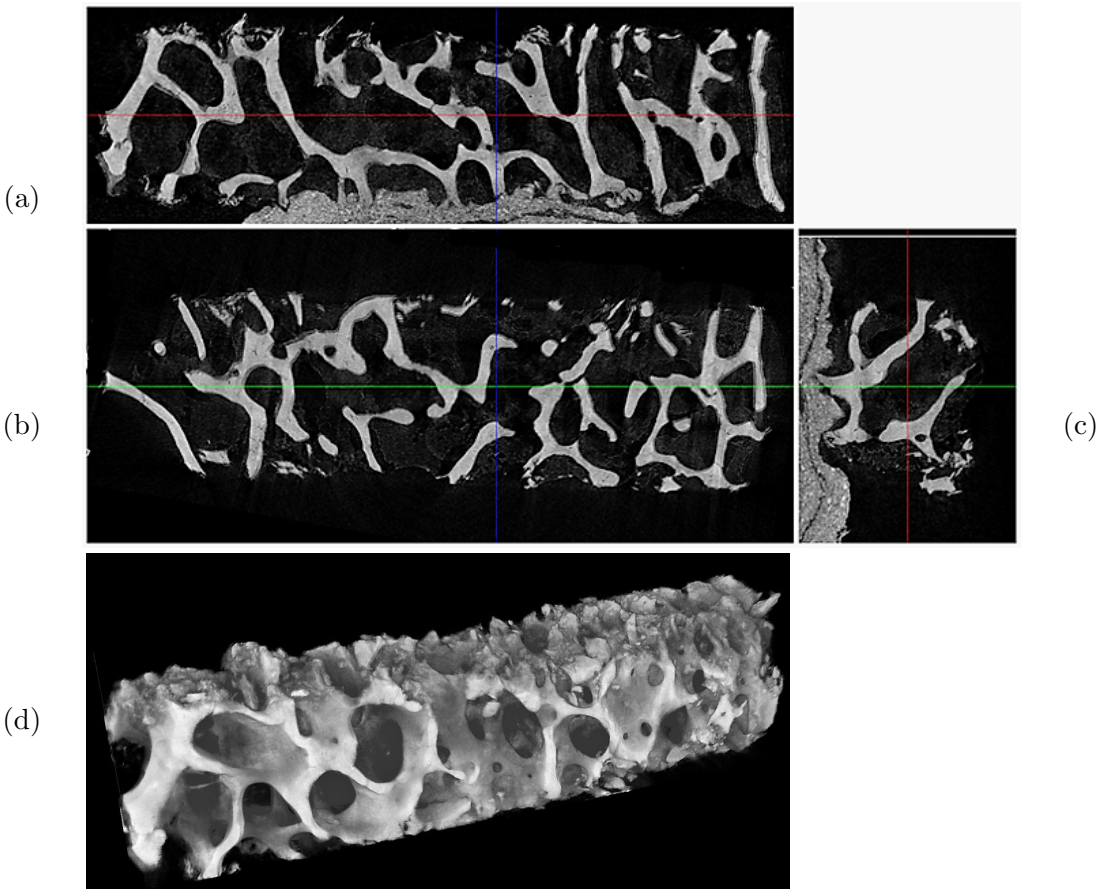

Figure 5.9: (a) Frontal (b) sagittal (c) transverse and (d) 3D representation of the μCT reconstruction of metaphyseal tissue recovered by Trephine needle

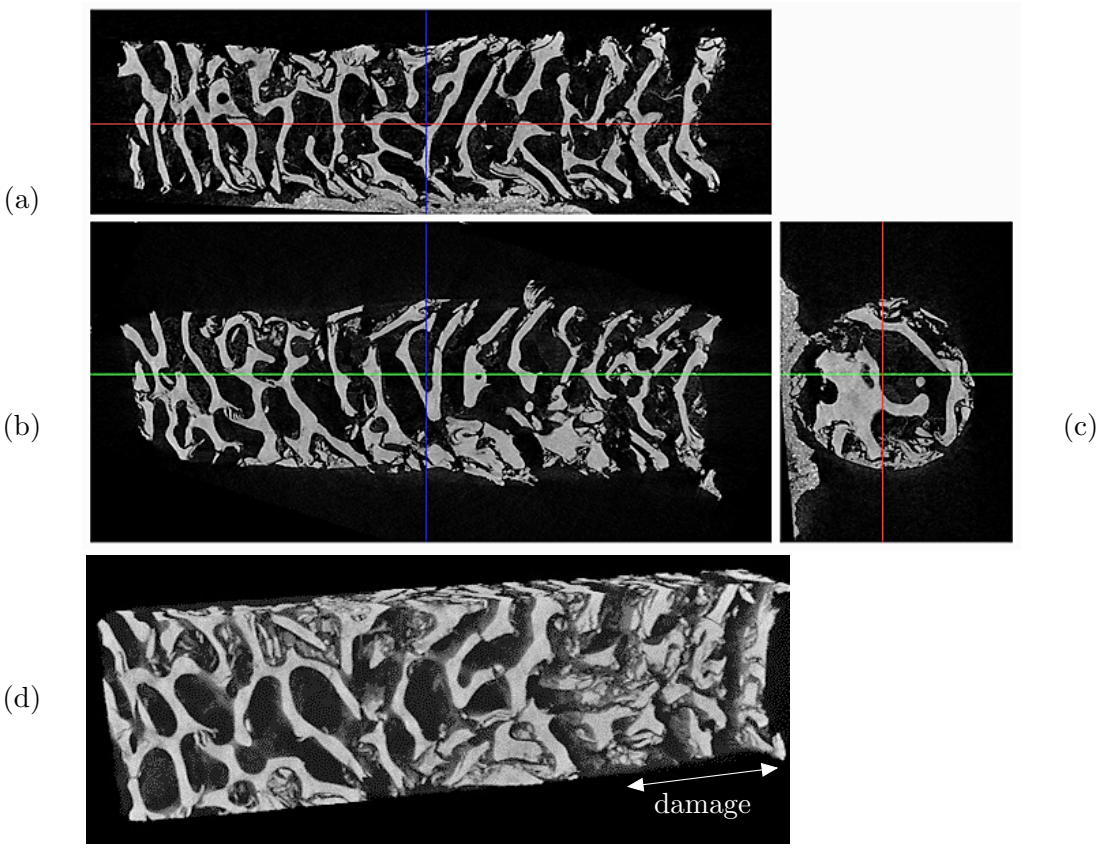

Figure 5.10: (a) Frontal (b) sagittal (c) transverse and (d) 3D representation of the μCT reconstruction of metaphyseal tissue recovered by USN2

5.2.2 Ovine cortical bone penetration

USN2 is then used to recover a cortical bone sample from the central diaphysis of an ovine femur, shown in Figure 5.11 (a). Cortical, or compact bone is much denser than trabecular bone and forms the bone's hard and strong outer exterior. Its strength makes it more difficult to penetrate and thus extract a sample from. The experimental protocol remained the same as for the ovine metaphyseal. Figure 5.11 shows an image of the penetration being conducted by the clinician partner. While both devices can retrieve a biopsy sample the trephine biopsy needle required the surgeon to apply a high force to the needle to penetrate the bone. This can be seen in Figure 5.11 (b) where the surgeon is gripping the clamp to generate the force required for the penetration while also applying a large torque with the needle penetrating in a cone-like orbit. This contrasted with USN2 which was held lightly while making a good positive contact with the bone during operation, as seen in Figure 5.11 (c). Consistent with previous penetration tests USN2 penetrated bone with just enough force to ensure a constant coupling between the needle tip and bone. A slow 120° twisting motion was also applied by

the surgeon to prevent the needle stalling.

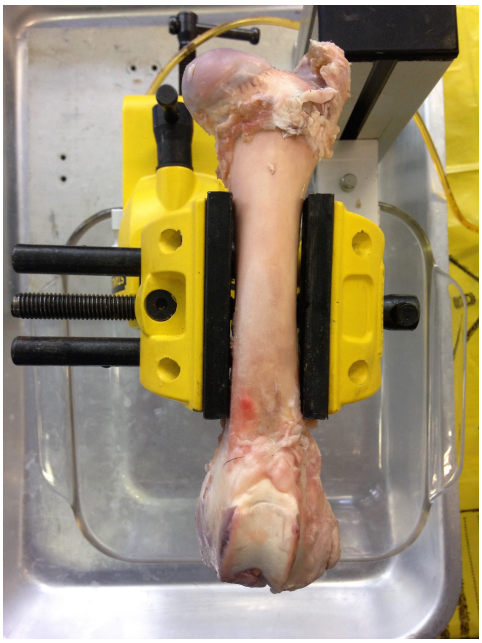

(a)

(b)

(c)

Figure 5.11: Ovine femur penetration (a) setup (b) with trephine needle (c) with USN2

Figures 5.12 (a) and (b) show the resulting penetration sites and extracted biopsies of cortical bone from the ovine femur using USN2 and a trephine needle.

A reconstructed μCT cross section of the sample extracted by USN2, shown in Figure

5.12 (c), presents a uniform cylindrical profile without visible micro-damaging on the surface indicating that the needle penetrated without subjecting the biopsy or hole walls to significant stress. However, the biopsy sample extracted using the trephine needle, also shown in Figure 5.12 (d) has been shortened and twisted, an indication of the high axial and shear stress applied by the surgeon during penetration. Maybe both samples form a viable biopsy for diagnosis, however the ultrasonic needle can extract a superior quality biopsy core from a challenging site.

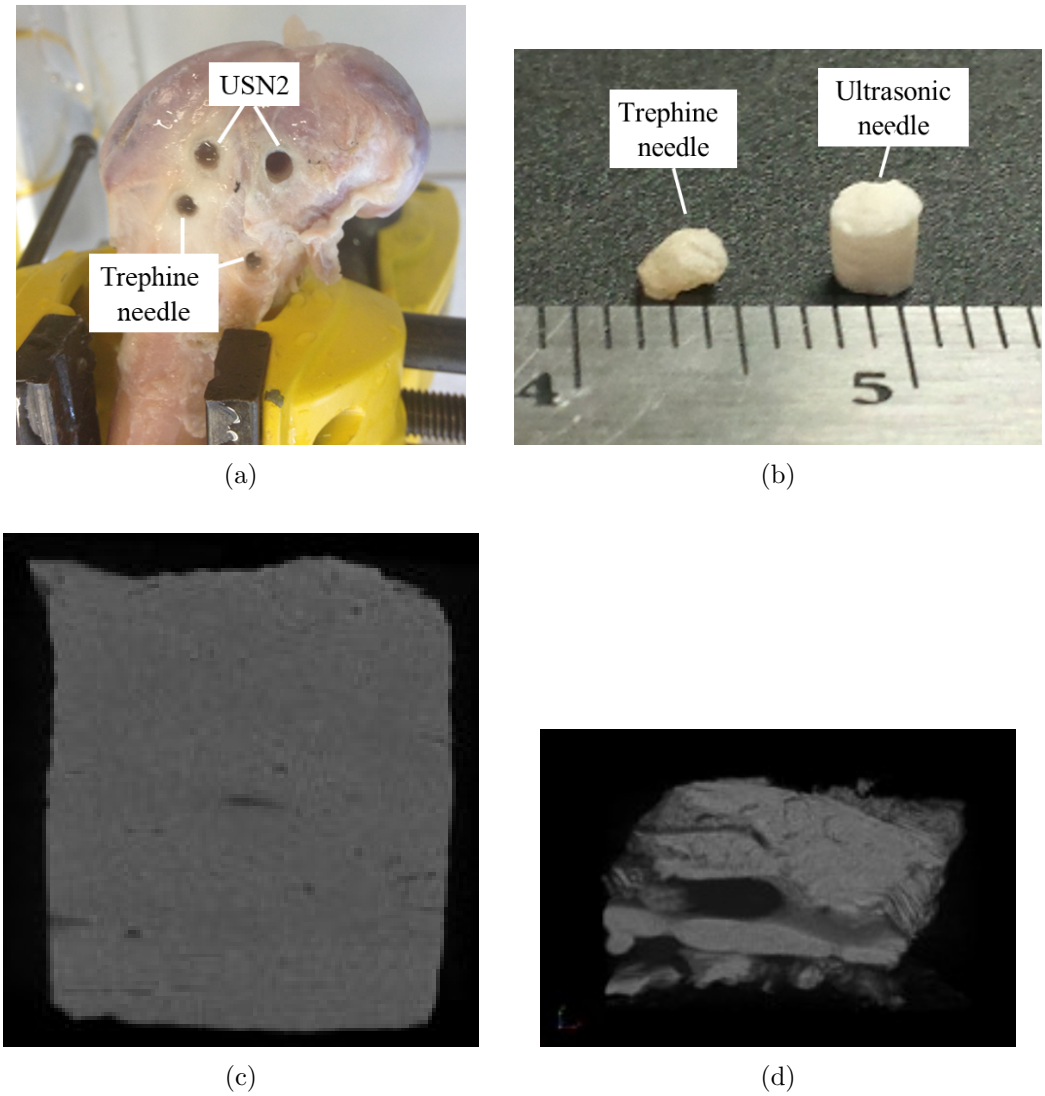

(a) (b)

(c) (d)

Figure 5.12: Ovine test (a) penetration sites (b) extracted biopsies of cortical bone, μCT reconstruction of biopsy recovered by (c) USN2, and (d) a trephine needle

A 3rd angle projection of a reconstructed μCT of the biopsy sample recovered from USN2 is presented in Figure 5.13. This presents sections through the sample; (a) is a section through the length of the sample, which corresponds to the green line, (b) gives a view through the

top of the sample, corresponding to the red line, while (c) corresponds to a section through the plane that the blue line lies on. The cylindrical shape of the sample and absence of surface micro-fractures indicates precision of the resonant needle, as does the intact bone canals seen in Figure 5.13 (b). A few bone fractures are visible and are indicated in Figure 5.13 (c). It can be noted that these cracks emanate from the sample surface and not from the internal bone canals implying that the penetration did not exert significant stress on the biopsy. This provides further evidence that the recovered sample could be viable biopsies for pathology.

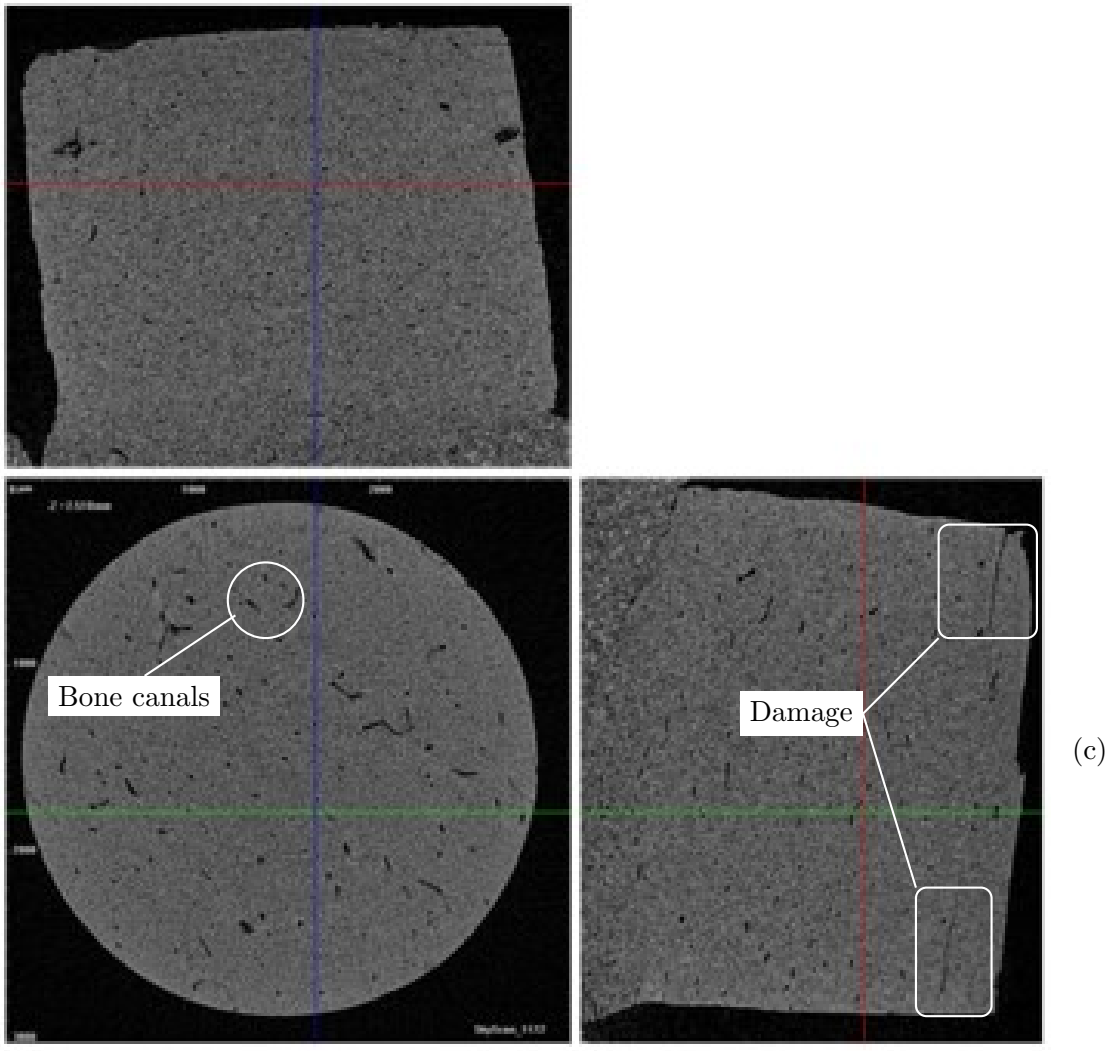

Figure 5.13: 3rd angle projection of the μCT image of the recovered biopsy

5.3 L-T composite mode needle, USNLT

The ability of an ultrasonic bone biopsy needle to penetrate challenging bone has been demonstrated. However, improvements are sought to increase the penetration speed and

reduce heating at the penetration site. The remainder of this chapter evaluates the generation of an L-T composite mode of the needle, the design of which is detailed in Chapter 3.

Experimental modal analysis is conducted to validate the modal parameters predicted using FEA for USNLT. The axial and tangential components of the needle tip displacement amplitude are then measured at the resonance frequency for a range of excitation levels to calculate the torsionality and investigate its dependence on excitation level. Initial penetration tests are carried out to compare the L–T mode needle USNLT with the L mode needle, USN3. Sawbones® is the bone mimic materials to allow direct comparison of the penetration time and record mechanical damage.

5.3.1 Characterisation of USN3 and USNLT

Figure 5.14 shows an image of the manufactured devices, USNLT and USN3. The design process of the L–T needle is detailed in Section 3.5. Helical cuts are introduced along the conical sections of the ultrasonic needle device based on parameters determined. Both needles have a sharp-tapered titanium tip.

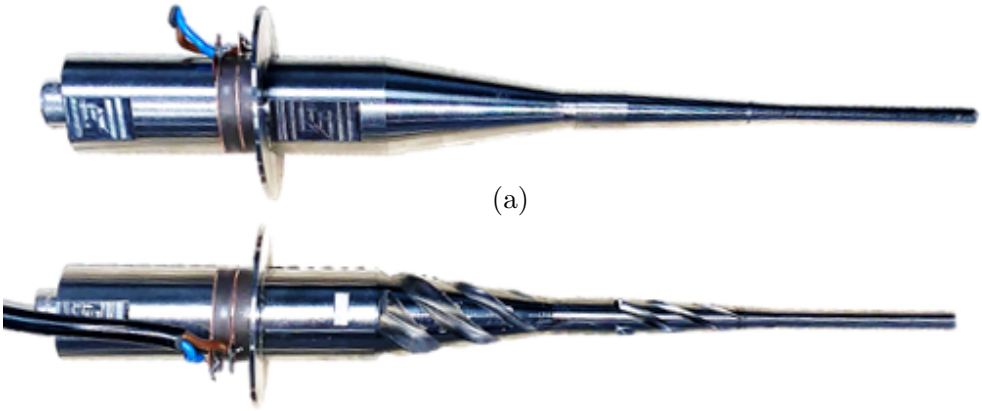

(a)

(b)

Figure 5.14: Ultrasonic biopsy needles (a) USN3, (b) USNLT

Experimental modal analysis

Figure 5.15 shows the FEA predictions and EMA measured mode for USNLT and USN3 desired mode of operation. As discussed in Section 4.2.5 the L mode device operates in resonance at 24.5 kHz with neighbouring modes B7 and B8. USNLT is resonant at 23.8 kHz, a 0.8% difference from the predicted value. The predicted neighbouring modes T3 and B8

modes could not be identified as peaks in the frequency responses, as the L-T mode dominated the response.

The nodal plane of the tuned frequency of USN3 represents the 2nd longitudinal mode of vibration. While the nodal plane of the L-T mode of USNLT combines the 2nd longitudinal mode and the 3rd torsional mode of vibration. The combination of modal coupling and degeneration of the longitudinal motion will aid in achieving torsionality at the needle tip that meets the design criteria.

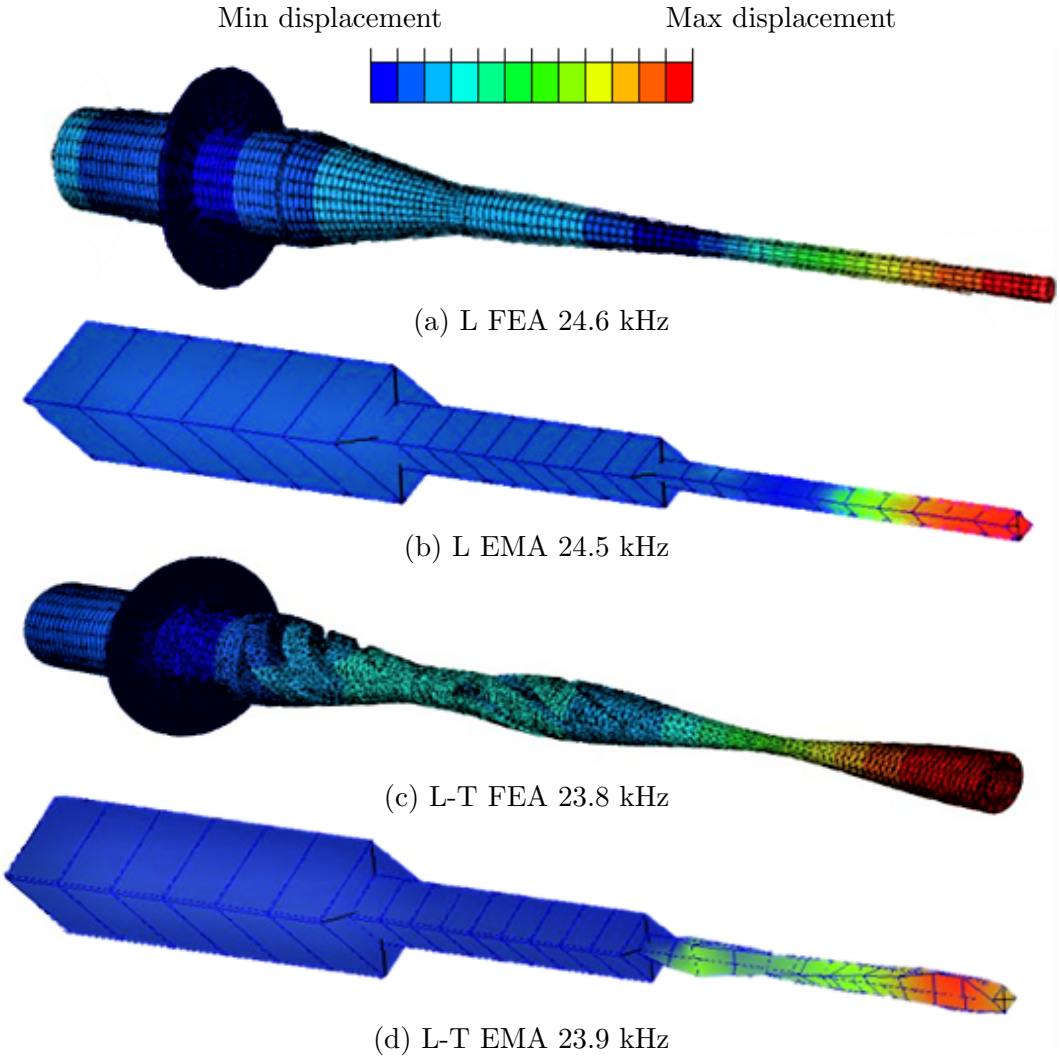

(a) L FEA 24.6 kHz

(b) L EMA 24.5 kHz

(c) L-T FEA 23.8 kHz

(d) L-T EMA 23.9 kHz

Figure 5.15: (a) FEA and (b) EMA of 2nd longitudinal mode of vibration and (c) FEA and (d) EMA of USNLT L–T mode of vibration

Validation through high excitation level

The tangential and longitudinal components of the displacement amplitude at the tip of USN3 and USNLT are measured using a 3D laser vibrometer (Polytec, 3D CLV) as shown in Figure 5.16. With USN3 and USNLT only differing physically in the addition of the helical cuts in USNLT, validation of the predicted torsionality is investigated and a direct comparison made of the axial component amplitude. The devices are excited under no-load conditions using the resonance tracking system and matching circuitry.

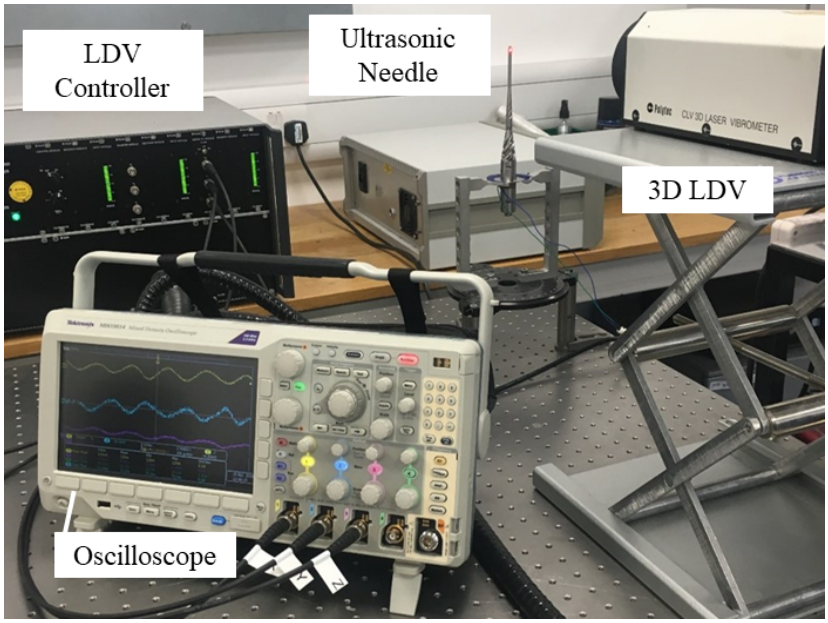

Figure 5.16: Measuring the vibration response at the needle tip using 3D LDV

Figure 5.17 (a) shows the axial and tangential components of displacement amplitude for incremented levels up to 34 V_{pp}. The longitudinal displacement of the USNLT is greater than that of USN3 across the range of excitation levels while also gaining an additional torsional response. Despite the name of the method used to generate an L-T motion being mode degeneration, suggesting that longitudinal vibration is sacrificed to attain a torsional mode, it is likely that the amplitude increase is due to reducing the mass of the front mass and needle insert. The torsionality of USNLT, shown in Figure 5.17 (b), across the range of excitation levels remains consistent between 0.59 and 0.62, considerably higher than the FEA estimation of 0.37. This response may be the result of the L-T mode coupling with T3 as suggested by the mode shapes from EMA.

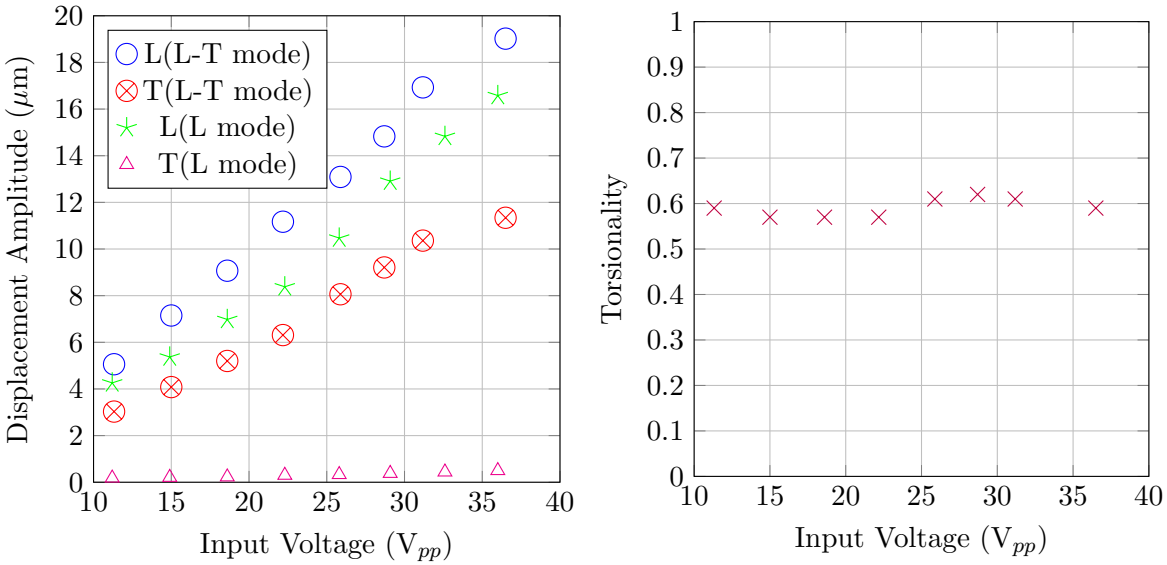

Figure 5.17: (a) Longitudinal (L) and tangential (T) displacement amplitude at tip of USN3 and USNLT, (b) Torsionality of USNLT

5.3.2 Harmonic analysis

Linear mathematical approximations of dynamic systems are commonly used to estimate the displacement of a system proportionate to the force applied. Although sometimes this may be sufficient, non-linearity affects the operation of ultrasonic surgical and other devices. The causes of non-linearities and characterisation techniques have been investigated to aid understanding of operation limits. Nonlinearity in ultrasonic transducers causes mechanical loss, frequency shifts, softening responses, amplitude jumps and the generation of harmonics. It is widely accepted that the causes of nonlinearity are structural configurations, and strain dependent material properties of the piezoceramic material.

Nonlinear dynamic responses can be identified by measuring vibration amplitude through a frequency sweep in a bandwidth containing the resonant frequency as in Figure 5.18. A linear response is symmetrical around the natural frequency. Non-linearities are characterised by asymmetrical bending of the response curve. At increasing excitation levels, the natural frequency either decreases referred to as softening, or increases referred to as hardening. Further non-linear behaviours such as the jump phenomena and associated hysteresis, where the response becomes unstable, can be characterised through changes in the response between an upward frequency sweep and downward frequency sweep [184–187].

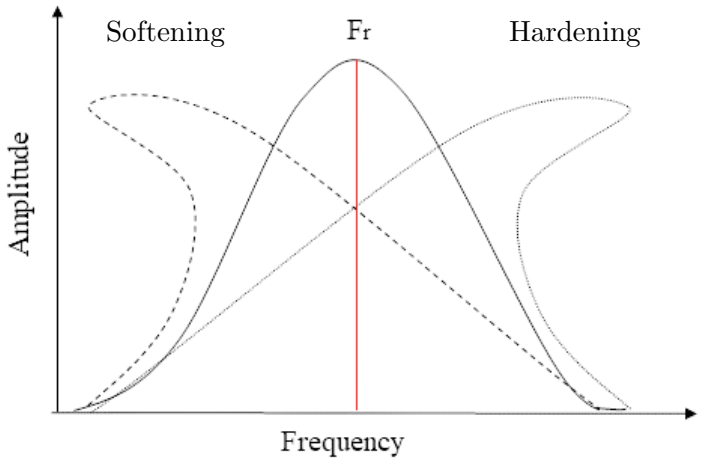

Figure 5.18: Characteristics suggesting nonlinearity in a frequency sweep

Previous research on nonlinear behaviour of ultrasonic devices used in bone surgery has investigated the influence of design features, such as the length, slenderness and location of the piezoceramic rings [184], for ultrasonic devices which vibrate with a longitudinal or longitudinal-flexural motion. The response of a longitudinal-torsional composite transducers has been captured previously [181]. However, an understanding of the effects of the helical cuts on the nonlinear response and new knowledge of the existence and effects of nonlinear torsional response and its influence on exciting a composite L-T modes is required.

Experimental setup

The experimental setup used to perform the nonlinear characterisation is shown in Figure 5.19. Two laser Doppler vibrometers, a 3D and a 1D are used to separately measure the axial and tangential displacement. The 1D LDV (Polytec, OFV 3001 with OFV 303 sensor head) is configured to measure the longitudinal vibration by directing the laser axially onto the needle tip illustrated in Figure 5.20. The 3D LDV (Polytec, 3D CLV) is configured to measure the radial response close to the needle tip to capture the tangential displacement. LabVIEW software is used to control the excitation signal produced by the function generator (Agilent technologies, 33220A) which is then passed through an amplifier (Nanjing Foneng, HFVA-62).

Harmonic characterisation involves performing narrow bi-directional frequency sweeps through the resonant frequency at incremented excitation levels. The resolution of the

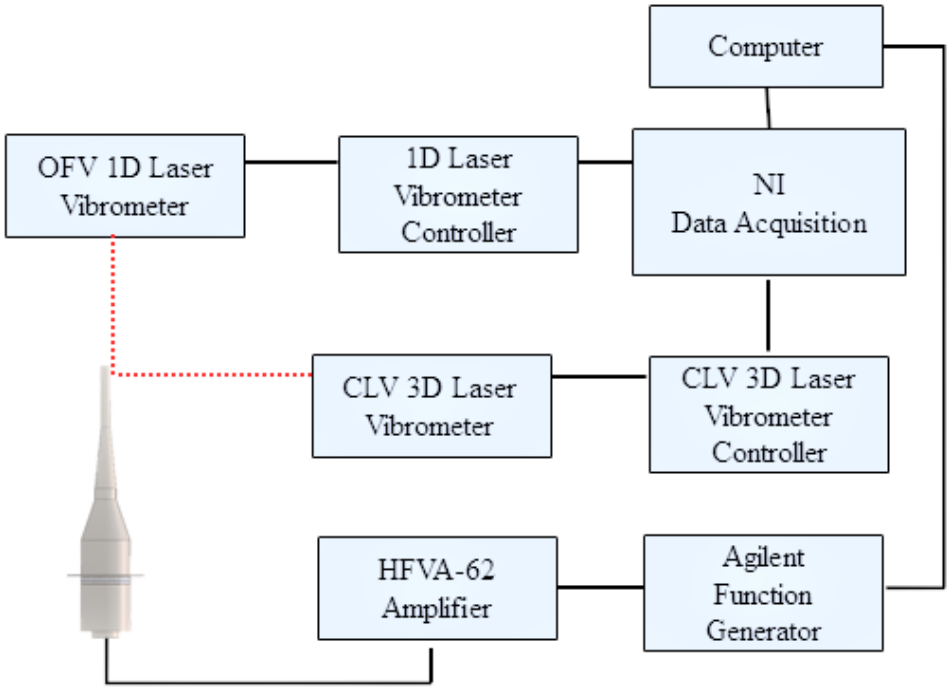

Figure 5.19: Set-up for harmonic analysis of USN3 and USNLT

frequency sweep must be sufficient to capture any evidence of jump phenomena due to a nonlinear response. Sinusoidal excitation of the ultrasonic transducer is performed using a burst signal of a finite number of cycles. The length of the burst signal is selected to allow the transducer to reach steady state. A time delay between bursts is introduced to minimise temperature increases within the transducer.

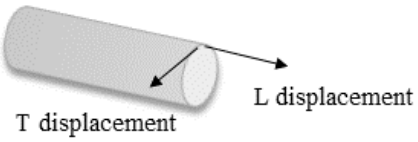

Figure 5.20: Measuring the longitudinal and tangential response at the needle tip

Harmonic analysis of USN3 and USNLT

For all measurements the frequency resolution is 5 Hz and the frequency sweep is 23.5 to 24.5 kHz for USNLT and 24.2 to 25.2 kHz for USN3. Excitation level is controlled by the voltage which is incremented from 6 to 132 V_{pp}. The results of all the harmonic analysis are presented in Figures 5.21 and 5.22.

The results show behaviour typical of power ultrasonic devices. Stiffness softening is observed in the responses, exhibited by decreasing resonant frequency with increasing excitation levels. The longitudinal and torsional responses of USNLT suffered from similar reductions in the resonant frequency for increasing excitations from 6 to 132 V_{pp}. Above 66 V_{pp} it is observed that both the L and T response displayed hysteretic response regions. The width of these regions became significant, 30 Hz and 40 Hz for 110 V_{pp} and 132_{pp}. Similarity in the softening response for the longitudinal and torsional vibration suggest that the difference between the axial and torsional stiffness does not significantly affect the nonlinear response.

USN3 suffered from tuned frequency reduction similar to that exhibited by USNLT. For an excitation of 132 V_{pp}, USN3 and USNLT suffered from a reduction in frequency from the tuned resonant frequency of 350 Hz and 275 Hz. For USN3, hysteretic response regions can be observed above 66 V_{pp} with regions of significance apparent for the highest excitation levels. The results suggest that geometric changes to the device, carving deep helical cuts to degenerate the longitudinal mode does not affect the nonlinear response. This is despite significant changes to the axial and tranverse stiffnesses and the mass of the device.

The peak displacement amplitudes for USN3 and USNLT for the incremented excitation voltages is displayed in Figure 5.23. Across the range of excitations USNLT excited a larger L response than USN3. This can be accredited to the reduction in mass caused by the helical cuts, decreasing material losses and encouraging more energy from the piezoceramic rings forward to the tip of the device. A torsionality of 0.65 was exhibited, higher than the FEA predictions, accredited to the combination of coupling and degeneration to induce the L-T

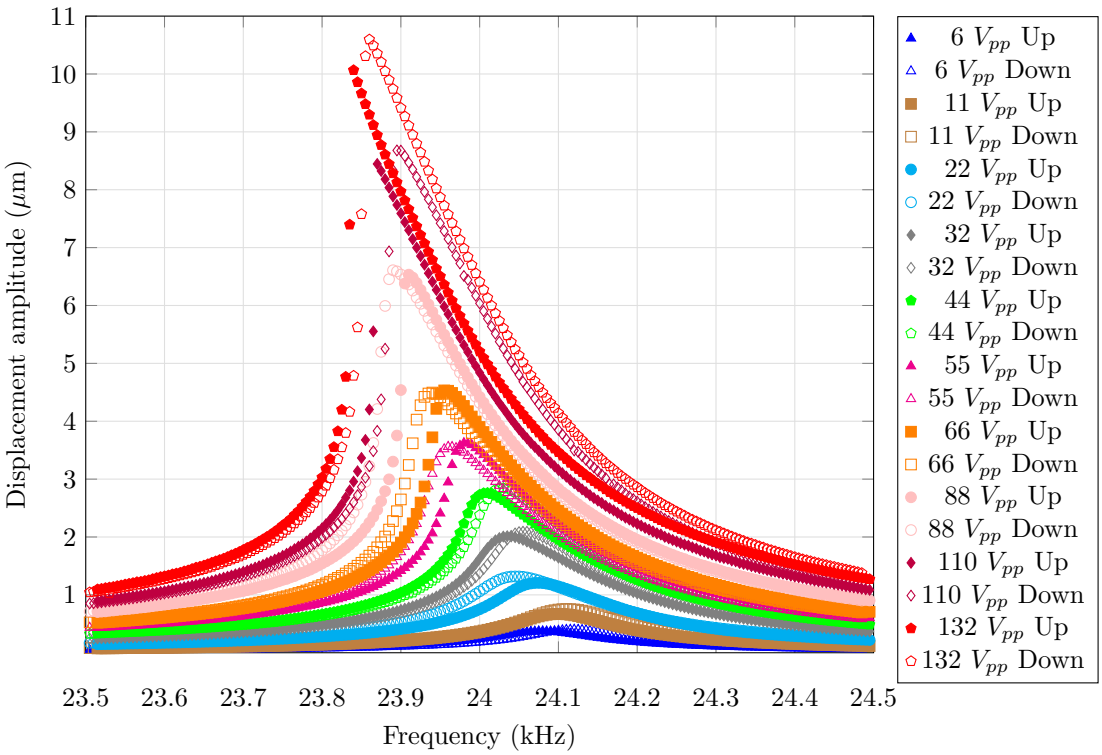

(a) Longitudinal response of USNLT

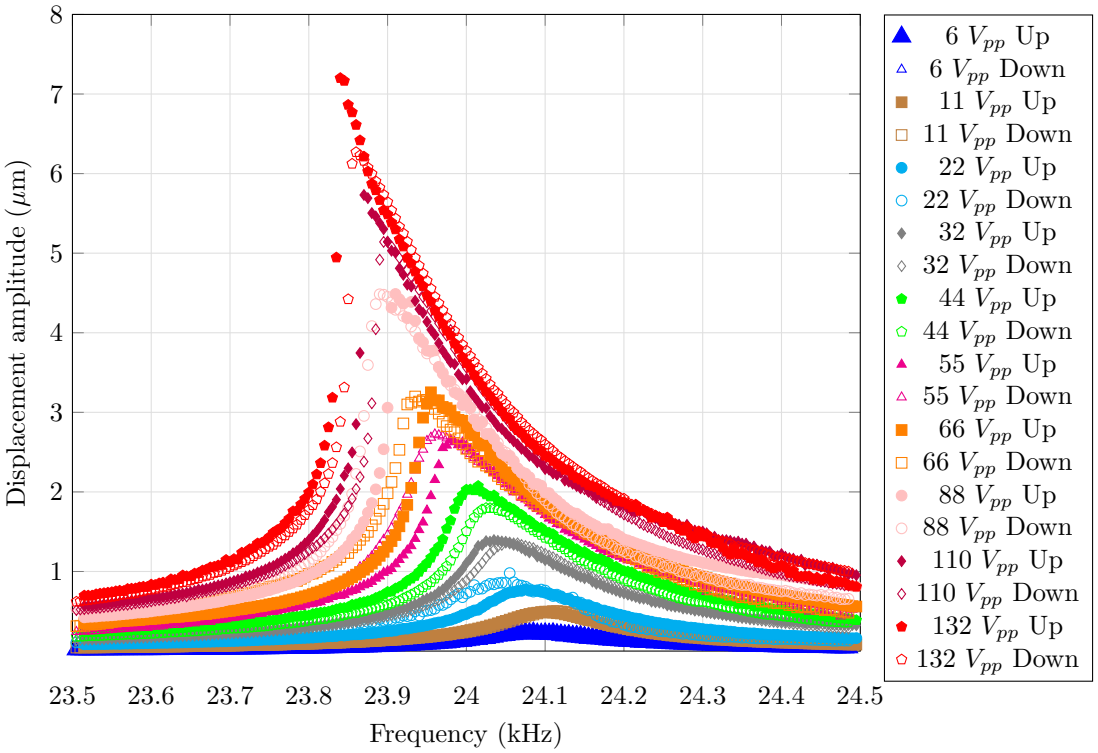

(b) Torsional response of USNLT

Figure 5.21: Harmonic analysis of USNLT

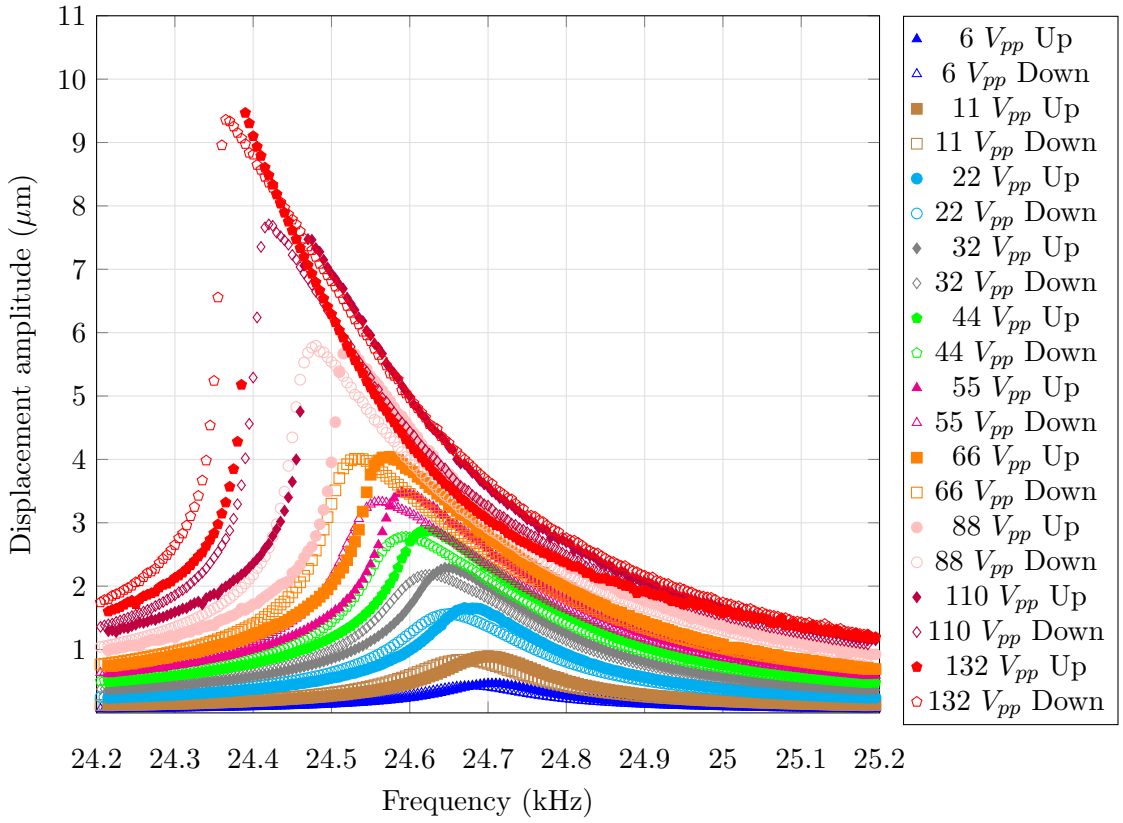

Figure 5.22: Harmonic analysis of USN3

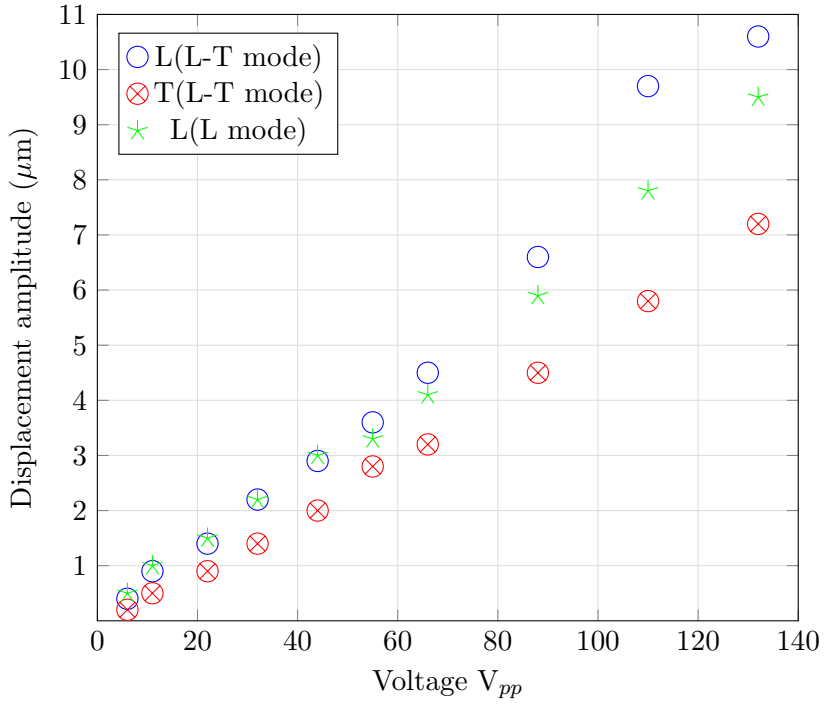

Figure 5.23: Peak displacement amplitude for increments of excitation voltage

5.3.3 Penetration tests: Sawbones®

Penetration tests are carried out to compare the penetration of USN3 and USNLT. The devices are driven by the resonance tracking system for penetration tests into the bone mimic material Sawbones®, PCF 20. USNLT penetrated 5 mm in 38 s, while USN3 penetrated 5 mm in 52 s. USN3 stalled in the Sawbones® sample unless the operator added a slow backward and forward rotation of the device. It was then possible to fully breach the back wall of the sample. Some charring around the hole and damage on the rear penetrating wall of the sample could be seen in Figure 5.24. USNLT penetrated without stalling, requiring no rotation motion by the operator. The penetration site is circular with considerably less micro-damage.

X-Ray computer tomography μCT is performed to evaluate the mechanical damage of the penetration sites. An X-ray microscope (Bruker, Skyscan 1172) with a megapixel camera (SHT 11) and an 80 kV source (Kamatsu) is used to attain 1800 images taken around one full 360° rotation of the sample. The images are reconstructed using Bruker's micro-CT volume rendering software. The μCT reconstruction (Figure 5.25), shows the resulting hole of USN3 is larger than that of USNLT perhaps from the rotatory motion performed by the operator. This suggests that using a composite mode of vibration could simplify the procedure, produce a smaller penetration hole with higher precision due to the removal of manual rotation.

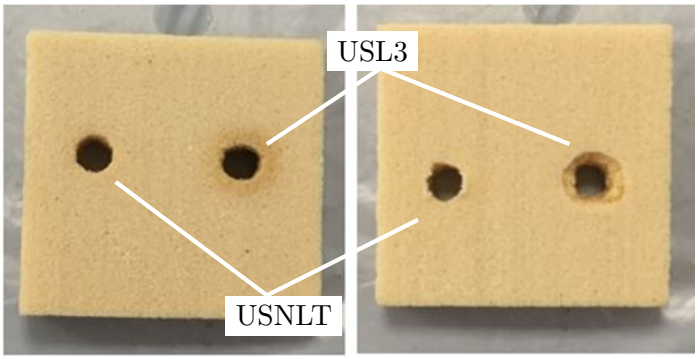

Figure 5.24: Sawbone sites, front (left) and back (right)

5.3.4 Penetration test: Ovine cortical

The capability of USNLT is further assessed by penetrating a segment of ovine femur shown in Figure 5.26. During the experiments both USNLT and USN3 penetrated cortical bone with the resulting sites shown in Figure 5.26(b). For both devices a very low force is supplied

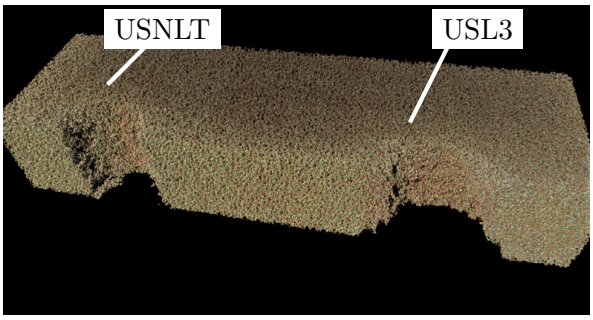

Figure 5.25: μCT representation of section through Sawbones® sample

by the operator, just enough to ensure a good contact between the needle and the subject. A rotation applied by the operator was required for USN3 but not for the USNLT device. USNLT created a circular hole while USN3 resulted in a wider, more irregular shaped hope. It can be assumed this is due to the additional manual 180° slow rotation required to prevent stalling and assist progress of the penetration. USNLT also retrieved an intact core sample of bone which broke away during the penetration which would be viable for clinical analysis.

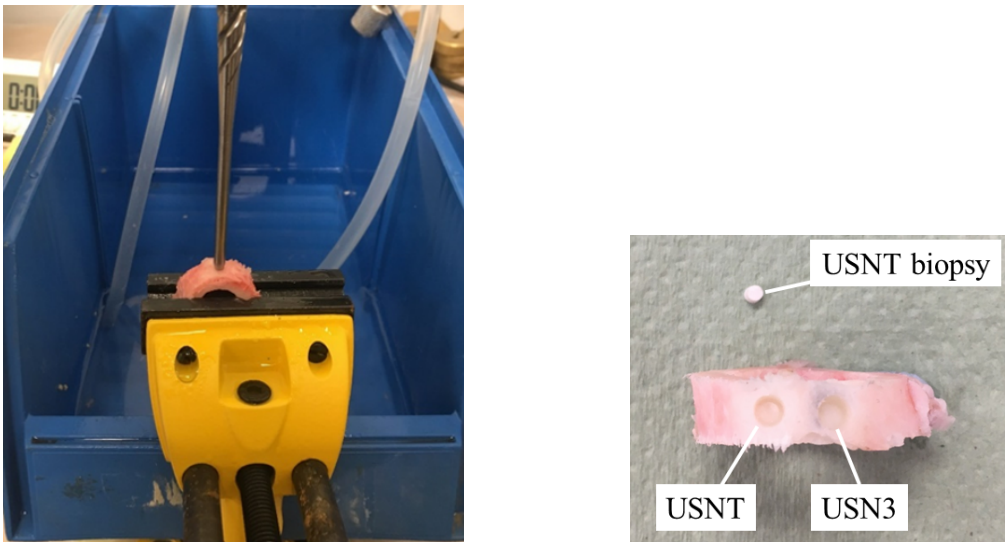

(a) (b)

Figure 5.26: Ovine femur (a) experimental set up (b) penetration sites and USNLT biopsy

The X-ray μCT 3D reconstruction of the penetration sites and a section through the biopsy retrieved by USNLT is shown in Figure 5.27 (a) and (b) respectively. The direction of striations around the penetration site for the USNLT of the radial motion, emanates out from the penetration site. While the striation around the penetration site of USN3 micro-damage, radiates down the wall of the hole.

The μCT reconstruction of the bone biopsy sample in Figure 5.27(b) shows little micro-cracking. However, the recovered biopsy has been compacted towards the bottom of the sample. This is due to the sample being jammed into the inner cavity of the needle during the procedure. Despite this, the sample's architecture remained intact suggesting it would be viable for clinical analysis.

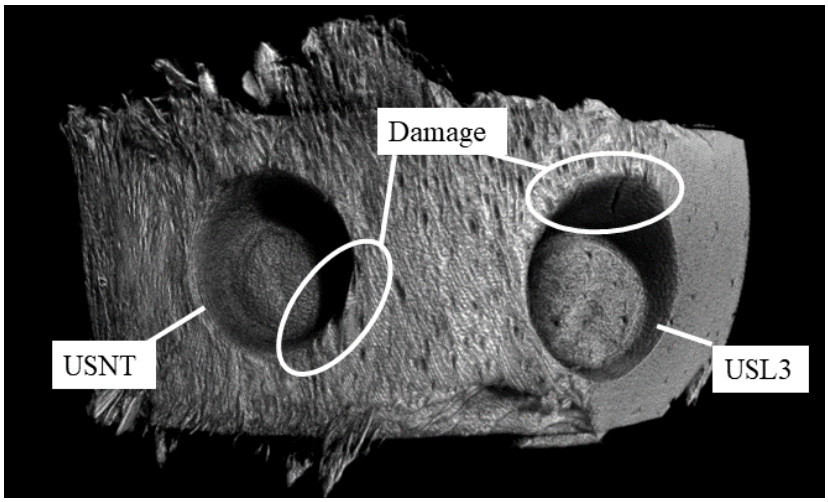

(a)

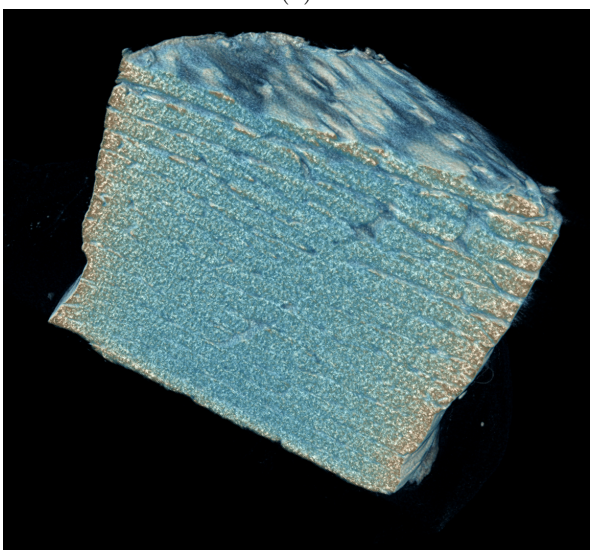

(b)

Figure 5.27: 3D μCT reconstruction of (a) penetration sites and (b) biopsy sample

Figure 5.28 shows a μCT of a section of the biopsy retrieved by USNLT depicts the layers of the cortical bone. The layers at the bottom are closely compacted relative to the layers at the top. This indicates the sample being wedged within the hollow needle tip during retrieval. However, the resulting architecture would not affect the quality and viability for analysis.The 3rd angle projections of the penetration site shown in Figure 5.29 provide further insight into

the damage caused by the procedure. The colour profile is based on the relative attenuation of the X-Rays at that point; however, these are not mutually calibrated for USN3 and USNLT therefore can only provide a depiction of the density of that bone section. The profile of the wall of the USN3 hole is angled due to the manual motion required by the operator to aid progress of the needle. The site possessed little cracking compared to the site of the USNLT needle. Mechanical cracking could be seen at the base of the USNLT site caused by the biopsy breaking away from the sample.

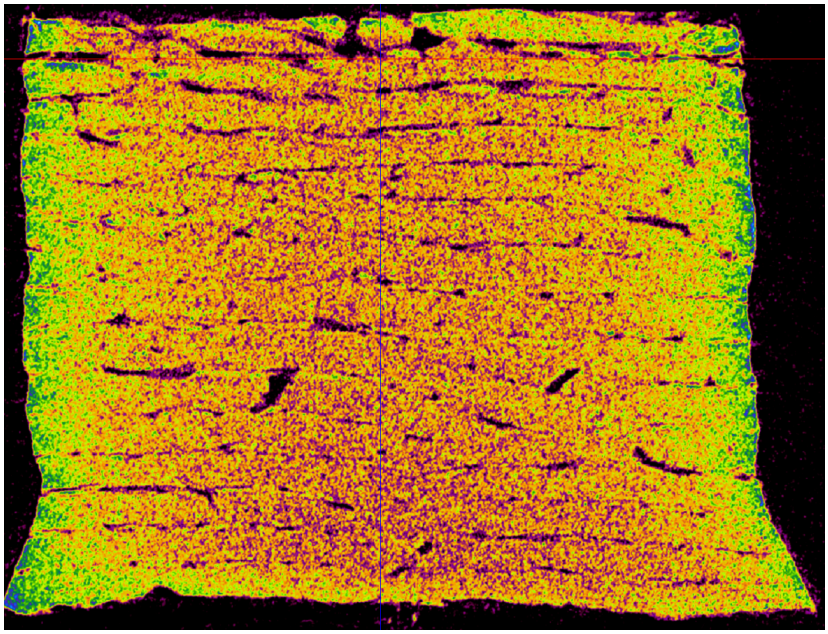

Figure 5.28: μCT of biopsy extract by USNLT

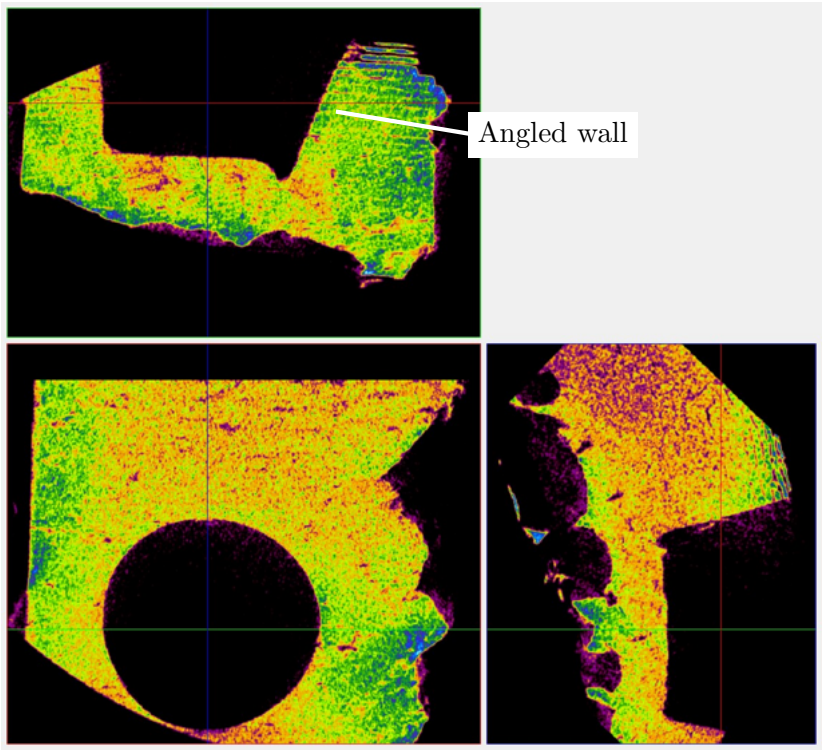

(a)

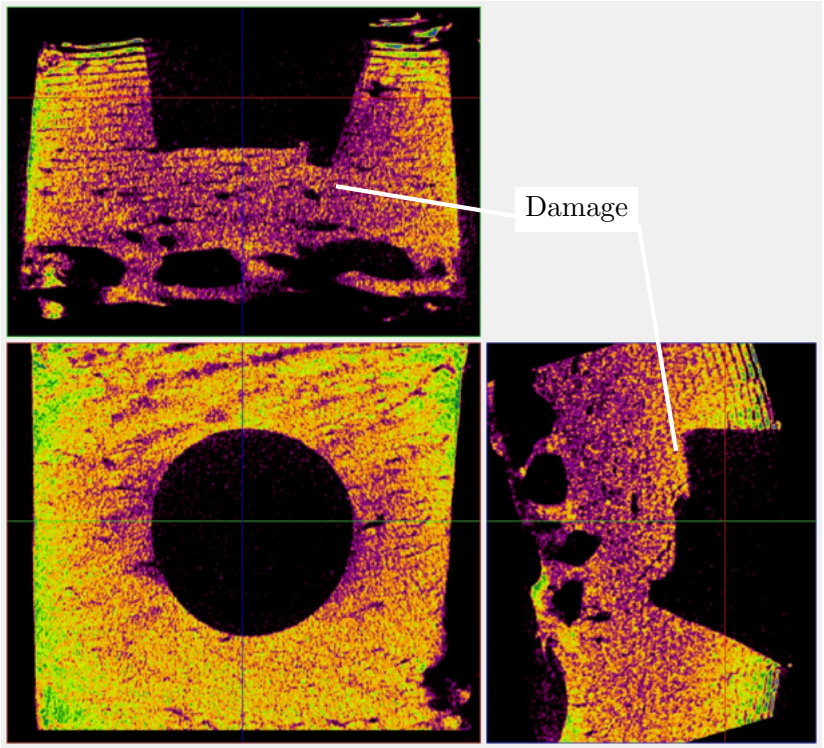

(b)

Figure 5.29: 3rd angle projections of μCT of the penetration sites (a) USN3 and (b) USNLT

5.4 Chapter conclusion

Evaluation of the different needle devices is presented in this chapter. Multiple longitudinal mode devices are used to penetrate bone mimic and animal bone samples. Evaluation of USN1 is achieved by penetrating Wistar rat femur, using μCT to evaluate the resulting damage inflicted on the site. The penetration site presented minimal damage, only minor instances of cracking with much of the micro-architecture intact. USN2 penetrated the metaphysis and cortical of ovine femur. The core bone biopsy retrieved from the cortical bone was geometrically cylindrical, architecturally intact and smoother when compared with a biopsy obtained using a trephine biopsy needle. Although possible that both samples are viable biopsies for diagnosis, the ultrasonic needle can extract a biopsy core of superior quality .

The characterisation of USNLT through EMA corresponded well with the values predicted through FEA. The modal shape of the L-T mode suggests that the 2nd longitudinal mode couples with the 3rd longitudinal mode of vibration, increasing the torsion at the tip of the needle. Nonlinearity exhibited by USN3 and USNLT were comparable, similar downward frequency drifts with increasing excitation level, indicating a softening nonlinear response. The frequency drift of the L displacement and T displacement were also comparable suggesting that differences in the axial and tangential stiffness does not significantly affect the nonlinear response. This is corroborated by the similarities in the nonlinear responses of USN3 and USNLT.

USNLT and USN3 are used to penetrate Sawbones® and ovine cortical. USNLT penetrated bone mimics without the operator superimposing a slow rotation onto the device. This resulted in a smoother, more precise penetration and prevented stalling. When used to penetrate ovine cortical the resulting striation around the site of penetration differed for each device. The angle of the penetration site for USNLT was easier to control, resulting in a more geometrically cylindrical hole.

USN1	EMA	EMA validated the FEA predictions with an error of 2.1% for bending modes, B8 and B9 and 0.8% for L2. B8, L2 and B9 were measured at 22.8 kHz, 25.7 kHz and 27.7kHz respectively.
	Sawbones	A smooth 50 mm penetration in Sawbone with a PCF 10 is achieved with little force required beyond self-weight and no signs of charring.
	Rat bone	The femur bone of a 3 month old Wistar rat is penetrated with only sufficient force to maintain good contact, with a slow 120° motion. μ-CT revealed a irregular shaped hole without large cracks.
USN2	EMA	EMA identified the resonant frequency of the 2nd longitudinal mode at 23.5 kHz, the 8th and 9th bending modes at 20.8 kHz and 24.5 kHz, with errors of 0.8%, 2.1% and 1.8% respectively from the FEA predictions.
	Ovine metaphyseal	USN2 successfully penetrated the ovine metaphysis bone and extracted an intact and viable biopsy sample for analysis.
	Ovine cortical	The needle penetrated through ovine cortical and extracted a uniform cylindrical biopsy without visible micro-damaging on the surface indicating that the penetration did not subject the biopsy or hole walls to significant stress.
USN3 and USNLT	EMA	Strong correlation between the FEA predictions and EMA measured modes for both USNLT and USN3 was found. A combination of modal coupling and degeneration aids in achieving torsionality at the needle tip.
	Harmonic analysis	Comparable stiffness softening, typical of power ultrasonic devices, is observed in the responses of both devices. This suggests that the geometric changes to generate an L-T response does not affect the nonlinear response.
	Sawbones	Both USN3 and USNLT required low force to penetrate through Sawbone. USNLT created a more uniform circular hole as no manual rotation is required to prevent stalling and assist progress of the penetration.
	Ovine cortical	Longitudinal-torsional motion resulted in a more circular penetration site and simplified the procedure by removing the requirement for manual rotation of the needle. USNLT also retrieved an intact core sample of bone while USN3 did not.

Table 5.1: Summary of evaluation procedures performed

Chapter 6

Case study: Surgery of the petrous apex

In this chapter, the needle is further developed as a device that fits the need of a specialised application - the surgical treatment of the petrous apex. The petrous apex is in the centre of the head, close to the ear, shown in Figure 6.1. The bone is one of the most difficult to penetrate and requires sample recovery from one of the most inaccessible areas of the skull. The petrous apex can have lesions and tumours, the most common being schwannomas, meningiomas and epidermoid cysts. This work is a collaboration with a consultant ENT and skull base surgeon.

Accessing the petrous apex to obtain biopsies of relevant pathologies requires an extended

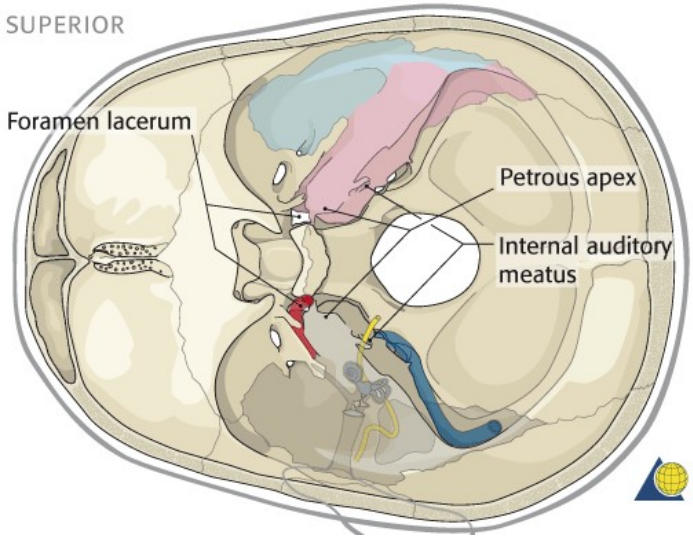

Figure 6.1: Location of the petrous apex in the skull [188]

surgical intervention usually related to significant morbidity. Biopsies of the petrous apex are achieved through an open approach, typically utilising power drills operating at 50,000-80,000 rpm with saline irrigation and manual suction. The procedure takes several hours (up to 12 hours is common) as precision is required while drilling around delicate structures. The procedure can affect the patients' hearing, balance and even the facial nerve function. Additionally, the several hours of general anaesthesia involved comes with its own risks, particularly in older patients. This typically results in diagnosis and management being achieved through magnetic resonance imaging.

Accessing pathologies of the lateral skull base and the petrous apex through a safe and minimally invasive technique aims to reduce potential morbidity and facilitate accurate diagnosis and tailored treatment. An ultrasonic, navigated biopsy needle has the potential to access lesions deep in the bone, improving how such pathologies are managed and thus patient outcomes. Previous chapters of this thesis have discussed how a low force is required, just sufficient to physically couple the ultrasonic device to the bone and make a forward progression of the needle. The ultrasonic needle would be a single device used to perform the procedure which has the potential of increased precision, reduced sample damage, reduced injury to surrounding tissue, improved patient outcomes and, importantly, improved diagnosis.

In collaboration with an ENT surgeon, several design requirements are identified including adjusting the length of the needle insert, increasing the vibrational amplitude, incorporation of irrigation and surgical navigation. To evaluate the devices an application specific test environment is created. Feedback from initial penetration tests conducted with the physician highlighting key areas of interest which should be investigated further.

When surveying the available surgical devices it was clear that published guidelines regarding transducer design do not reflect the devices on the market. For the needle to be commercially successful an investigation into key features is required. One key feature is the number of pairs of piezoceramic rings incorporated. In Chapter 3 Abaqus FEA is used to predict how the volume of ceramics affects the vibrational response of the device. Experimental validation of an altered version of USNLT is detailed in this chapter.

6.1 Test environment: The Phacon navigator

The aim is to develop an ultrasonic needle device which will combine safe and low force penetration and sample recovery, through real-time surgical navigation. Lab evaluation of the ultrasonic devices is sought using a surgical mock-up of the petrous apex procedure. The Phacon temporal bone trainer is a bench top surgical navigation system coupled with advanced and realistic 3D printed skull models.

The Phacon Temporal bone trainer is a modular navigation system for surgical training used with ENT models based on the CT scans of real patients. The system shown in Figure 6.2 consists of a navigation camera, instrument tracker, head, bone patient 'Schmidt' and a laptop. The navigation software provides visual and tactile feedback through sensors. The bone insert "Schmidt" has tubing incorporated so the system can detect if the surgical instrument has contacted a critical anatomical structure such as the dura mater. The system also tracks the duration of the simulation, the type of structure damaged and the number of contacts, all of which can be viewed and statistically evaluated.

Figure 6.2: The Phacon navigator [189]

6.1.1 Penetration tests

USNLT is used to perform penetration tests on the temporal bone skull model, Schmidt. The tests are performed by the consultant ENT surgeon, demonstrating the location and direction of the penetration through the mastoid bone and angle of attack in Figure 6.3 (a).

The device successfully penetrated the cortical of the mastoid bone before continuing through the trabeculae as illustrated in Figure 6.3 (b) and (c).

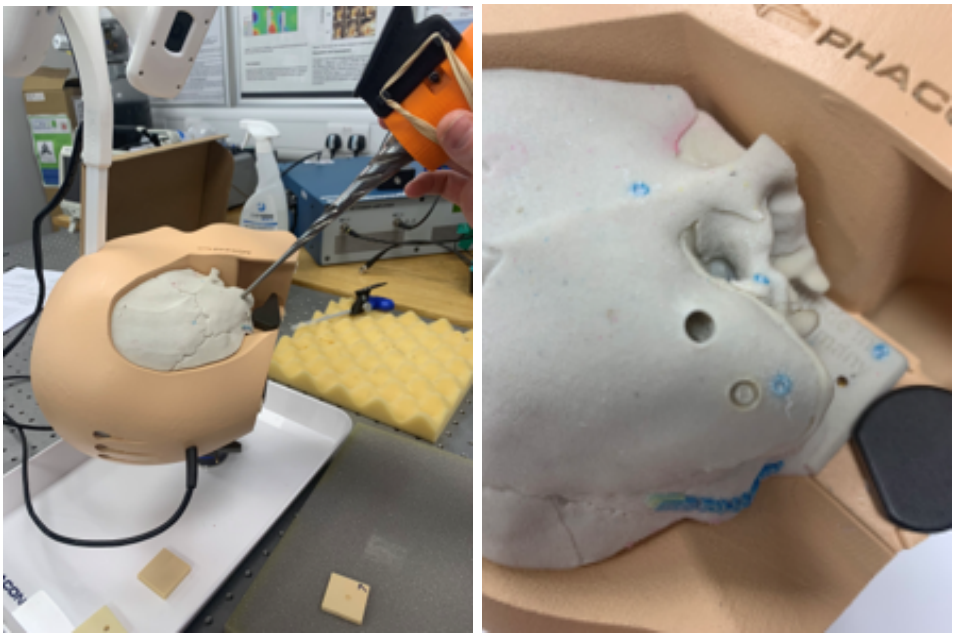

(a) (b)

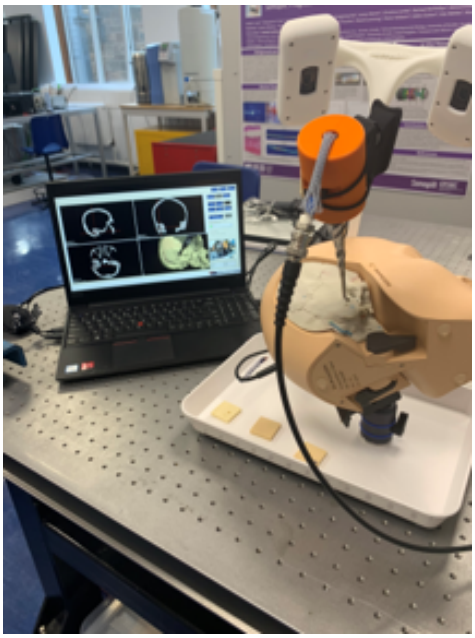

(c)

Figure 6.3: Schmidt petrous apex penetration (a) angle of penetration (b) resulting site and (c) final placement

During the procedure the consultant can monitor the location of the needle tip on the graphical user interface. Figure 6.4 depicts screenshots captured with the needle insert at its deepest location. Cross-sections are provided in Figure 6.4(a), (b) and (c) depicting the x, y

and z axis views respectively, with red crosshairs representing the location of the needle tip. Figure 6.4 (d) provides a 3D representation with the opacity of the bone reduced to view the needle tip location with respect to vascular structures (yellow and purple) and dura mater (pink).

Penetration of the cortical bone is achieved, however the time of penetration of the cortical layer of bone is longer than desired. To access the petrous apex the surgeon would penetrate through the cortical of the mastoid which varies in thickness across its surface. The dense, thick cortical bone proved difficult to penetrate at locations of increased thickness, slowing progress and causing heat build-up at the site. On reaching the cancellous bone, penetration is quick and the petrous apex is easily accessed. The remainder of this chapter will investigate managing of the temperature rise at the site through irrigation and increasing the vibrational response of the device by adapting the transducer design.

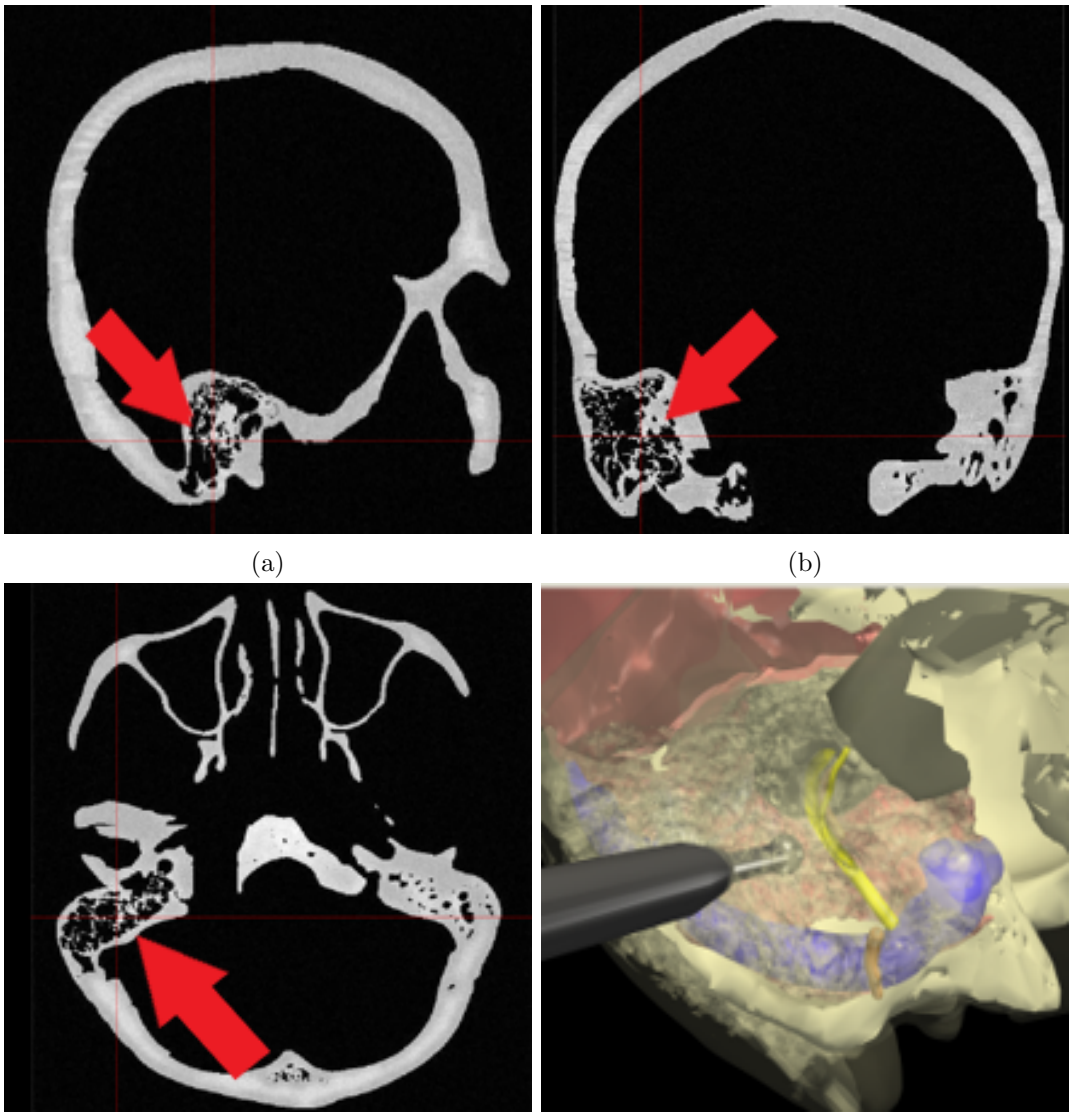

(a) (b)

(c) (d)

Figure 6.4: (a) X view (b) Y view (c) Z View (d) 3D representation from GUI of the Phacon system

6.2 Temperature at the site

A concern of high power ultrasonic devices is irreversible thermal damage in biological tissue which occurs if a temperature threshold is reached. It is widely accepted that thermal necrosis or cell death occurs when bone tissue is subjected to 47 °C for 1 minute [106]. In Chapter 4 power modulation was proposed to address temperature rises and investigated the effect duty cycle had on the temperature and penetration speed with Sawbones®. During a follow-up session with the ENT surgeon the needle USNLT is used to penetrate ovine skull and irrigation was proposed as a potential cooling technique.

The experimental set up shown in Figure 6.5 to monitor the temperature at the site uses type K thermocouples (RS Components Ltd, UK). USNLT was used to penetrate a thick section of cortical bone without irrigation for a period of around 11 minutes. The penetration then continued with a flow of room temperature water supplied at 20ml/min.

Figure 6.6 shows the temperature recorded by thermocouple A located approximately 10 mm from the site. During the period of no irrigation the temperature gradually increases from room temperature 23.8 °C to 69 °C, an average increase of 4 °C per minute. Necrosis of the bone tissue would have occurred after 6 minutes of driving.

Instantaneous with irrigation being applied the temperature dropped to 25.6 °C, 1.8 °C higher than room temperature and does not fluctuate. This is 20 °C below the threshold of necrosis and suggests that thermal damage is preventable solely through irrigation.

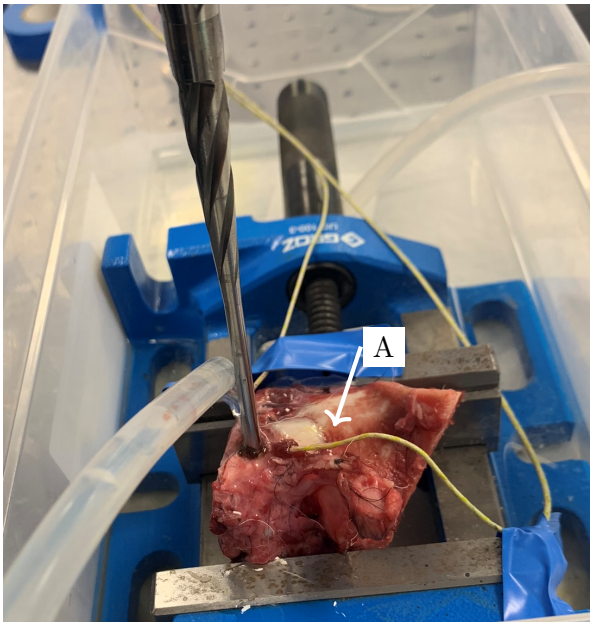

Figure 6.5: Experimental set-up to monitor the temperature during penetration

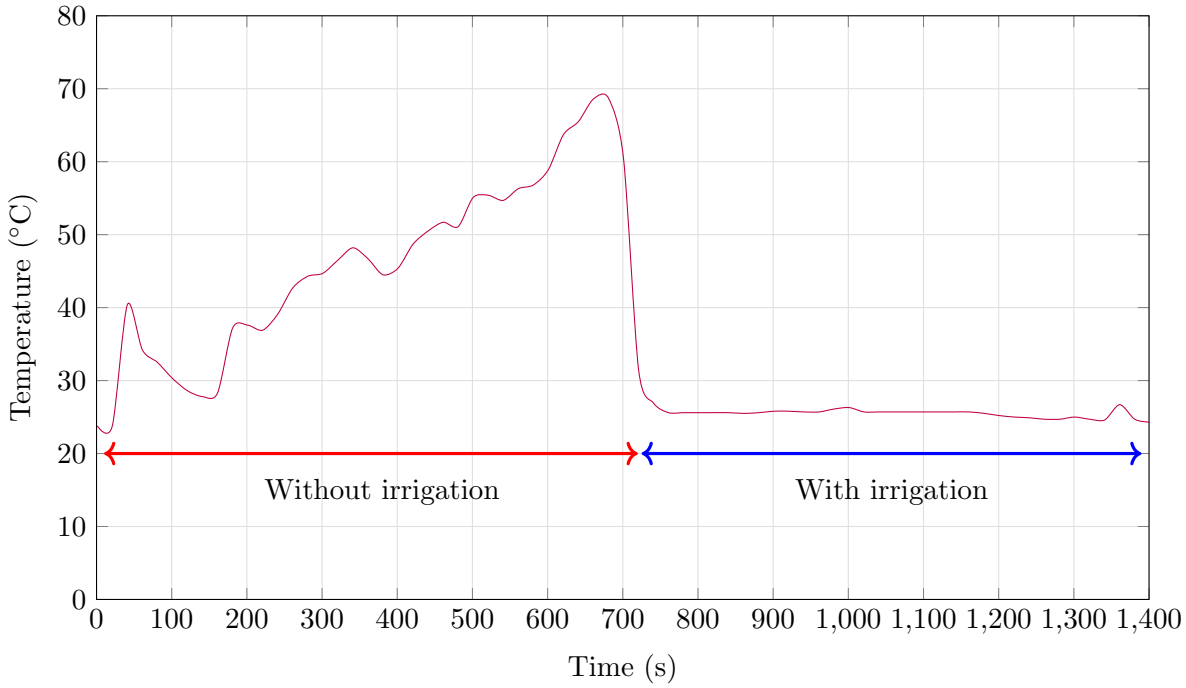

Figure 6.6: Temperature with and without irrigation at the site of penetration

6.3 Comparison of the 2 and 4-ring USNLT

The assembled 4-ring configuration of the USNLT is shown in Figure 6.7. The electrical impedance analysis (Figure 6.8) validated the FEA predictions and gave an insight into how the additional ceramic volume affects the impedance response.

Figure 6.7: 4-ring configurations of USNT

The frequency of L-T and B8 for both configuration correlate with the FEA predictions. For the 2-ring and 4-ring, L-T occurred at 24 kHz and 23.5 kHz respectively. Incorporating an additional pair of piezoceramics causes the resonant frequency of L-T to decrease due to the reduction of stiffness of the device. The impedance magnitude has decreased across the frequency range.

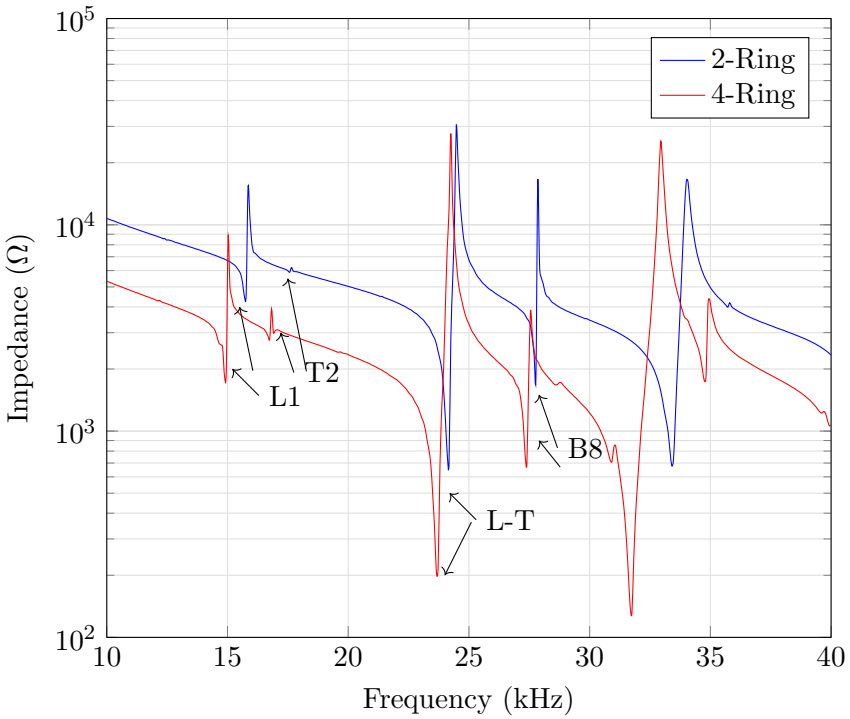

(a)

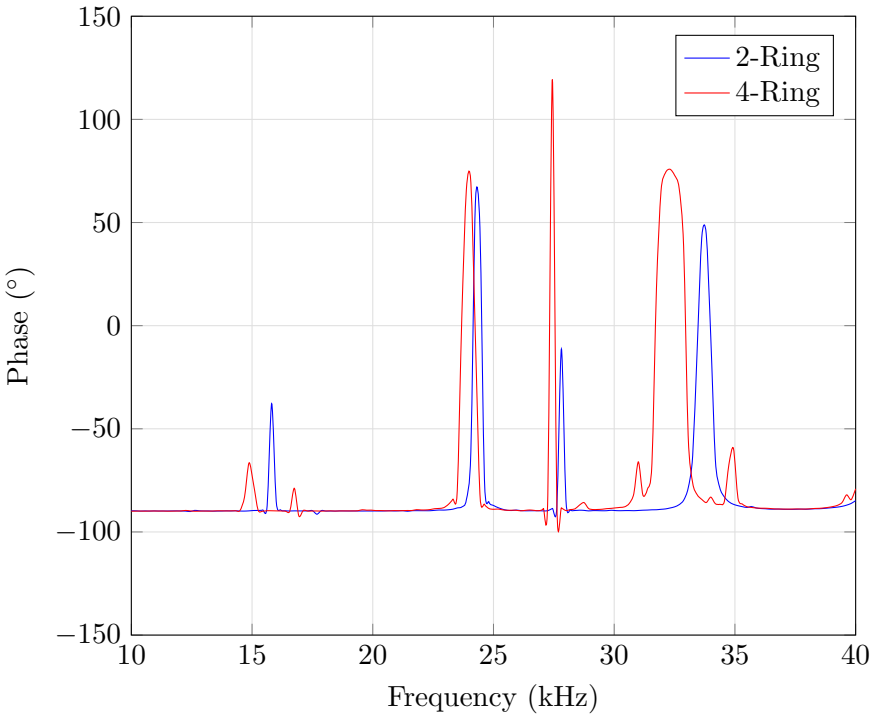

(b)

Figure 6.8: (a) Impedance magnitude (b) phase of USN3 with 2 and 4-rings

Harmonic analysis

Harmonic analysis is conducted to obtain the nonlinear dynamic response of the 4-ring USNLT. The axial and tangential responses are compared with that of the 2-ring configuration detailed in Section 5.3.2. The frequency resolution is 5 Hz between 23 kHz and 24 kHz, for excitation levels incremented from 6 and 132 V_{pp}.

Like the 2-ring USNLT, 4-ring USNLT exhibited a frequency shift downwards with increasing excitation level, indicating a softening nonlinear response. The 4-ring device suffered from a 350 Hz shift for the excitation of 132 V_{pp}. While for 132 V_{pp}, 2-ring USNLT's tuned frequency lowered by 275 Hz. For the 4-ring USNLT hysteretic regions are also observed above 44 V_{pp}. However, for the 2-ring USNLT, hysteretic region is observed above 66 $_{pp}$. For the 4-ring USNLT the width of these regions become significant; 45 Hz, 60 Hz for 110 V_{pp} and 132 V_{pp} respectively.

The combination of larger frequency reduction and wider regions of hysteretic response suggests that the additional rings are causing the 4-ring device to suffer a larger nonlinear response. Nonlinearity in ultrasonic devices stem from two sources, the strain dependent material properties or the internal dissipation of energy in the piezoceramic. Perhaps the latter causes the increased nonlinear response of the 4-ring device.

The peak displacement amplitude for both devices is given in Table 6.1. Good correlation with the FEA predictions can be seen between 6 V_{pp} and 66 V_{pp}, with the L response over 2 x greater than the 2-ring response. However above 66 V_{pp}, the peak L and T responses of 4-ring USNLT (Figure 6.9) become only marginally higher, accredited to the higher nonlinear response of the device. Concurrent with previous results the torsionality of the 4-ring configuration was considerably higher than the steady state dynamic predictions, suggesting that FEA has not constructivly combined the T response achieved by coupling with the third torsional mode and degeneration of the 2nd longitudinal mode.

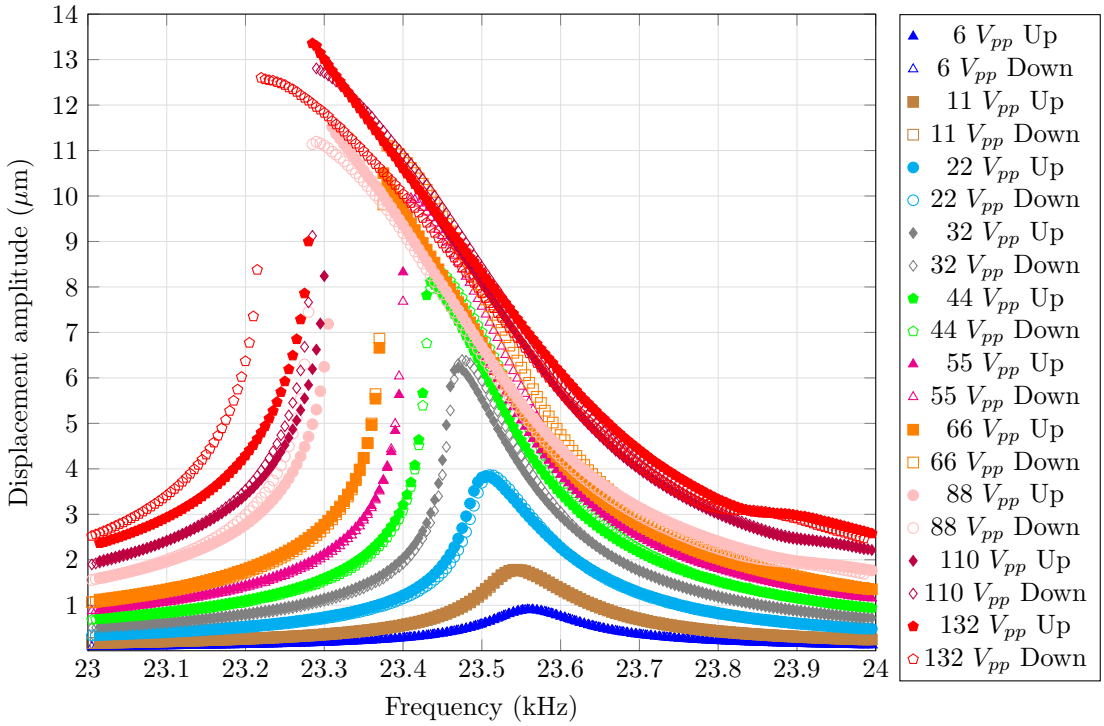

(a) Longitudinal response of 4-Ring USNLT

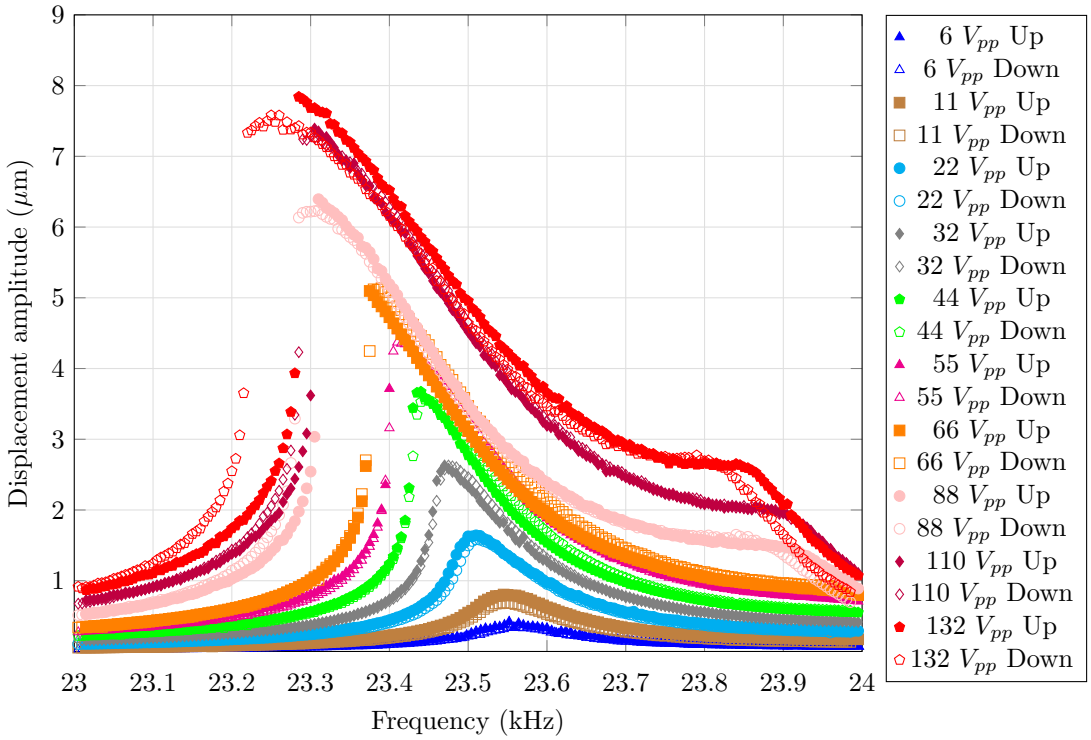

(b) Torsional response of 4-Ring USNLT

Figure 6.9: Harmonic analysis of 4-ring USNLT

Excitation voltage	Displacement Amplitude			
	2-Ring		4-Ring	
	L	T	L	T
(V_{pp})	(μm)			
6	0.4	0.2	1	0.4
11	0.9	0.5	2	0.8
22	1.4	0.9	4	1.7
32	2.2	1.4	6.5	2.6
44	2.9	2	8.3	3.6
55	3.6	2.8	10	4.4
66	4.5	3.2	10.5	5.2
88	6.6	4.5	11.5	6.2
110	9.7	5.8	12	7.3
132	10.6	7.2	13	8.0

Table 6.1: Peak displacement amplitudes across voltage excitations

6.4 Chapter conclusion

Developing the resonant ultrasonic bone biopsy needle towards meeting the needs of a clinical application has been described within this chapter. Surgery of the petrous apex to treat tumours, cyst or lesions is a difficult and challenging procedure involving the patient enduring general anaesthesia for up to 12 hours. The ultrasonic resonant bone biopsy needle proposes as a solution as it can penetrate through the mastoid to obtain a biopsy of the target in a minimally invasive, delicate manner.

A test environment involving the Phacon surgical navigator was established for evaluation of the devices. The ENT models based on CT scans of real patients provided a geometrical model of the bone to be penetrated. Penetration tests proved the needle was capable of penetrating the location however penetrating the initial layer of cortical bone took around 180 seconds causing temperature rise at the site.

To maximise the displacement amplitude and improve the rate of progression, a 4-ring configuration of USNT was investigated. The steady state response predicted the longitudinal

response to be double that of the 2-ring configuration. However, harmonic analysis captured a higher nonlinear response for the 4-ring device than that of the 2-ring configuration which resulted in lower vibrational gains at the higher excitation levels. Therefore if larger power levels are to be used to achieve higher vibrational amplitudes it may not be beneficial to incorporate more than one pair of piezoceramic rings.

The combination of FEA, EMA and harmonic analysis has proven efficient for evaluating ultrasonic needles. The combination of techniques will be used to evaluate further design changes with the aim of producing a device invaluable in the surgical approach of the petrous apex.

Chapter 7

Conclusions and future work

7.1 Conclusions

This thesis focused on developing resonant ultrasonic bone biopsy needles. Evaluation of these devices was achieved through finite element analysis, experimental modal analysis and harmonic analysis, used to predict, validate and characterise each prototype. A resonance tracking system was adopted to excite the needle at the tuned modal frequency and investigate different power modulation techniques. Penetration tests within bone mimic and animal bones were used to evaluate the device, with the biopsy and penetration site investigated through μCT. Although the aim of the work was the design of a surgical needle, the methodology is transferable to the design of other slender or composite mode ultrasonic devices.

A design criterion is set based on the desired vibration response and the application. Full wavelength devices exhibit high modal densities and therefore have a higher likelihood of suffering from mode coupling. To reduce the chance of modal coupling a 10% frequency separation between the tuned and neighbouring modes of vibration is sought. Finite element analysis is used to design the device by monitoring frequency spacing around the tuned mode of interest while incremental changes are made to the needle geometry. A conical needle is adopted to investigate the needle length, exhibited a linear frequency – length relationship for longitudinal, torsional and lower order bending modes within the frequency range of interest. To realise a cylindrical needle tip suitable for insertion a conical to cylinder and cylinder stepped profile were both investigated. The needle length and profile significantly influenced

the frequencies of the modes. For the stepped profile higher order bending modes increased and decreased cyclically as the position of the step moved along the needle profile towards and away from the nodal planes. Finite element analysis was then used to monitor the frequency spacing and resulting torsionality in the design of a composite mode L-T device. The helical cut depth and angle was chosen based on the design criteria set for frequency spacing and achieving high torsion at the tip. All configurations modelled provided sufficient frequency spacing allowing the final configuration to be chosen based on achieving maximum torsion at the distal tip of the needle. Finally, FEA is used to investigate the piezoceramic volume in a Langevin transducer, calculating the steady state displacement amplitude of four 30 kHz ultrasonic transducers with varying quantities of rings. The steady state response and nodal planes suggest that if a portion of the stack is located away from the node, these rings will have a reduced contribution to the vibrational displacement.

Characterisation of the device is conducted through electrical impedance analysis and experimental model analysis. Electrical impedance analysis distinguishes if sufficient preload is applied indicated by the consolidation of the resonant frequency and high electromechanical coupling factor. Strong correlation between the EMA results and FEA predictions are found with errors between the predicted and experimental values of the resonant frequency (L or L-T) of 0.8%, 0.8%, 0.8% and 0.2% for USN1, 2, 3 and USNLT respectively. The modal shape of the L-T mode of USNLT presented as the 2nd longitudinal mode coupling with the third torsional mode of vibration. The combination of coupling with T3 and degeneration of L2 through helical cuts increased torsion at the needle tip. As predicted the curve fitted FRF of each device exhibited dense modal responses due to the slender hollow profile. However sufficient frequency spacing could be confirmed by the L or L-T mode without modal coupling. Each result confirmed FEA as an effective technique for designing ultrasonic needle device based on their vibrational response.

Vibrational stability and maximum power transfer are achieved by adopting a resonance tracking system based on driving at zero phase alongside matching circuitry. A coil transformer manipulates the impedance magnitude of the device to match the output of the amplitude, while the resonance tracking system monitors the voltage and current during operation and alters the frequency to achieve zero phase. The functionality of the system was extended, inspired by phacoemulsification, to investigate waveform shape and power

modulation. Power modulation involved incorporating duty cycles with periods of low excitation which reduced the temperature at the site but also significantly increased the penetration time.

Device evaluation was achieved through penetration tests into biomedical material Sawbones® and animal bone. USN1 successfully penetrated the femur of a Wistar rat with minimal damage, only minor cracking. USN2 was then used to penetrate into metaphysis and cortical bone of ovine femur. A cortical biopsy sample retrieved by USN2 presented as a uniform cylindrical profile, architecturally intact when compared with the biopsy retrieved by the trephine needle, which was shortened and twisted due to the high axial and shear stress applied by the surgeon. While possible that both samples were viable for diagnosis, the ultrasonic needle extracted a core of superior quality.

Harmonic analysis of USN3 and USNLT is used to capture the nonlinear response and determine the effect of the geometry of the device. Both devices exhibit similar downward frequency drifts with increasing excitation levels, indicative of a softening response. The response captured for the L and T displacement of USNLT also possessed comparable nonlinear phenomena suggesting that altering the axial and tangential stiffness does not affect each nonlinear response independently. During penetration tests into ovine cortical the USNLT was faster and more precise than USN3, resulting in a highly circular and less damaged hole surface. Additionally, without the manual rotation the procedure had been simplified. X-ray μCT visualised striations around the penetration sites was indicative of axial motion for USN3 and tangential motion for USNLT.

The surgical treatment of the petrous apex requires an instrument capable of penetrating 50 mm through the mastoid bone with precision and control. As one of the most inaccessible location of the skull, the procedure is challenging, often taking up to 12 hours. The ultrasonic resonant needle poses as a solution, boasting the ability to penetrate bone with little force. The Phacon temporal bone surgical trainer was established as a test environment to evaluate the efficacy of the resonant ultrasonic needle for surgery of the petrous apex. While initial successful penetration of the needle was achieved, a reduction in the penetration time was desired. A combination of steady state dynamic analysis and harmonic analysis investigated the effect of ceramic ring quantity on the vibrational response. Steady state response predicted that vibrational response could be doubled by incorporating an additional 2 rings

into USNLT. However harmonic analysis of the 4-ring USNLT exhibited a higher nonlinear response in terms of frequency shift and regions of hysteresis than the 2-ring configuration. This resulted in the displacement amplitude of the 4-ring configuration being only marginally higher than the 2-ring configuration at high excitation levels.

The current research has demonstrated that resonant ultrasonic bone biopsy needles have the potential to be a transformative for a range of clinical applications, including the surgical treatment of the petrous apex. Combining FEA, EMA and harmonic analysis has proven successful in the realisation of an ultrasonic needle focused on a design criterion based on their vibrational response. Continuing to investigate different design features using these techniques will result in a device which will transform the surgical treatment of the petrous apex and potentiall other clinical applications.

7.2 Future work

The aim of this thesis was the design and evaluation of resonant ultrasonic bone biopsy needles. Further developments could involve:

FEA Predictions

Throughout this work a strong correlation was achieved between the predicted resonant frequency and experimental values. Steady state dynamics obtained the displacement amplitude across a frequency sweep. Further work must improve the model to accurately predict displacement by refining damping. A global damping factor is applied across the system which cannot capture the losses involved between the different contact surfaces. Additionally, further work must accurately predict the torsion at the tip of needle when the response results from coupling combined with degeneration of the longitudinal motion.

Heat generation during bone penetration

Maintaining a low temperature by minimising the build up of heat at the site during the penetration is crucial in avoiding tissue necrosis. The extent of cell death around the penetration site could differentiate the effectiveness of different cooling techniques including internal, external, gas and liquid. Histological evaluation should be established which must include a method for setting the bone tissue to minimise post-harvest cell death.

Surgical treatment of the petrous apex

The device has proven successful in penetrating an ENT model of the mastoid bone, suggestive of its potential in the surgical treatment of the petrous apex. The investigation into the device design should continue using the experimental techniques developed within this thesis. Improving the rate of progress by increasing the vibrational response at the tip of the needle should be sought by altering the geometry and component materials.

Appendix A

List of publications

Journal Papers

1. Mathieson, A., Wallace, R., Cleary, R., Li, L., Simpson, H. and Lucas, M., 2017. Ultrasonic needles for bone biopsy, IEEE Transactions on Ultrasonics, Ferroelectrics, and Frequency Control, vol. 64, pp. 433-440.

Conference Papers

1. Cleary, R., Mathieson, A., Wallace, R., Simpson, H. and Lucas, M., 2015. Design of a slender tuned ultrasonic needle for bone penetration. Physics Procedia, vol. 70, pp. 10-13.

2. Cleary, R., Mathieson, A., Wallace, R., Simpson, H. and Lucas, M., 2015. Assessment of the performance of a novel power ultrasonic biopsy needle. In Ultrasonics Symposium (IUS), IEEE International.

3. Cleary, R. and Lucas, M., 2017. The effect of driving conditions on the performance of an ultrasonic bone biopsy needle. In Proceedings of Meetings on Acoustics ICU, vol. 32, 020011.

4. Cleary, R. and Lucas, M., 2018. Comparison of Longitudinal-Mode and Longitudinal-Torsional Mode Ultrasonic Bone Biopsy Devices. In Ultrasonics Symposium (IUS), IEEE International.

References

[1] "Bone marrow biopsy." www.mayoclinic.org. Accessed: 2018-08-14.

[2] N. Hjortholm, E. Jaddini, K. Hałaburda, and E. Snarski, "Strategies of pain reduction during the bone marrow biopsy," *Annals of Hematology*, vol. 92, no. 2, pp. 145–149, 2013.

[3] "Bone marrow trephine biopsy system." www.ranfac.com. Accessed: 2019-06-29.

[4] M. F. Zahid, "Methods of reducing pain during bone marrow biopsy: a narrative review," *Annals of Palliative Medicine*, vol. 4, no. 4, pp. 184–193, 2015.

[5] T. Valebjørg, B. Spahic, F. Bremtun, J. Kahrs, J. Hammerstrøm, R. Brudevold, J. Kolflaath, and W. Ghanima, "Pain and bleeding associated with trephine biopsy," *European Journal of Haematology*, vol. 93, no. 4, pp. 267–272, 2014.

[6] P. Vanhelleputte, K. Nijs, M. Delforge, G. Evers, and S. Vanderschueren, "Pain during bone marrow aspiration: prevalence and prevention," *Journal of Pain and Symptom Management*, vol. 26, no. 3, pp. 860–866, 2003.

[7] M. Sarigianni, E. Vlachaki, S. Chissan, F. Klonizakis, E. Vetsiou, K. I. Anastasiadou, E. Ioannidou-Papagiannaki, and I. Klonizakis, "Haematoma caused by bone marrow aspiration and trephine biopsy," *Hematology Reports*, vol. 3, no. 3, 2011.

[8] J. N. Feeney and J. E. Barry, "Massive retroperitoneal hemorrhage post bone marrow biopsy mimicking ruptured abdominal aortic aneurysm," *European Journal of Radiology Extra*, vol. 59, no. 2, pp. 77–80, 2006.

[9] W. Jamaludin, S. Mukari, and S. Wahid, "Retroperitoneal hemorrhage associated with bone marrow trephine biopsy," *The American journal of Case Reports*, vol. 14, pp. 489–493, 2013.

[10] J. Kennedy, G. R. ter Haar, and D. Cranston, "High intensity focused ultrasound: surgery of the future?," *The British Journal of Radiology*, vol. 76, no. 909, pp. 590–599, 2003.

[11] F. Murat, L. Poissonnier, G. Pasticier, and A. Gelet, "High-intensity focused ultrasound for prostate cancer," *Cancer Control*, vol. 14, no. 3, pp. 244–249, 2007.

[12] A. Gelet, J. Chapelon, R. Bouvier, O. Rouviere, Y. Lasne, D. Lyonnet, and J. Dubernard, "Transrectal high-intensity focused ultrasound: minimally invasive therapy of localized prostate cancer," *Journal of Endourology*, vol. 14, no. 6, pp. 519–528, 2000.

[13] "Phaco cataract surgery." www.visiomed.co.za. Accessed: 2018-08-17.

[14] C. D. Kelman, "Phaco-emulsification and aspiration: a new technique of cataract removal: a preliminary report," *American Journal of Ophthalmology*, vol. 64, no. 1, pp. 23–35, 1967.

[15] F. Ascaso and V. Huerva, "The history of cataract surgery," in *Cataract Surgery*, InTech, 2013.

[16] D. Yorston, "High-volume surgery in developing countries," *Eye (London)*, vol. 19, no. 10, pp. 1083–1089, 2005.

[17] D. Wuchinich, A. Broadwin, and R. Andersen, "Ultrasonic aspirator," Dec. 1977. US Patent 4,063,557.

[18] R. Chopp, B. Shah, and J. Addonizio, "Use of ultrasonic surgical aspirator in renal surgery," *Urology*, vol. 22, no. 2, pp. 157–159, 1983.

[19] B. J. O'Daly, E. Morris, G. P. Gavin, J. M. O'Byrne, and G. B. McGuinness, "High-power low-frequency ultrasound: A review of tissue dissection and ablation in medicine and surgery," *Journal of Materials Processing Technology*, vol. 200, no. 1-3, pp. 38–58, 2008.

[20] J. Amaral, "Ultrasonic dissection," *Endoscopic Surgery and Allied Technologies*, vol. 2, no. 3-4, pp. 181–185, 1994.

[21] R. Gruber, F.-J. Kramer, H.-A. Merten, and H. Schliephake, "Ultrasonic surgery — an alternative way in orthognathic surgery of the mandible: A pilot study," *International Journal of Oral and Maxillofacial surgery*, vol. 34, no. 6, pp. 590–593, 2005.

[22] J. Sherman and H. Davies, "Ultracision: the harmonic scalpel and its possible uses in maxillofacial surgery," *British Journal of Oral and Maxillofacial Surgery*, vol. 38, no. 5, pp. 530–532, 2000.

[23] T. Kinoshita, E. Kanehira, K. Omura, K. Kawakami, and Y. Watanabe, "Experimental study on heat production by a 23.5 khz ultrasonically activated device for endoscopic surgery," *Surgical Endoscopy*, vol. 13, no. 6, pp. 621–625, 1999.

[24] "Harmonic scalpel." www.ethicon.com. Accessed: 2018-08-17.

[25] P. Hennet, "Piezoelectric bone surgery: a review of the literature and potential applications in veterinary oromaxillofacial surgery," *Frontiers in veterinary science*, vol. 2, 2015.

[26] J. Drane, B. Matis, and D. Sexson, "A triservice comparison of dental scaling devices: sonic and ultrasonic," tech. rep., School of Aerospace Medicine, Brooks Air Force Base, Texas, 1989.

[27] "Cavitron touch ultrasonic scaler." www.uk.cavitronsystems.com/. Accessed: 2019-07-01.

[28] M. Labanca, F. Azzola, R. Vinci, and L. F. Rodella, "Piezoelectric surgery: twenty years of use," *British Journal of Oral and Maxillofacial Surgery*, vol. 46, no. 4, pp. 265–269, 2008.

[29] C. Landes, S. Stubinger, A. Ballon, and R. Sader, "Piezoosteotomy in orthognathic surgery versus conventional saw and chisel osteotomy," *Oral and Maxillofacial Surgery*, vol. 12, no. 3, pp. 139–147, 2008.

[30] G. Spinelli, D. Lazzeri, M. Conti, T. Agostini, and G. Mannelli, "Comparison of piezosurgery and traditional saw in bimaxillary orthognathic surgery," *Journal of Cranio-Maxillofacial Surgery*, vol. 42, no. 7, pp. 1211–1220, 2014.

[31] "Mectron piezosurgery device." www.dental.mectron.com/. Accessed: 2018-08-17.

[32] H. Hadeishi, A. Suzuki, N. Yasui, and Y. Satou, "Anterior clinoidectomy and opening of the internal auditory canal using an ultrasonic bone curette," *Neurosurgery*, vol. 52, no. 4, pp. 867–871, 2003.

[33] P. Cappabianca, L. M. Cavallo, I. Esposito, M. Barakat, and F. Esposito, "Bone removal with a new ultrasonic bone curette during endoscopic endonasal approach to the sellar-suprasellar area," *Operative Neurosurgery*, vol. 66, 2010.

[34] H. Nakagawa, S. D. Kim, J. Mizuno, Y. Ohara, and K. Ito, "Technical advantages of an ultrasonic bone curette in spinal surgery," *Journal of Neurosurgery: Spine*, vol. 2, no. 4, pp. 431–435, 2005.

[35] K. Ito, S. Ishizaka, T. Sasaki, T. Miyahara, T. Horiuchi, K. Sakai, H. Shigeta, and K. Hongo, "Safe and minimally invasive laminoplastic laminotomy using an ultrasonic bone curette for spinal surgery," *Surgical neurology*, vol. 72, no. 5, pp. 470–475, 2009.

[36] M. Dellepiane, R. Mora, F. A. Salzano, and A. Salami, "Clinical evaluation of piezoelectric ear surgery," *Ear, Nose & Throat Journal*, vol. 87, no. 4, pp. 212–216, 2008.

[37] A. Salami, M. Dellepiane, F. A. Salzano, and R. Mora, "Piezosurgery in the excision of middle-ear tumors: effects on mineralized and non-mineralized tissues," *Medical Science Monitor*, vol. 13, no. 12, pp. 25–29, 2007.

[38] G. Augustin, T. Zigman, S. Davila, T. Udilljak, T. Staroveski, D. Brezak, and S. Babic, "Cortical bone drilling and thermal osteonecrosis," *Clinical Biomechanics*, vol. 27, no. 4, pp. 313–325, 2012.

[39] K. Alam, A. Mitrofanov, and V. Silberschmidt, "Experimental investigations of forces and torque in conventional and ultrasonically-assisted drilling of cortical bone," *Medical engineering & Physics*, vol. 33, no. 2, pp. 234–239, 2011.

[40] D. Zerbino, "Biopsy: its history, current and future outlook," *Likars' ka Sprava*, no. 3-4, pp. 1–9, 1994.

[41] C. Nezelof and J. Guinebretière, "Ernest Besnier inventor of the word biopsy," *La Revue du Praticien*, vol. 56, no. 18, pp. 2081–2085, 2006.

[42] M. Wintrobe, *Hematology, the blossoming of a science: A story of inspiration and effort*. Lea & Febiger Philadelphia, 1985.

[43] L. Parapia, "Trepanning or trephines: a history of bone marrow biopsy," *British Journal of Haematology*, vol. 139, no. 1, pp. 14–19, 2007.

[44] N. Henning and J. Korth, "Die diagnostische sternalspülung," *Journal of Molecular Medicine*, vol. 13, no. 34, pp. 1219–1220, 1934.

[45] "Trephine bone biopsy needles." www.dixons-uk.com. Accessed: 2018-08-21.

[46] L. Sacker and B. Nordin, "A simple bone biopsy needle," *The Lancet*, vol. 263, no. 6807, p. 347, 1954.

[47] I. Silverman, "A new biopsy needle," *The American Journal of Surgery*, vol. 40, no. 3, pp. 671–672, 1938.

[48] K. Jamshidi, W. R. Swaim, and H. E. Windschitl, "Biopsy technique and biopsy device," 1971. US Patent 3598108A.

[49] A. Shaltot, P. Michell, J. Betts, A. Darby, and P. Gishen, "Jamshidi needle biopsy of bone lesions," *Clinical Radiology*, vol. 33, no. 2, pp. 193–196, 1982.

[50] R. Burkhardt and R. Meier, "Power tool for excising a bone or cartilage biopsy." US Patent 4,936,313.

[51] "The Arrow Oncontrol® powered bone access system." www.arrowoncontrol.com/. Accessed: 2018-07-22.

[52] J. Berenson, O. Yellin, B. Blumenstein, D. Bojanower, J. Croopnick, D. Aboulafia, G. Upadhyaya, and C. Spadaccini, "Using a powered bone marrow biopsy system results in shorter procedures, causes less residual pain to adult patients, and yields larger specimens," *Diagnostic Pathology*, vol. 6, no. 1, p. 23, 2011.

[53] R. T. Swords, J. Anguita, R. A. Higgins, A. C. Yunes, M. Naski, S. Padmanabhan, K. R. Kelly, D. Mahalingam, T. Philbeck, L. Miller, *et al.*, "A prospective randomised study of a rotary powered device (oncontrol) for bone marrow aspiration and biopsy," *Journal of Clinical Pathology*, vol. 64, no. 9, pp. 809–813, 2011.

[54] C. Bucher, T.Lehmann, A. Tichelli, A. Tzankov, S. Dirnhofer, J. Passweg, and A. Rovó, "Comparison of a powered bone marrow biopsy device with a manual system: results of a prospective randomised controlled trial," *Journal of Clinical Pathology*, pp. 24–28, 2012.

[55] J. Fauvel, R. Flood, and R. J. Wilson, *Music and Mathematics: From Pythagoras to Fractals*. Oxford University Press, 2006.

[56] L. Judson, *Aristotle's Physics: A Collection of Essays*. Clarendon Press, USA, 1995.

[57] J. MacLachlan, *Galileo Galilei: The First Physicist*. Oxford University Press, 1999.

[58] R. Hooke, *The Posthumous Works of Robert Hooke*. Royal Society, London, 1705.

[59] R. Beyer, *Sounds of our times, two hundred years of acoustics*. Springer Science and Business Media, 1999.

[60] J. W. S. B. Rayleigh, *The Theory of Sound*. MacMillan and Co., 1896.

[61] J. Roelandt, "Seeing the invisible: A short history of cardiac ultrasound," *European Journal of Echocardiography*, vol. 1, no. 1, pp. 8– 11, 2000.

[62] V. Mckusick, *Cardiovascular sound in health and disease*. Tindall and Cox, Ltd, 1958.

[63] F. Galton, *Inquiries into human faculty and its development*. MacMillan and Co., 1883.

[64] T. Greenslade Jr, "The acoustical apparatus of Rudolph Koenig," *The Physics Teacher*, vol. 30, pp. 518–524, 1992.

[65] G. Pierce and D. Griffin, "Experimental determination of supersonic notes emitted by bats," *Journal of Mammalogy*, vol. 19, no. 4, pp. 454– 1455, 1938.

[66] M. Gibbs, "Magnetostriction: 150 years from the discovery," *Physica Scripta*, vol. T45, pp. 115–119, 1992.

[67] W. Heywang, K. Lubitz, and W. Wersing, *Piezoelectricity: Evolution and future of a technology*. Springer Science and Business Media, 2008.

[68] E. Gold, *Lewis Fry Richardson, 1881-1953*. The Royal Society London, 1954.

[69] R. Fessenden, "Method for measuring distance," 1917. US Patent 1,217,585A.

[70] S. Katzir, "Who knew piezoelectricity? rutherford and langevin on submarine detection and the invention of sonar," *The Royal Society*, vol. 66, pp. 141–157, 2012.

[71] C. Chilowsky and P. Langevin, "Production of submarine signals and the location of submarine objects," 1917. US Patent 171547A.

[72] W. Cady, "The piezo-electric resonator," *Proceeding of the Institue of Radio Engineers*, vol. 10, no. 2, pp. 84–114, 1922.

[73] G. Pierce, "Piezoelectric crystal oscillators applied to the precision measurement of the velocity of sound in air and CO2 at high frequencies," *Proceedings of the American Academy of Arts and Sciences*, vol. 60, no. 5, pp. 271–302, 1925.

[74] K. Van Dyke, "The piezo-electric resonator and it's equivalent network," *Proceedings of the Institute of Radio Engineers*, vol. 16, no. 6, p. 742–764, 1928.

[75] S. Sokolov, "On the problem of the propagation of ultrasonic oscillations in various bodies," *Elek Nachr Tech*, vol. 6, no. 454-460, p. 92, 1929.

[76] R. Wood and A. Loomis, "The physical and biological effects of high-frequency sound-waves of great intensity," *The London, Edinburgh, and Dublin Philosophical Magazine and Journal of Science*, vol. 4, no. 22, pp. 417–436, 1927.

[77] M. Catuna, "Sonic energy; a possible dental application," *Annals of Dentistry*, vol. 12, pp. 100–101, 1953.

[78] L. Balamuth, "Ultrasonics and dentistry," *Sound: Its uses and control*, vol. 2, no. 2, pp. 15–19, 1963.

[79] D. Zinner, "Recent ultrasonic dental studies, including periodontia, without the use of an abrasive," *Jounal of Dental research*, vol. 34, pp. 748–749, 1955.

[80] W. Johnson and J. Wilson, "The application of the ultrasonic dental unit to scaling procedures," *Journal of Periodontology*, vol. 28, no. 4, pp. 264–271, 1957.

[81] M. Richman, "The use of ultrasonics in root canal therapy and root resection," *Journal of Dental Medicine*, vol. 12, pp. 12–18, 1957.

[82] H. Martin and W.Cunningham, "Endosonics–the ultrasonic synergistic system of endodontics," *Dental Traumatology*, vol. 1, no. 6, pp. 201–206, 1985.

[83] P. Lindstrom, "Prefrontal ultrasonic irradiation — a substitute for lobotomy," *AMA Archives of Neurology & Psychiatry*, vol. 72, no. 4, pp. 399–425, 1954.

[84] W. Fry, J. Barnard, F. Fry, and J. Brennan, "Ultrasonically produced localized selective lesions in the central nervous system," *American Journal of Physical Medicine & Rehabilitation*, vol. 34, no. 3, pp. 413–423, 1955.

[85] R. Meyers, W. Fry, F. Fry, L. Dreyer, D. Schultz, and R. Noyes, "Early experiences with ultrasonic irradiation of the pallidofugal and nigral complexes in hyperkinetic and hypertonic disorders," *Journal of Neurosurgery*, vol. 16, no. 1, pp. 32–54, 1959.

[86] V. Poljakov, *Ultrasonic bonding of bones and cutting of live biological tissues.* Mir Publishers, 1974.

[87] M. Volkov, "The use of ultrasonic instrumentation for the transection and uniting of bone tissue in orthopaedic surgery," *Reconstr Surg Traumatol*, vol. 14, pp. 147–152, 1974.

[88] E. Flamm, J. Ransohoff, D. Wuchinich, and A. Broadwin, "Preliminary experience with ultrasonic aspiration in neurosurgery," *Neurosurgery*, vol. 2, no. 3, pp. 240–245, 1978.

[89] W. J. B. Hodgson and A. J. McElhinney, "Ultrasonic partial splenectomy," *Surgery*, vol. 91, no. 3, pp. 346–348, 1982.

[90] D. G. Wuchinich, A. Broadwin, and R. P. Andersen, "Ultrasonic aspirator," Sept. 23 1980. US Patent 4,223,676.

[91] P. Alken, G. Hutschenreiter, R. Günther, and M. Marberger, "Percutaneous stone manipulation," *The Journal of Urology*, vol. 125, no. 4, pp. 463–466, 1981.

[92] V. Alfred, "Vibratory surgical instruments," Aug. 9 1955. US Patent 2,714,890.

[93] H. Aro, H. Kallioniemi, A. Aho, and P. Kellokumpu-Lehtinen, "Ultrasonic device in bone cutting: A histological and scanning electron microscopical study," *Acta Orthopaedica Scandinavica*, vol. 52, no. 1, pp. 5–10, 1981.

[94] J. E. Horton, T. M. Tarpley Jr, and J. R. Jacoway, "Clinical applications of ultrasonic instrumentation in the surgical removal of bone," *Oral Surgery, Oral Medicine, Oral Pathology*, vol. 51, no. 3, pp. 236–242, 1981.

[95] B. Khambay and A. Walmsley, "Investigations into the use of an ultrasonic chisel to cut bone. part 1: forces applied by clinicians," *Journal of Dentistry*, vol. 28, no. 1, pp. 31–37, 2000.

[96] B. Khambay and A. Walmsley, "Investigations into the use of an ultrasonic chisel to cut bone. part 2: cutting ability," *Journal of Dentistry*, vol. 28, no. 1, pp. 39–44, 2000.

[97] "Mectron piezosurgery." www.medical.mectron.com/. Accessed: 2018-07-23.

[98] G. Eggers, J. Klein, J. Blank, and S. Hassfeld, "Piezosurgery®: an ultrasound device for cutting bone and its use and limitations in maxillofacial surgery," *British Journal of Oral and Maxillofacial Surgery*, vol. 42, no. 5, pp. 451–453, 2004.

[99] T. Vercellotti and A. Pollack, "A new bone surgery device: sinus grafting and periodontal surgery," *Compendium of Continuing Education in Dentistry*, vol. 27, no. 5, pp. 319–325, 2006.

[100] A. Gleizal, J. Bera, B. Lavandier, and J. Beziat, "Piezoelectric osteotomy: a new technique for bone surgery—advantages in craniofacial surgery," *Child's Nervous System*, vol. 23, no. 5, pp. 509–513, 2007.

[101] "Misonix bone scalpel." www.misonix.com. Accessed: 2018-07-23.

[102] K. Alam, M. Khan, and V. Silberschmidt, "Analysis of forces in conventional and ultrasonically assisted plane cutting of cortical bone," *Proceedings of the Institution of Mechanical Engineers, Part H: Journal of Engineering in Medicine*, vol. 227, no. 6, pp. 636–642, 2013.

[103] B. Kotrikova, R. Wirtz, R. Krempien, J. Blank, G. Eggers, A. Samiotis, and J. J. Mühling, "Piezosurgery — a new safe technique in cranial osteoplasty?," *International Journal of Oral and Maxillofacial Surgery*, vol. 35, no. 5, pp. 461–465, 2006.

[104] P. Nordera, S. di Spilimbergo, A. Stenico, U. Fornezza, L. Volpin, and E. Padula, "The cutting-edge technique for safe osteotomies in craniofacial surgery: the piezosurgery bone scalpel," *Plastic and Reconstructive Surgery*, vol. 120, no. 7, pp. 1989–1995, 2007.

[105] M. Onen, E. Yuvruk, S. Akay, and S. Naderi, "The reliability of the ultrasonic bone scalpel in cervical spondylotic myelopathy: a comparative study of 46 patients," *World Neurosurgery*, vol. 84, no. 6, pp. 1962–1967, 2015.

[106] R. Pandey and S. Panda, "Drilling of bone: A comprehensive review," *Journal of Clinical Orthopaedics and Trauma*, vol. 4, no. 1, pp. 15–30, 2013.

[107] K. Alam and V. Silberschmidt, "Analysis of temperature in conventional and ultrasonically-assisted drilling of cortical bone with infrared thermography," *Technology and Health Care*, vol. 22, no. 2, pp. 243–252, 2014.

[108] K. Alam, E. Hassan, and I. Bahadur, "Experimental measurements of temperatures in ultrasonically assisted drilling of cortical bone," *Biotechnology & Biotechnological Equipment*, vol. 29, no. 4, pp. 753–757, 2015.

[109] L. Merkulov and A. Kharitonov, "Design of ultrasonic concentrators," *Soviet Physics Acoustics*, vol. 3, no. 1957, pp. 246–255, 1957.

[110] L. Balamuth, "Mechanical impedance transformers in relation to ultrasonic machining," *The Journal of the Acoustical Society of America*, vol. 26, no. 5, pp. 934–934, 1954.

[111] L. L.G. Merkulov and A. Kharitonov, "Theory and analysis of sectional concentrators," *The Journal of the Acoustical Society of America*, vol. 5, pp. 183–190, 1959.

[112] D. Ensminger, "Solid cone in longitudinal half-wave resonance," *The Journal of the Acoustical Society of America*, vol. 32, no. 2, pp. 194–196, 1960.

[113] E. Neppiras, "Mechanical transformers for producing very large motion," *Acustica*, vol. 13, pp. 368–370, 1963.

[114] E. Neppiras, "Effect of shape and internal impedance on power-handling capacity and efficiency of ultrasonic transducers," *Acustica*, vol. 15, no. 1, pp. 58–61, 1965.

[115] G. Amza and D. Drimer, "The design and construction of solid concentrators for ultrasonic energy," *Ultrasonics*, vol. 14, no. 5, pp. 223–226, 1976.

[116] S. Muhlen, "Design of an optimized high-power ultrasonic transducer," in *IEEE Ultrasonics Symposium*, pp. 1631–1634, IEEE, 1990.

[117] K. O'Shea, "Enhanced vibration control of ultrasonic tooling using finite element analysis," *Vibration Analysis–Analytical and Computational*, pp. 259–265, 1991.

[118] S. Amin, M. Ahmed, and H. Youssef, "Computer-aided design of acoustic horns for ultrasonic machining using finite-element analysis," *Journal of Materials Processing Technology*, vol. 55, no. 3-4, pp. 254–260, 1995.

[119] M. Lucas and G. Chapman, "Vibration analysis at ultrasonic frequencies," *Vibration analysis - Techniques and applications*, pp. 235–240, 1989.

[120] G. Chapman and M. Lucas, "Frequency analysis of an ultrasonically excited thick cylinder," in *Modern Practice in Stress and Vibration Analysis*, pp. 69–77, Elsevier, 1989.

[121] G. Graham, J. Petzing, M.Lucas, and J. Tyrerd, "Whole-field modal analysis using electronic speckle pattern interferometry," in *International Conference on Vibration Measurements by Laser Techniques: Advances and Applications*, vol. 2868, pp. 352–362, 1996.

[122] G. Graham, J. Petzing, M. Lucas, and J.Tyrer, "Quantitative modal analysis using electronic speckle pattern interferometry," *Optics and Lasers in Engineering*, vol. 31, no. 2, pp. 147–161, 1999.

[123] G. Graham, J. Petzing, and M. Lucas, "Modal analysis of ultrasonic block horns by espi," *Ultrasonics*, vol. 37, no. 2, pp. 149–157, 1999.

[124] G. Busch, "Early history of ferroelectricity," *Ferroelectrics*, vol. 74, no. 1, pp. 267–284, 1987.

[125] R. N. C.A. Randall, C. L.E. CrossRandall, R. Newnham, and L. Cross, "History of the first ferroelectric oxide, BaTiO3," *Materials Research Institute The Pennsylvania State University*, 2004.

[126] R. Gray, "Transducer and method of making the same," Nov. 1 1949. US Patent 2,486,560.

[127] B. Jaffe, R. Roth, and S. Marzullo, "Piezoelectric properties of lead zirconate-lead titanate solid-solution ceramics," *Journal of Applied Physics*, vol. 25, no. 6, pp. 809–810, 1954.

[128] B. Jaffe and W. Cook, *Piezoelectric Ceramics*. Academic press, 1971.

[129] D. DeAngelis and G. Schulze, "Performance of PZT8 versus PZT4 piezoceramic materials in ultrasonic transducers," *Physics Procedia*, vol. 87, pp. 85–92, 2016.

[130] P. Panda and B. Sahoo, "PZT to lead free piezo ceramics: a review," *Ferroelectrics*, vol. 474, no. 1, pp. 128–143, 2015.

[131] J. Rödel, K. Webber, R. Dittmer, W. Jo, M. Kimura, and D. Damjanovic, "Transferring lead-free piezoelectric ceramics into application," *Journal of the European Ceramic Society*, vol. 35, no. 6, pp. 1659–1681, 2015.

[132] E. Sun and W. Cao, "Relaxor-based ferroelectric single crystals: Growth, domain engineering, characterization and applications," *Progress in Materials Science*, vol. 65, pp. 124–210, 2014.

[133] T. Kobayashi, S. Shimanuki, S. Saitoh, and Y. Yamashita, "Improved growth of large lead zinc niobate titanate piezoelectric single crystals for medical ultrasonic transducers," *Japanese Journal of Applied Physics*, vol. 36, no. 9S, pp. 6035–6038, 1997.

[134] D. Williams, "On the nature of biomaterials," *Biomaterials*, vol. 30, no. 30, pp. 5897–5909, 2009.

[135] N. Huebsch and D. Mooney, "Inspiration and application in the evolution of biomaterials," *Nature*, vol. 462, no. 7272, pp. 426–432, 2009.

[136] T. Hanawa, "Research and development of metals for medical devices based on clinical needs," *Science and Technology of Advanced Materials*, vol. 13, no. 6, 2012.

[137] B. Love, *Biomaterials: a systems approach to engineering concepts*. Academic Press, 2017.

[138] T. I. Kim, "A tribute to Dr. Per-Ingvar Brånemark," *Journal of Periodontal & Implant Science*, vol. 44, no. 6, p. 265, 2014.

[139] "Cavitron ultrasonic aspirator." www.demo.webassign.net/. Accessed: 2018-08-21.

[140] L. D. Rozenberg, *Sources of high-intensity ultrasound*, vol. 1. Springer Science & Business Media, 2013.

[141] H. Barth, "Ultrasonic magnetic surface finisher," Nov. 13 1973. US Patent 3,771,939.

[142] O. Ohnishi, O. Myohga, T. Uchikawa, M.Tamegai, T.Inoue, and S.Takahashi, "Piezoelectric ultrasonic motor using longitudinal-torsional composite resonance vibration," *IEEE transactions on ultrasonics, ferroelectrics, and frequency control*, vol. 40, no. 6, pp. 687–693, 1993.

[143] Y. Izuno and M. Nakaoka, "High performance and high precision ultrasonic motor-actuated positioning servo drive system using improved fuzzy-reasoning controller," in *Power Electronics Specialist Conference*, vol. 2, pp. 1269–1274, IEEE, 1994.

[144] J. Gallego-Juárez, G. Rodriguez-Corral, and L. Gaete-Garreton, "An ultrasonic transducer for high power applications in gases," *Ultrasonics*, vol. 16, no. 6, pp. 267–271, 1978.

[145] L. Shuyu, "Optimization of the performance of the sandwich piezoelectric ultrasonic transducer," *The Journal of the Acoustical Society of America*, vol. 115, no. 1, pp. 182–186, 2004.

[146] H. Nagashima and S. Ueha, "Study of longitudinal-torsional composite vibrator system," *The Journal of the Acoustical Society of Japan*, vol. 45, no. 2, pp. 94–100, 1989.

[147] Y. Watanabe, Y. Tsuda, and E. Mori, "A longitudinal-flexural complex-mode ultrasonic high-power transducer system with one-dimensional construction," *Japanese Journal of Applied Physics*, vol. 32, no. 5B, pp. 24–30, 1993.

[148] J. Tsujino, "Ultrasonic motor using a one-dimensional longitudinal-torsional vibration converter with diagonal slits," *Smart Materials and Structures*, vol. 7, no. 3, p. 345, 1998.

[149] J. Tsujino, R. Suzuki, and H. Yasojima, "Load characteristics of ultrasonic rotary motor using a longitudinal-torsional vibration converter," in *IEEE Ultrasonics Symposium*, vol. 1, pp. 377–382, IEEE, 1996.

[150] J. Tsujino, T. Ueoka, K. Otoda, and A.Fujimi, "One-dimensional longitudinal–torsional vibration converter with multiple diagonally slitted parts," *Ultrasonics*, vol. 38, no. 1-8, pp. 72–76, 2000.

[151] J. Tsujino, T. Ueoka, T. Kashino, and F. Sugahara, "Transverse and torsional complex vibration systems for ultrasonic seam welding of metal plates," *Ultrasonics*, vol. 38, no. 1-8, pp. 67–71, 2000.

[152] J. Tsujino, M. Takeuchi, and H.Koshisako, "Ultrasonic rotary motor using a longitudinal-torsional vibration converter," in *IEEE Ultrasonics Symposium*, pp. 887–892, IEEE, 1992.

[153] J. Tsujino, T. Sano, H. Ogata, S. Tanaka, and Y. Harada, "Complex vibration ultrasonic welding systems with large area welding tips," *Ultrasonics*, vol. 40, no. 1-8, pp. 361–364, 2002.

[154] J. Tsujino, K. Nakai, K. Sako, N. Ikegami, K. Noda, and R. Suzuki, "Load characteristics and vibration loci at the driving surfaces of ultrasonic rotary motor using a longitudinal-torsional vibration converter," *Japanese Journal of Applied Physics*, vol. 37, no. 5B, 1998.

[155] D. Wuchinich, "Endoscopic ultrasonic rotary electro-cauterizing aspirator," 1993. US Patent 5,176,677.

[156] D. Wuhinich, "Longitudinal-torsional ultrasonic tissue dissection," 2010. US Patent 7,762,979 B2.

[157] M. Boukhny, "Torsional ultrasound handpiece," 2000. US Patent 6,077,285.

[158] L. Walsh, "Piezosurgery: an increasing role in dental hard tissue surgery," *Australasian Dental Practice*, vol. 18, no. 5, pp. 52–56, 2007.

[159] Stryker, "Stryker sonopet ultrasonic aspirator." www.neurosurgical.stryker.com. Accessed: 2019-07-01.

[160] H. Al-Budairi, P. Harkness, and M. M. Lucas, "A strategy for delivering high torsionality in longitudinal-torsional ultrasonic devices," in *Applied Mechanics and Materials*, vol. 70, pp. 339–344, Trans Tech Publ, 2011.

[161] H. Al-Budairi, M. Lucas, and P. Harkness, "Optimisation of the longitudinal-torsional output of a half-wavelength langevin transducer," *41st Annual Symposium of the Ultrasonic Industry Association*, 2012.

[162] P. Harkness, A. Cardoni, and M. Lucas, "Ultrasonic rock drilling devices using longitudinal-torsional compound vibration," in *IEEE Ultrasonics Symposium*, pp. 2088–2091, IEEE, 2009.

[163] P. Harkness and M. Lucas, "Development of a switchable system for longitudinal and longitudinal-torsional vibration extraction," *Ultrasonic Industry Association*, 2012.

[164] A. Ramos-Fernandez, J. Gallego-Juarez, and F. Montoya-Vitini, "Automatic system for dynamic control of resonance in high power and high q ultrasonic transducers," *Ultrasonics*, vol. 23, no. 4, pp. 151–156, 1985.

[165] B. Mortimer, T. Bruyn, J. Davies, and J. Tapson, "High power resonant tracking amplifier using admittance locking," *Ultrasonics*, vol. 39, no. 4, pp. 257–261, 2001.

[166] W. Littmann, T. Hemsel, C. Kauczor, J. Wallaschek, and M. Sinha, "Load-adaptive phase-controller for resonant driven piezoelectric devices," in *World Congress Ultrasonics*, vol. 48, pp. 547–550, 2003.

[167] R. Briot, M. Guillemot-Amadei, A. Pelourson, and C. Garabedian, "Generators for piezoelectric motors," *Measurement Science and Technology*, vol. 4, no. 9, p. 938, 1993.

[168] X. Liu, A. Colli-Menchi, J. Gilbert, D. Friedrichs, K. Malang, and E. Sánchez-Sinencio, "An automatic resonance tracking scheme with maximum power transfer for piezoelectric transducers," *IEEE Transactions on Industrial Electronics*, vol. 62, no. 11, pp. 7136–7145, 2015.

[169] V. Babitsky, V. Astashev, and A. Kalashnikov, "Autoresonant control of nonlinear mode in ultrasonic transducer for machining applications," *Ultrasonics*, vol. 42, no. 1-9, pp. 29–35, 2004.

[170] V. Babitsky, A. Kalashnikov, and F. Molodtsov, "Autoresonant control of ultrasonically assisted cutting," *Mechatronics*, vol. 14, no. 1, pp. 91–114, 2004.

[171] S. Voronina and V. Babitsky, "Autoresonant control strategies of loaded ultrasonic transducer for machining applications," *Journal of Sound and Vibration*, vol. 313, no. 3-5, pp. 395–417, 2008.

[172] Y. Kuang, M. Sadiq, S. Cochran, and Z. Huang, "Ultrasonic cutting with resonance tracking and vibration stabilization," in *IEEE Ultrasonics Symposium (IUS)*, pp. 843–846, IEEE, 2012.

[173] Y. Kuang, Y. Jin, and Z. H. S. Cochran, "Resonance tracking and vibration stablilization for high power ultrasonic transducers," *Ultrasonics*, vol. 54, no. 1, pp. 187–194, 2014.

[174] J. Gallego-Juarez, "Piezoelectric ceramics and ultrasonic transducers," *Journal of Physics E: Scientific Instruments*, vol. 22, no. 10, 1989.

[175] E. Neppiras, "The pre-stressed piezoelectric sandwich transducer," *Ultrasonics international 1973*, pp. 295–302, 1973.

[176] D. DeAngelis, G. Schulze, and K. Wong, "Optimizing piezoelectric stack preload bolts in ultrasonic transducers," *Physics Procedia*, vol. 63, pp. 11–20, 2015.

[177] "Matweb material properties." asm.matweb.com. Accessed: 2018-08-28.

[178] S. Volkov, I. Garanin, and Y. Kholopov, "Choice of waveguide material for ultrasonic welding," *Russian Ultrasonics*, vol. 28, no. 3, pp. 102–108, 1998.

[179] A. Abdullah, M. Shahini, and A. Pak, "An approach to design a high power piezoelectric ultrasonic transducer," *Journal of Electroceramics*, vol. 22, no. 4, pp. 369–382, 2009.

[180] H. Hibbitt, B. Karlsson, and P. Sorensen, "Abaqus user subroutines reference manual version 6.10," *Dassault Systèmes Simulia Corp.: USA*, 2011.

[181] H. Al-Budairi, *Design and analysis of ultrasonic horns operating in longitudinal and torsional vibration*. PhD thesis, University of Glasgow, 2012.

[182] Y. Kuang, *Resonance Tracking and Vibration Stabilisation of Ultrasonic Surgical Instruments*. PhD thesis, University of Dundee, 2014.

[183] T. Emam and A. Cuschieri, "How safe is high-power ultrasonic dissection?," *Annals of Surgery*, vol. 237, no. 2, pp. 186–191, 2003.

[184] A. Mathieson, *Nonlinear characterisation of power ultrasonic devices used in bone surgery*. PhD thesis, University of Glasgow, 2012.

[185] A. Mathieson, A. Cardoni, N. Cerisola, and M. Lucas, "Understanding nonlinear vibration behaviours in high-power ultrasonic surgical devices," *Proceedings of the Royal Society A: Mathematical, Physical and Engineering Sciences*, vol. 471, no. 2176, 2015.

[186] F. Bejarano, A. Feeney, R. Wallace, H. Simpson, and M. Lucas, "An ultrasonic orthopaedic surgical device based on a cymbal transducer," *Ultrasonics*, vol. 72, pp. 24–33, 2016.

[187] A. Feeney, L. Kang, and S. Dixon, "Nonlinearity in the dynamic response of flexural ultrasonic transducers," *IEEE Sensors*, vol. 2, no. 1, pp. 1–4, 2017.

[188] "Structure of the cranial skull." www.aofoundation.org. Accessed: 2018-08-14.

[189] "The Phacon navigator." www.phacon.de. Accessed: 2018-06-29.